University of Alberta

Positron Emission Tomography Target Volume Delineation

by

Laura Anne Drever

A thesis submitted to the Faculty of Graduate Studies and Research in partial fulfillment of the requirements for the degree of Master of Science

in

Medical Physics

Department of Physics

Edmonton, Alberta

Fall 2005

0-494-09153-3

Library and Archives Canada

Published Heritage Branch

395 Wellington Street
Ottawa ON K1A 0N4
Canada

Bibliothèque et Archives Canada

Direction du Patrimoine de l'édition

395, rue Wellington
Ottawa ON K1A 0N4
Canada

Your file *Votre référence*
ISBN:
Our file *Notre reference*
ISBN:

NOTICE:
The author has granted a non-exclusive license allowing Library and Archives Canada to reproduce, publish, archive, preserve, conserve, communicate to the public by telecommunication or on the Internet, loan, distribute and sell theses worldwide, for commercial or non-commercial purposes, in microform, paper, electronic and/or any other formats.

The author retains copyright ownership and moral rights in this thesis. Neither the thesis nor substantial extracts from it may be printed or otherwise reproduced without the author's permission.

AVIS:
L'auteur a accordé une licence non exclusive permettant à la Bibliothèque et Archives Canada de reproduire, publier, archiver, sauvegarder, conserver, transmettre au public par télécommunication ou par l'Internet, prêter, distribuer et vendre des thèses partout dans le monde, à des fins commerciales ou autres, sur support microforme, papier, électronique et/ou autres formats.

L'auteur conserve la propriété du droit d'auteur et des droits moraux qui protège cette thèse. Ni la thèse ni des extraits substantiels de celle-ci ne doivent être imprimés ou autrement reproduits sans son autorisation.

In compliance with the Canadian Privacy Act some supporting forms may have been removed from this thesis.

While these forms may be included in the document page count, their removal does not represent any loss of content from the thesis.

Conformément à la loi canadienne sur la protection de la vie privée, quelques formulaires secondaires ont été enlevés de cette thèse.

Bien que ces formulaires aient inclus dans la pagination, il n'y aura aucun contenu manquant.

Canada

To my family and friends

Abstract

Current radiation therapy techniques rely on the precise delivery of high doses of radiation to well defined volumes. However, the imaging modality that is most commonly used to determine the treatment volumes, computed tomography (CT), cannot easily distinguish between cancerous tissue and normal tissue. Since positron emission tomography (PET) can more readily differentiate between cancerous and normal tissues there is great interest in using PET images to delineate target volumes for radiation therapy treatment planning. The drawback of using PET is that the accurate geometric delineation of tumor volumes is a subject open to considerable interpretation which renders manual delineation highly problematic. Therefore, an automatic tool to delineate target volumes is being sought. Three methods of automatic target volume delineation were examined: thresholding, edge detection and the marker based watershed technique. The development of a completely automatic method of target volume delineation, iterative thresholding, will also be discussed.

Table of Contents

1. **Introduction** 1

2. **Physics of PET Imaging** 7

2.1 Positrons 7

2.1.1 Positron Emission 7

2.1.2 Mean energy of emitted betas and positrons 10

2.1.3 Positron Transport and Annihilation 11

2.2 Detection 19

2.2.1.1 Scintillation 19

2.2.1.2 Characteristics of Scintillators 20

2.2.2 Photomultiplier Tubes 24

2.2.3 Amplification 25

2.2.4 Discrimination 26

2.2.5 Coincidence Detection 26

2.3 Conclusion 27

3. **Introduction to Segmentation** 30

3.1 Introduction 30

3.2 Thresholding 31

3.3 Sobel Edge Detection 32

3.4 Watershed 33

3.5 Conclusion 35

4. **Measurement Methodology** 36

4.1 Thresholding 42

4.2 Sobel 43

4.3 Watershed 44

5. **Experimental Results and Discussion** 46

5.1 Introduction 46

5.2 Thresholding 46

5.2.1 Cylinders 46

5.2.2 Spheres 66

5.3 Sobel 81

5.3.1 Cylinders 81

5.3.2 Spheres 83

5.4 Watershed 85

5.4.1 Cylinders 85

5.4.2 Spheres 86
5.5 Conclusion 87
6. Iterative Thresholding 90
6.1 Introduction 90
6.2 Spherical Targets 94
6.3 Irregular Targets 116
6.4 Application to Patient Data 122
6.5 Conclusion 124
7. Conclusion and Future Directions 127
References ..... **Error! Bookmark not defined.**

List of Tables

Table 2.1: Summary of the relative probability of each interaction for each element present in the ICRU soft tissue model. 15

Table 2.2: Summary of the properties of three common scintillators, NaI(Tl), BGO and LSO. 21

Table 5.1: Ideal threshold values for large, medium and small cylinder at three radial offsets and multiple target to background activity concentration ratios. 52

Table 5.2: Summary of the percentage differences between the physical volume and the single threshold volume for the three spheres, and the absolute volume difference for the different target to background activity concentration ratios. 77

Table 6.1: Summary of the percentage difference (measured – true) between the physical volume and the calculated volume for the application of a single threshold, the iterative threshold for only the axial data set, and the tri-axial iterative threshold to the spherical data, also shown is the absolute difference in volume. 114

Table 6.2: Summary of clinical volumes determined from both PET and CT patient images. 124

List of Figures

Figure 1.1: Diagram of line source phantom. A 1mm diameter tube was filled with activity and placed inside the 20cm diameter plastic phantom, which was then imaged. 4

Figure 1.2: Image of the line source phantom with a low window and level setting. It can be seen that the entire plastic region of the phantom is shown as a region of higher activity concentration. 4

Figure 1.3: Image of the line source phantom with a medium window and level setting. The solid white line indicates the outer edge of the plastic phantom, while the region of higher activity is shown within. 5

Figure 1.4: Image of the line source phantom with a high window and level setting. Only the tube of activity is shown as being a region of higher activity density. 5

Figure 1.5: A profile through the bright spot shown in Figure 1.4. 6

Figure 2.1: Position of ^{18}F relative to its decay product ^{18}O on the chart of nuclides, and its decay scheme. 8

Figure 2.2: Position of ^{22}Na relative to its decay product ^{22}Ne on the chart of nuclides, and its decay scheme. 9

Figure 2.3: Spectral distribution of positrons emitted by ^{18}F 10

Figure 2.4: Monte Carlo simulation of positron transport in tissues of clinical relevance. 12

Figure 2.5: Angular deviation from colinearity of annihilation photons in water. 14

Figure 2.6: Finite positron flight transforms positron point source into a distributed volume of annihilation radiation emission. 16

Figure 2.7: Emission photons deviate by an angle θ from colinearity causing an error in the point of origin as identified by back projection. 16

Figure 2.8: Compton scattering through an angle θ of one emission photon leads to an error in the point of origin as identified by back projection. 17

Figure 2.9: Differential Compton cross section per unit solid angle as a function of photon scattering angle for 511keV annihilation photons. 18

Figure 2.10: Energy bands in a crystal. At left are the processes characteristic of a pure NaI scintillator, at right are the processes in the presence of an activator, such as Tl in NaI(Tl) 20

Figure 2.11: Apparent width of a detector element d' increases as the radial offset from the centre of the PET scanner. Because the depth at which the scintillation event occurred is unknown the annihilation event could occur at any position between the two dashed lines. 23

Figure 2.12: Schematic of photomultiplier operation. Electrons released from the photocathode are attracted to the first dynode and multiplied. Each successive dynode is at a higher potential than the previous. The final signal is collected at the anode and output to the remaining electronics. 24

Figure 2.13: Side view of a stack of detector rings. The leftmost image shows the 2D mode in which only coincident events from the same ring are recorded. The right image shows the 3D mode in which coincident events from any pair of detectors are recorded. 27

Figure 4.1: Diagram of phantom with the medium cylindrical target centered in the phantom. 37

Figure 4.2: Photograph of the phantom. Note the pump assembly on the top of the phantom lid. 37

Figure 4.3: Photograph of PET scanner used. 39

Figure 4.4: Photograph of the pump assembly contained in a watertight structure on the lid of the phantom. 40

Figure 4.5: The white rectangle, representing a large slice width, demonstrates the difficulty in choosing the physical area, of a spherical target represented by the dark circle, on each image slice. 41

Figure 4.6: Histogram of number of occurrences versus pixel values for a PET image of the large cylindrical target centered in the phantom. 43

Figure 5.1: Calculated diameter versus threshold for the (a) small, (b) medium, and (c) large cylinder for different target to background activity concentration ratios. 48

Figure 5.2: Ideal threshold versus physical area for the large cylinder at three radial offsets, 0mm, 32mm and 64mm, for a target to background activity concentration ratio of approximately 15:1. 49

Figure 5.3: Ideal threshold versus physical area for the large cylinder at three radial offsets, 0mm, 32mm and 64mm, for a target to background activity concentration ratio of approximately 3:1. 49

Figure 5.4: Ideal threshold versus physical area for the medium cylinder at three radial offsets, 0mm, 32mm and 64mm, for a target to background activity concentration ratio of approximately 5:1. 50

Figure 5.5: Ideal threshold versus physical area for the small cylinder at three radial offsets, 0mm, 32mm and 64mm, for a target to background activity concentration ratio of approximately 15:1. 50

Figure 5.6: Ideal threshold versus physical area for the small cylinder at three radial offsets, 0mm, 32mm and 64mm, for a target to background activity concentration ratio of approximately 5:1. 51

Figure 5.7: Mean background pixel intensity along the length of the medium cylinder centered in the phantom for different target to background activity concentration ratios. 53

Figure 5.8: Contrast range along the length of the medium cylinder centered in the phantom at different target to background activity concentration ratios. 53

Figure 5.9: Threshold values that produce the correct physical area versus slice number for the (a) small, (b) medium, (c) large cylinders centered in the phantom for different target to background activity concentration ratios. 55

Figure 5.10: Diameter versus threshold for a medium target cylinder with a medium confounding cylinder for different target to background activity concentration ratios (a)-(d). Target centered in the phantom, confounding volume 64mm offset from centre. 58

Figure 5.11: Diameter versus threshold for a large target cylinder with a large confounding cylinder for different target to background activity concentration ratios (a)-(d). Target offset 64mm from centre of phantom, confounding volume 128mm from centre of target 60

Figure 5.12: Diameter versus threshold for a medium target cylinder with a large confounding cylinder for different target to background activity concentration ratios (a)-(d). Target offset 64mm from centre of phantom, confounding volume centered in phantom. 62

Figure 5.13: Diameter versus threshold for a large target cylinder with a medium confounding cylinder for different target to background activity concentration ratios (a)-(d). Target centered in phantom, confounding volume offset 64mm from centre of phantom. 64

Figure 5.14: Diameter versus threshold for a small target cylinder with a large confounding cylinder for different target to background activity concentration ratios (a)-(d). Target centered in phantom, confounding volume offset 64mm from centre of phantom. 66

Figure 5.15: Area calculated using a threshold value that produces the correct volume versus the radial displacement from the centre of the large sphere for different target to background activity concentrations. 67

Figure 5.16: Area calculated using a threshold value that produces the correct volume versus the radial displacement from the centre of the medium sphere for different target to background activity concentrations. 67

Figure 5.17: Area calculated using a threshold value that produces the correct volume versus the radial displacement from the centre of the small sphere for different target to background activity concentrations. 68

Figure 5.18: Ideal threshold based on the central slice contrast range, versus the physical area for the (a) small, (b) medium, and (c) large sphere. 70

Figure 5.19: Ideal threshold based on the contrast range from each slice, versus the physical area for the (a) small, (b) medium, and (c) large sphere. 71

Figure 5.20: Percentage error, (physical area-measured area/physical area)*100%, between the true physical area and the calculated area by applying a single mean threshold to the large sphere. 72

Figure 5.21: Percentage difference, (physical area-measured area/physical area)*100%, between measured and true cross sectional areas versus the physical cross section for the (a) small, (b) medium, and (c) large sphere. 75

Figure 5.22: Calculated area, using a 28% threshold, versus slice number for the (a) small, (b) medium, and (c) large spheres. 76

Figure 5.23: Ideal threshold versus the physical area for a small spherical target with a large confounding volume offset from the target by 64mm, for a target to background activity concentration ratio of 2:1. 78

Figure 5.24: Ideal threshold versus physical area for the large sphere at three radial offsets, 0mm, 32mm and 64mm, for a target to background activity concentration ratio of approximately 15:1. 79

Figure 5.25: Ideal threshold versus physical area for the large sphere at three radial offsets, 0mm, 32mm and 64mm, for a target to background activity concentration ratio of approximately 5:1. 79

Figure 5.26: Ideal threshold versus physical area for the medium sphere at three radial offsets, 0mm, 32mm and 64mm, for a target to background activity concentration ratio of approximately 10:1. 80

Figure 5.27: Ideal threshold versus physical area for the medium sphere at three radial offsets, 0mm, 32mm and 64mm, for a target to background activity concentration ratio of approximately 3:1. 80

Figure 5.28: Ideal threshold versus physical area for the small sphere at three radial offsets, 0mm, 32mm and 64mm, for a target to background activity concentration ratio of approximately 10:1. 81

Figure 5.29: Sobel and Watershed experimental diameters versus target to background activity concentration ratio for the (a) large, (b) medium, and (c) small cylinders. 83

Figure 5.30: Sobel areas versus radial displacement from the centre of the sphere for multiple target to background activity concentration ratios for the (a) large, (b) medium, and (c) small sphere. 85

Figure 5.31: Watershed areas versus radial displacement from the centre of the sphere for multiple target to background activity concentration ratios for the (a) large, (b) medium, and (c) small sphere. 87

Figure 6.1: Ideal threshold versus physical area for the spherical targets at all target to background activity concentration ratios. 93

Figure 6.2: Fits to ideal threshold versus area for the spherical targets at all target to background activity concentration ratios. 94

Figure 6.3: Area found using the iterative thresholding technique only on the axial data set for the small sphere at approximately (a) 15, (b) 10, (c) 5, (d) 3, and (e) 2 to one target to background activity concentration ratios versus slice number. 96

Figure 6.4: Area found using the iterative thresholding technique only on the axial data set for the medium sphere at approximately (a) 15, (b) 10, (c) 5, (d) 3, and (e) 2 to one target to background activity concentration ratios versus slice number. 98

Figure 6.5: Area found using the iterative thresholding technique only on the axial data set for the large sphere at approximately (a) 15, (b) 10, (c) 5, (d) 3, and (e) 2 to one target to background activity concentration ratios versus slice number. 100

Figure 6.6: Calculated area using the tri-axial iterative thresholding method with a threshold of one for the small sphere for target to background activity concentration ratios of approximately (a) 15, (b) 10, (c) 5, (d) 3, and (e) 2 to one versus slice number. 103

Figure 6.7: Calculated area using the tri-axial iterative thresholding method with a threshold of one for the medium sphere for target to background activity concentration ratios of approximately (a) 15, (b) 10, (c) 5, (d) 3, and (e) 2 to one versus slice number. 105

Figure 6.8: Calculated area using the tri-axial iterative thresholding method with a threshold of one for the large sphere for target to background activity concentration ratios of approximately (a) 15, (b) 10, (c) 5, (d) 3, and (e) 2 to one versus slice number. 107

Figure 6.9: Calculated area using the tri-axial iterative thresholding method with a threshold of two for the small sphere for target to background activity concentration ratios of approximately (a) 15, (b) 10, (c) 5, (d) 3, and (e) 2 to one versus slice number. 109

Figure 6.10: Calculated area using the tri-axial iterative thresholding method with a threshold of two for the medium sphere for target to background activity concentration ratios of approximately (a) 15, (b) 10, (c) 5, (d) 3, and (e) 2 to one versus slice number. 111

Figure 6.11: Calculated area using the tri-axial iterative thresholding method with a threshold of two for the large sphere for target to background activity concentration ratios of approximately (a) 15, (b) 10, (c) 5, (d) 3, and (e) 2 to one versus slice number. 113

Figure 6.12: Calculated area using the tri-axial iterative thresholding method versus slice number for the medium sphere at a target to background activity concentration ratio of fifteen to one. This data set was not used to generate the fit used in the iterative thresholding. 115

Figure 6.13: Photograph of the deformed spheroid volume. 116

Figure 6.14: Photograph of the small bottle used as an irregular shaped target volume. 117

Figure 6.15: Comparison of CT generated, axial and tri-axial iterative threshold areas versus slice number for the deformed spheroid target for target to background activity concentration ratios of approximately (a) 15, (b) 10, (c) 5, (d) 3 and (2) to one. 120

Figure 6.16: Comparison of CT generated, axial and tri-axial iterative threshold areas versus slice number for the small bottle target for target to background activity concentration ratios of approximately (a) 15, (b) 10, (c) 5, (d) 3 and (2) to one. 122

Figure 6.17: Patient image, note the dark spots in the patient's left lung. The first spot is near the left shoulder, the second near the midline and the third near the heart of the patient. 123

List of Abbreviations

3D-CRT	Three Dimensional Conformal Radiotherapy
IMRT	Intensity Modulated Radiotherapy
CT	Computed Tomography
PET	Positron Emission Tomography
FDG	Fluorodeoxyglucose
MRI	Magnetic Resonance Imaging
GTV	Gross Tumor Volume
ICRU	International Commission on Radiation Units and Measurements
NaI(Tl)	Thallium-doped Sodium Iodide
BGO	Bismuth Germanate
LSO	Cerium-doped Lutetium Oxyorthosilicate
PMT	Photomultiplier Tube
PHA	Pulse Height Analyzer
GVF	Gradient Vector Flow
PMMA	Polymethyl Methacralate
NEC	Noise Equivalent Count Rate

1. Introduction

New techniques in radiation therapy such as three-dimensional conformal radiotherapy (3D-CRT) and intensity modulated radiotherapy (IMRT) are designed to deliver large doses of radiation to small volumes. The intent of these techniques is to deliver higher doses to diseased tissue while sparing surrounding normal tissues and are expected to yield better control of cancers with fewer accompanying normal tissue complications. However, with higher doses being delivered to smaller regions it is imperative that tumor volumes be accurately and completely delineated. Uncertainty in the location and the extent of the tumor will jeopardize patient outcome.

Computed tomography (CT) is the current imaging standard for radiotherapy treatment planning as this modality provides accurate, high resolution, anatomical patient images. Further, this modality provides the electron densities of imaged tissues which are required by modern treatment planning systems to correct dose calculations in order to account for heterogeneities in patients. Unfortunately, the change in electron density between normal tissue and cancerous tissue can be quite small making an accurate differentiation between normal and cancerous tissues difficult.

Recently there has been interest in augmenting the anatomical data contained in CT images with the physiological or functional data available from positron emission tomography (PET) images. Oncologic PET images are created by introducing a radioactive tracer, which decays through positron emission, into the patient. The most commonly used tracer is fluorodeoxyglucose (FDG) which has been labeled with an F-18 atom. Since FDG is a glucose analog, a measure of the uptake of FDG can be compared to the uptake of glucose which correlates with the metabolic activity of tissue. Since cancerous tissue is more metabolically active than normal tissue it takes up more FDG than do normal cells. Once FDG has been taken up by a cell it is phosphorylized, after which it cannot escape from the cell. This ensures that the FDG that is injected into the patient seeks out metabolically active tissue and then remains in that tissue. As the FDG sits in the tissue the F-18 atom will eventually decay releasing a positron, which, in turn will

undergo mass annihilation producing two photons that may be detected to form the PET image. Therefore, tumors will appear as bright spots in a lighter background[1,2].

The uses of PET in oncology are many, ranging from use in diagnosis and treatment planning to the follow up care of the patient. PET imaging is useful in the confirmation of suspected malignancies as FDG is quickly taken up by tissues with higher metabolic activity[3,4,5]. Malignant lung tumors, for example, have demonstrated a significantly higher uptake of FDG in comparison to their benign counterparts[5]. The differentiation between benign and malignant is difficult to make from anatomical information alone. PET imaging also has the ability to improve cancer staging as compared to CT or MRI. The staging of non-small cell lung cancer is based on the size of the tumor visible in a CT or MRI scan; however this technique can confuse normal tissue as tumor[5]. PET has higher sensitivity and specificity in the staging of non-small cell lung cancer than do either CT or MRI [1,7,8,9]. PET imaging is also being explored for its potential to aid in identifying the primary site of disease when cancer is strongly suspected but the location is unknown[6]. Additionally, PET imaging can be used to measure the response of cancer to a treatment[3]. When a cancerous mass responds to treatment the amount of activity taken up by the tumor decreases, however, the physical size may not readily exhibit detectable change. This allows the oncologist to more accurately gauge patient response and change the course of treatment as required. Finally PET imaging can be used to aid in the diagnosis of recurrent disease[3]. FDG PET imaging is thus a very useful tool in the diagnosis and treatment of cancer. PET imaging can help to confirm suspected malignancies, improve cancer staging, help find the site of the disease, measure the response to therapy and aid in the diagnosis of recurrent disease[1,7,8].

The first step in augmenting CT data with PET data is to correctly align, or register, the two image sets. The second is to accurately delineate the cancerous tissue, or target volume, on the PET image. The step of registering the two images has been well studied[10,11,12,13] while little work has been done on the accurate delineation of PET targets[14].

Some of the difficulties which hamper accurate target volume delineation on PET images are the time frame over which the image is acquired, and the low resolution of the PET scanner. As PET images are acquired over tens of minutes there is ample opportunity for patient motion, both voluntary and involuntary, which will result in a blurring of the image. Further, the resolution of the PET scanner is relatively low, on the order of 4mm at the centre of the scanner and increasing at the outer edge of the bore, which will further blur the image. The result of this blurring is an amorphous ill-defined tumor volume of elevated activity concentration surrounded by a heterogeneous background of lower activity concentration. With PET images it is possible to adjust the window and level of the image in such a way as to make the bright spots either disappear completely or fill nearly the entire image. This effect can be seen in **Figures 1.2** through **1.4**, which are produced from the same data set with different window and level settings. **Figure 1.1** depicts the physical arrangement upon which these images are based. Here a 1 mm diameter inner tube of activity is situated at the center of a surrounding 20 cm diameter plastic cylindrical phantom. The solid plastic phantom is devoid of activity except for that contained within the inserted tube. The bright region indicated by the window and level settings of **Figure 1.2** corresponds to the entire phantom. A second set of window and level settings (see **Figure 1.3**) yields a bright region which is smaller than the full extent of the phantom (indicated by the solid white circle) but considerably larger than the inner tube of activity. A third set of window and level settings, used in **Figure 1.4**, yields a cross section corresponding to the inner tube of activity only. **Figure 1.5** shows the pixel intensity versus the pixel number along a line through the bright spot in **Figure 1.4**. The central peak corresponds to the tube of activity while the outer region of the peak corresponds to the size of the phantom. Outside the phantom the pixel intensity drops sharply to zero. These difficulties cause PET images to be difficult to interpret. In a recent study three radiation oncologists were first shown standard CT data sets and were asked to outline the gross tumor volume (GTV). Later the same radiation oncologists were given a merged set of PET/CT images for the same group of patients, and were asked to once again outline the GTV. With the PET information the size of the planning target volume (PTV) was increased in 24 to 70% of the cases and decreased in 30-76% of the cases. This study illustrates the difficulty in both outlining tumor volumes on CT alone, and the added difficulty in accurately relating to the information provided by PET imaging[14].

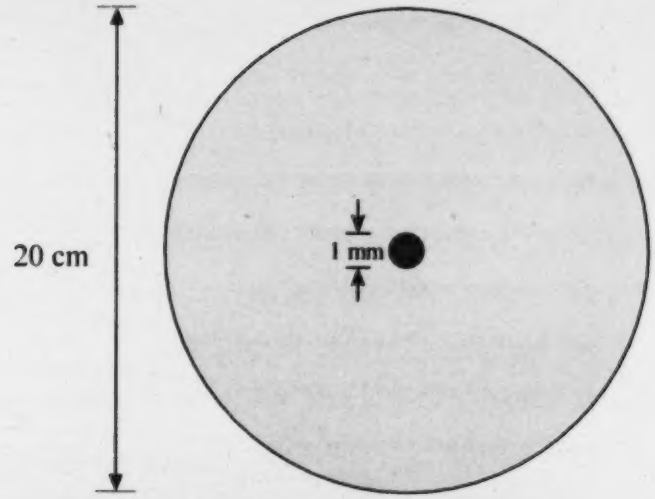

Figure 1.1: Diagram of line source phantom. A 1mm diameter tube was filled with activity and placed inside the 20cm diameter plastic phantom, which was then imaged.

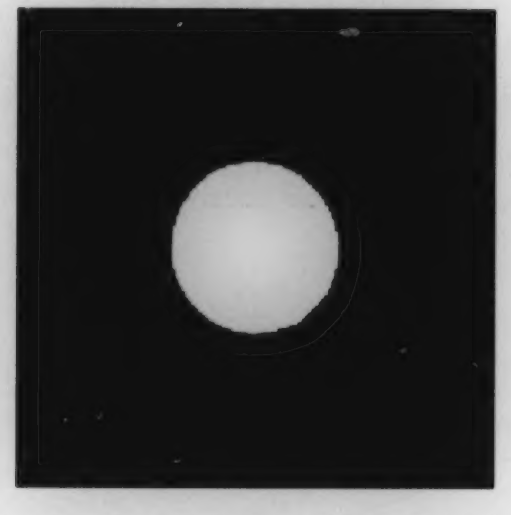

Figure 1.2: Image of the line source phantom with a low window and level setting. It can be seen that the entire plastic region of the phantom is shown as a region of higher activity concentration.

Figure 1.3: Image of the line source phantom with a medium window and level setting. The solid white line indicates the outer edge of the plastic phantom, while the region of higher activity is shown within.

Figure 1.4: Image of the line source phantom with a high window and level setting. Only the tube of activity is shown as being a region of higher activity density.

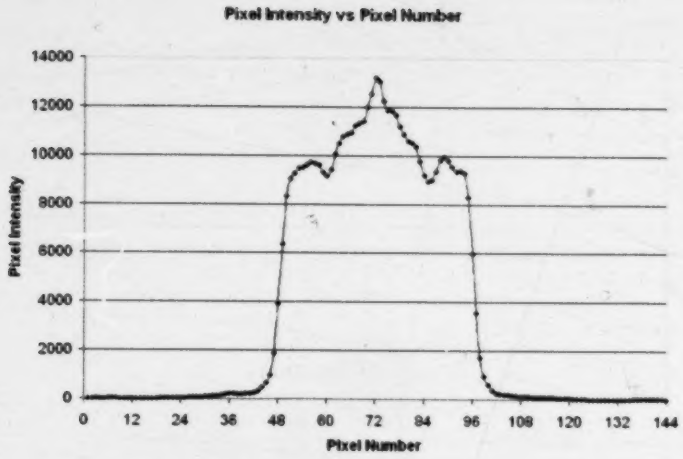

Figure 1.5: A profile through the bright spot shown in **Figure 1.4**.

The amorphous appearance of targets in PET images, along with the large change possible in apparent target size as a function of display settings renders the manual delineation of targets unreliable. In order to use PET images quantitatively in radiation therapy treatment planning a more reliable and robust method of delineation is highly desirable. Such a method must be accurate and reliable over a large range of target sizes, target shapes, activity concentrations and locations within the bore of the scanner. To this end three segmentation techniques are investigated with regard to their ability to properly delineate well defined target volumes with known activity distributions. These methods are thresholding, Sobel edge detection and a marker-based watershed technique. The threshold technique was chosen for its overall conceptual and practical implementation simplicity. Watershed segmentation is, by comparison, considerably more complex but potentially more robust in its application. Sobel edge detection provides a middle ground between these two extremes.

2. Physics of PET Imaging

Oncologic positron emission tomography images are formed by injecting patients with fluorodeoxyglucose labeled with F-18. Since FDG is a glucose analog it is preferentially taken up by cancerous cells in the patient. Once a FDG molecule has entered a cell it undergoes phosphorylation and cannot exit the cell. After FDG becomes trapped the F-18 atoms will decay and emit positrons, which in turn will undergo annihilation, each producing two high energy annihilation photons. The annihilation photons will then interact with the scintillation crystals used by the PET scanner to convert the high energy annihilation photons into lower energy light that can be detected by photomultiplier tubes. The photomultiplier tubes amplify and measure the signal coming from the patient. The signals from all the photomultiplier tubes are analyzed by the coincidence timing circuit to remove noise. After the coincidence timing circuitry has removed many of the non-coincident events the data is fed to a computer system to be reconstructed and displayed.

2.1 Positrons

2.1.1 Positron Emission

Decay by positron emission consists of the emission of a positron and an electron neutrino and a decrease in the atomic number, Z, of the nucleus by one. Two examples of positron emission are

$$^{18}_{9}\mathrm{F} \Rightarrow {}^{18}_{8}\mathrm{O} + e^{+} + \nu_e + Q + \text{orbital electron}$$

$$^{22}_{11}\mathrm{Na} \Rightarrow {}^{22}_{10}\mathrm{Ne} + e^{+} + \nu_e + Q + \text{orbital electron}$$

The decay schemes for these two interactions are shown in **Figures 2.1** and **2.2** respectively. An additional orbital electron mass is required on the right side of the above equations due to the decrease in the atomic number of the nucleus. In order for an atom to undergo positron emission it must exceed the mass (atomic mass) of the product atom by at least $2m_e$. When energetically possible, the positron is emitted with a maximum energy, $E_{e^+}^{max}$, that is equal to the Q value of the interaction minus 1.022 MeV which is required to produce the two electrons. A spectrum of positron energies is observed due to the accompanying

emission of an electron neutrino. Positron emission spectra are skewed to the right due to the repulsion between the emitted positron and the product nucleus (see **Figure 2.3**, adapted from Levin et al[15]).

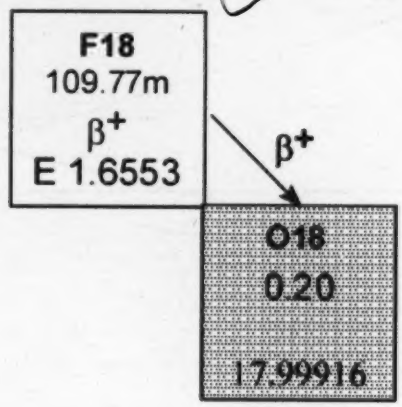

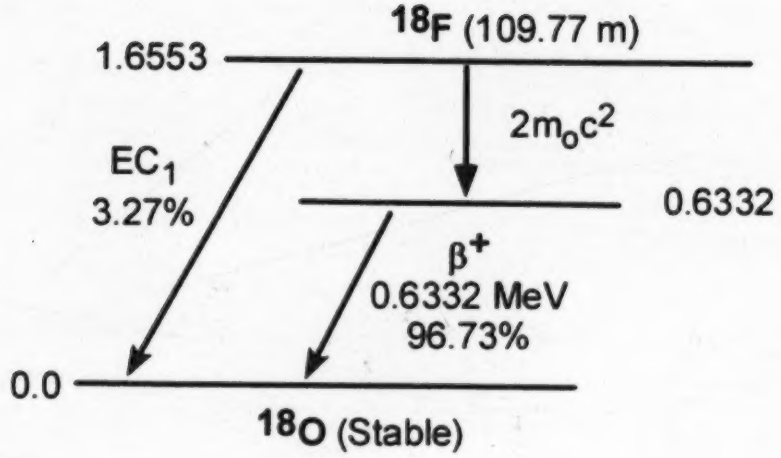

Figure 2.1: Position of ^{18}F relative to its decay product ^{18}O on the chart of nuclides, and its decay scheme.

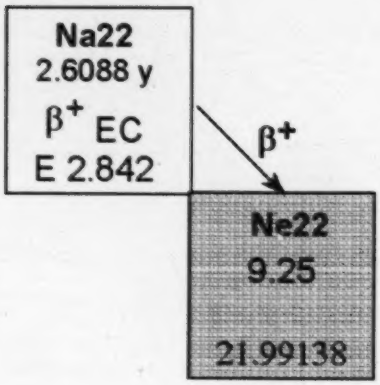

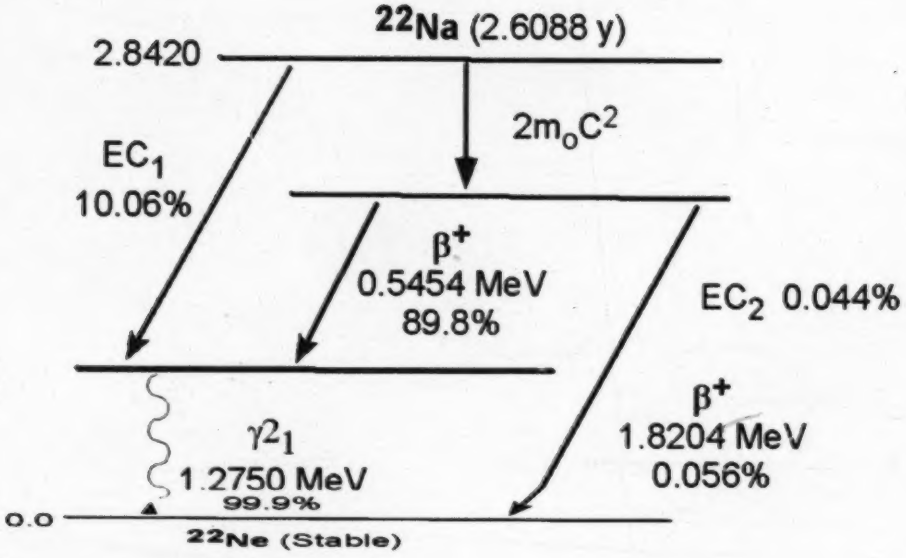

Position of ^{22}Na relative to its decay product ^{22}Ne on the chart of nuclides, and its decay scheme

Figure 2.2: Position of ^{22}Na relative to its decay product ^{22}Ne on the chart of nuclides, and its decay scheme.

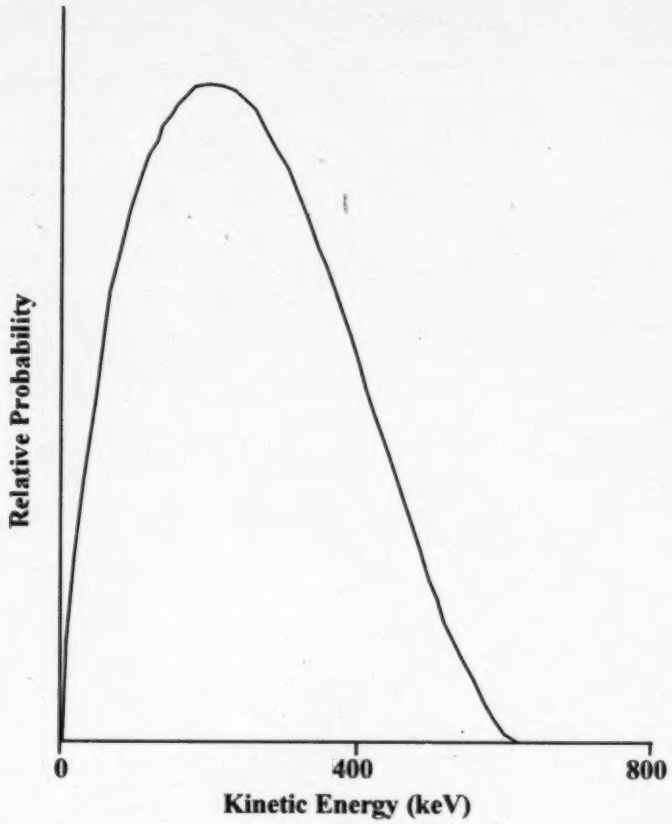

Figure 2.3: Spectral distribution of positrons emitted by ^{18}F.

2.1.2 Mean energy of emitted betas and positrons

The average kinetic energy, measured in MeV, of positrons emitted in radioactive interactions is given by

$$E_{e^+}^{ave} = \frac{E_{e^+}^{max}}{3}\left(1 + \frac{\sqrt{E_{e^-}^{max}}}{4}\right) \qquad (2.1)$$

As with beta decay, a reasonable approximation of the mean positron energy is

$$E_{e^+}^{ave} = \frac{E_{e^+}^{max}}{3} \qquad (2.2)$$

Since positrons are anti-particles, they will eventually be captured by electrons of the medium and will undergo annihilation with those electrons. This process is more probable for low energy positrons than for high energy positrons

2.1.3 Positron Transport and Annihilation

Positrons lose energy along their path by means of collisional and radiative interactions with the medium through which they are traveling in much the same manner as electrons. The major difference between the two is that positrons may loose up to and including their entire energy in any collisional loss whereas electron energy losses are limited to one half their total kinetic energy. At the end of its track through matter a positron will eventually undergo mass annihilation with an electron from the medium as either a quasi-free particle or as part of a bound system (e^+e^-) called positronium. This bound state may be resolved into two substates: a singlet state called para-positronium where electron and positron spins are aligned in an antiparallel orientation, and a parallel alignment triplet state referred to as ortho-positronium. Experimentally, the vast majority of positrons achieve thermalization with the medium in a very short time frame, on the order of 10^{-12} s post emission[16]. An experimental examination of the spectral annihilation line in copper produced by the β+ decay of ^{64}Cu (E_{max} = 0.66 MeV) set 2% as an upper limit to the number of positrons which undergo in flight annihilation prior to being slowed to thermal velocities[17]. These results have been reinforced by other experimenters who conclude that the probability of a positron undergoing annihilation prior to achieving thermal energies is negligible[18,19]. The time required for thermalization, ~10^{-12} s, is short in comparison to the average lifetime of a positron in condensed matter, which ranges anywhere from 100 to 500 ps depending on the medium[16] . The energy of a thermalized positron is of the order of 0.01 eV and is considerably smaller than that of most electrons of the medium[16]. In the process of being slowed down by the media, positrons will travel a short but finite distance from their point of emission prior to annihilation. Positron flight, which is the linear distance from point of origin to annihilation position, is considerably shorter than the continuous slowing down range due to the highly torturous path which results due to multiple scattering. Monte Carlo simulations of positron transport in tissues of clinical relevance yield radial distances from emission to annihilation which exhibit the sharp cusp-like distributions shown in **Figure 2.4** (adapted from Sanchez-Crespo et al[20]). For ^{18}F, the

radionuclide used in this thesis work, the Full Width at Half Maximum (FWHM) and Full Width at one Tenth Maximum (FWTM) of the distribution of positron flight in soft tissue are 0.19 mm and 0.91 mm respectively[20]. While the sub-millimeter range in tissue of positrons emitted by medically utilized radionuclides renders the annihilation process a relatively localized phenomenon over distances of clinical relevance, their finite flight distance poses one of several limiting factors to the overall image resolution which may be theoretically achieved with PET imaging.

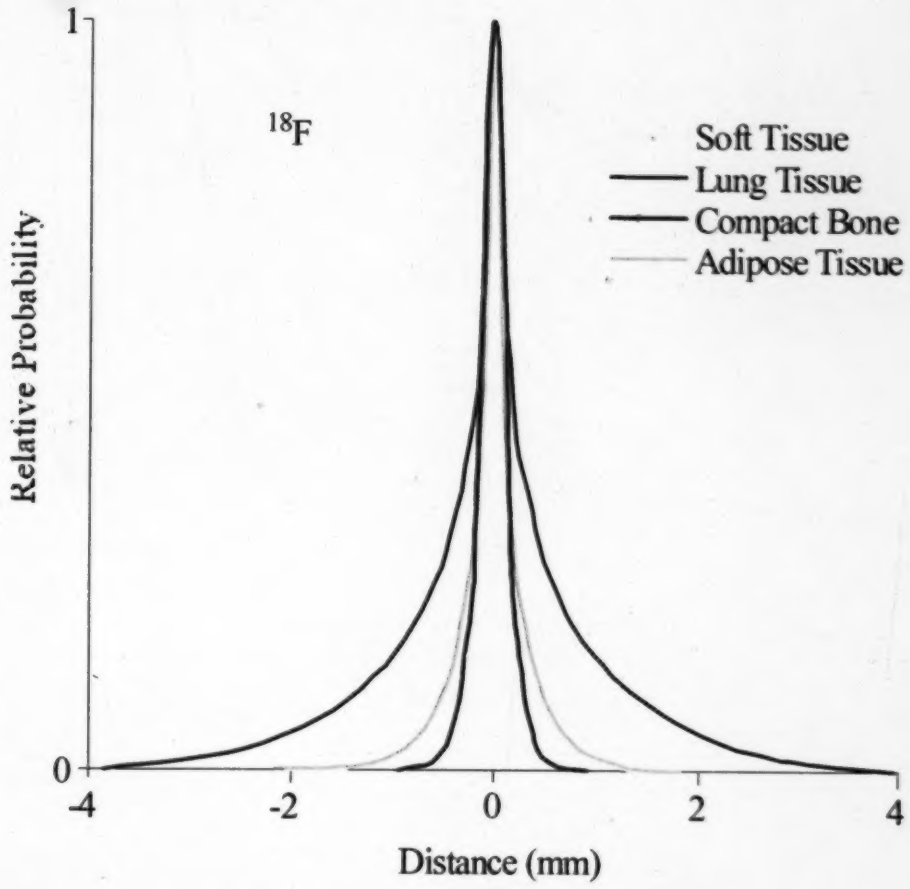

Figure 2.4: Monte Carlo simulation of positron transport in tissues of clinical relevance.

The annihilation of a quasi-free positron can produce several different results. Single photon annihilation is possible but only in the presence of a third body required to absorb the recoil momentum. Experimentally

this form of annihilation is observed at negligible rates and for all practical purposes may be safely ignored. Processes resulting in three or more annihilation photons also occur. The most probable of these is the three photon annihilation mode which occurs at rates of about only 0.27% that of the two gamma mode. As with the case of single photon annihilation, modes producing three or more photons are sufficiently rare so as to render them of little consequence in standard PET imaging. The dominant form of annihilation results in the creation of two photons. In the rest frame these two annihilation photons are emitted in opposite directions to one another, each with momentum = $m_o c$. Non-zero momentum in the laboratory frame results in photon emission which deviates by a small amount (~ 0 to 20 mrad) from colinearity.

The non-zero momentum of the annihilating electron-positron pair also results in a Doppler shift of the emission spectrum from the nominal value of $m_o c^2$. The kinetic energy of the annihilating pair is typically on the order of a few electron volts and is almost entirely due to the residual momentum of electrons in matter. The finite range in the kinetic energies of the electron-positron pairs also results in a Doppler broadening of the observed annihilation emission spectral line. Because of the low thermal positron energies the degree of broadening is almost entirely due to the momentum distribution of electrons in matter.

Those positrons which achieve thermal energies and do not undergo annihilation as a quasi-free particle eventually form a bound state with an electron called positronium. The binding energy of positronium is 6.8 eV in vacuum. The momentum of positronium in the laboratory frame is lower than that associated with quasi-free positron annihilation. Deviation from colinearity of the emission gamma rays produced by the decay of positronium is thus less than that associated with the annihilation photons produced by quasi-free positrons. The relative yield of quasi-free positrons and positronium is highly dependent upon the nature of the medium. The stopping of positrons in amorphous media such as water produces both quasi-free positrons and positronium which together yield the annihilation angular deviation from colinearity spectrum shown in **Figure 2.5** (adapted from Mogensen et al [21]).

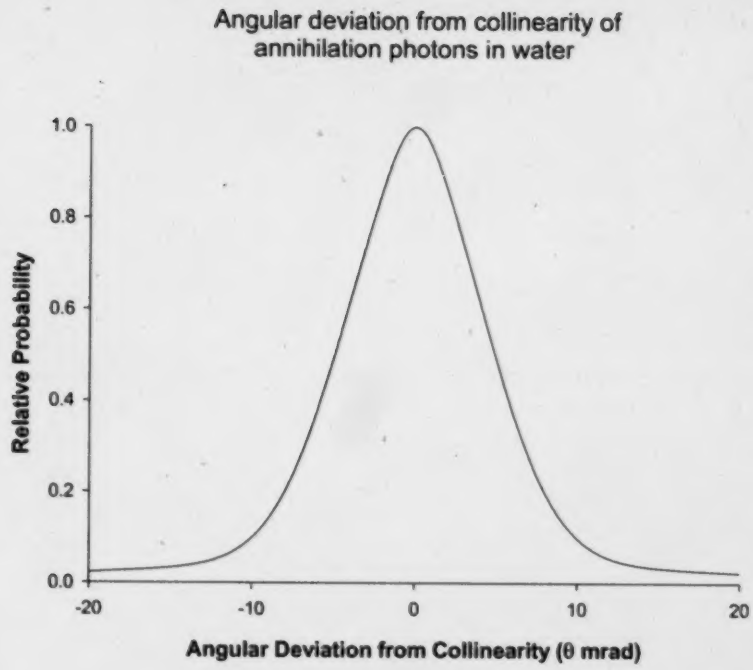

Figure 2.5: Angular deviation from colinearity of annihilation photons in water.

The existence of positron flight and the departure of annihilation photons from strict colinearity pose fundamental limitations to the resolution, which may be theoretically achieved with PET imaging. The contributions of photon scattering processes serve to exacerbate the blurring of annihilation radiation emission leading to further degradation of PET image resolution. Positron flight transforms a positron point source into a distributed region of annihilation photon emission constituting a small but finite volume, see **Figure 2.6**, ranging from 1 to 2 mm in size depending on tissue type. The non-colinearity of annihilation photons creates an apparent volumetric distribution of emission as illustrated in **Figure 2.7**. Here two sets of emission photons are depicted. The first set is created exactly at 180° to one another and an ideal detector system would indicate a back projected location of origin coincident with their true point of emission. A second set of annihilation photons is emitted with a small angular deviation (5 mrad) from true colinearity. Over a typical flight path of from 40 to 50 cm from point of creation to detector surface a perfect coincidence back projection would indicate a point of origin displaced by a little more than 2mm

from its true emission location. Both of these effects combine to set a fundamental limit to the physical resolution which may be achieved with PET imaging. To this must be added the effects of scatter as encountered by the annihilation photons subsequent to emission but prior to detection. The mean free path of a 511 keV photon in tissue[22] is approximately 10.5 cm and hence a significant number of emission photons will undergo interactions in transiting even modest amounts of body mass. At photon energies of 511 keV the possible interaction processes are coherent or Rayleigh scattering, photoelectric absorption, and Compton scattering. Of these three modes of interaction, the Compton process is by far the most prominent. The relative probability of each interaction is listed in **Table 2.1** for each element constituting the ICRU four component soft tissue model[22].

Element	Composition (by mass)	Relative Probability of Occurrence		
		Coherent Scattering	Photoelectric Absorption	Compton Scattering
Hydrogen	0.101174	0.00%	0.00%	100.00%
Carbon	0.111000	0.18%	0.06%	99.76%
Nitrogen	0.026000	0.23%	0.02%	99.75%
Oxygen	0.761826	0.29%	0.03%	99.68%

Table 2.1: Summary of the relative probability of each interaction for each element present in the ICRU soft tissue model.

Photoelectric interactions result in complete absorption of an incident photon and hence serve only to reduce the overall number of annihilation photons reaching the detection system. Coherent scattering causes small angle deflections of incident photons without an accompanying energy change. The retention of incident energy renders photons scattered by this process indistinguishable from unscattered radiation and a broadening of the effective annihilation emission volume results. Fortunately the relative contribution from this process is very small (<0.3%) and may be safely ignored.

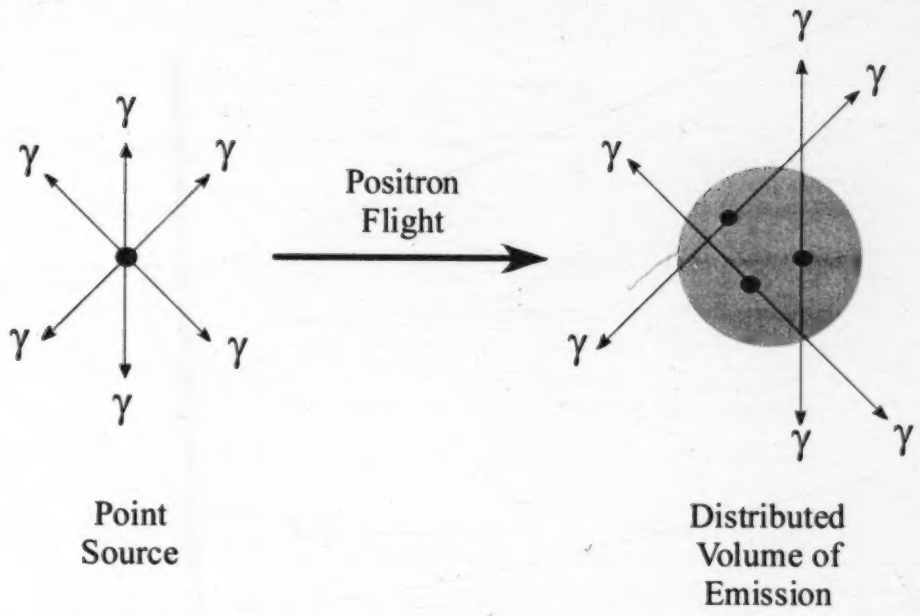

Figure 2.6: Finite positron flight transforms positron point source into a distributed volume of annihilation radiation emission.

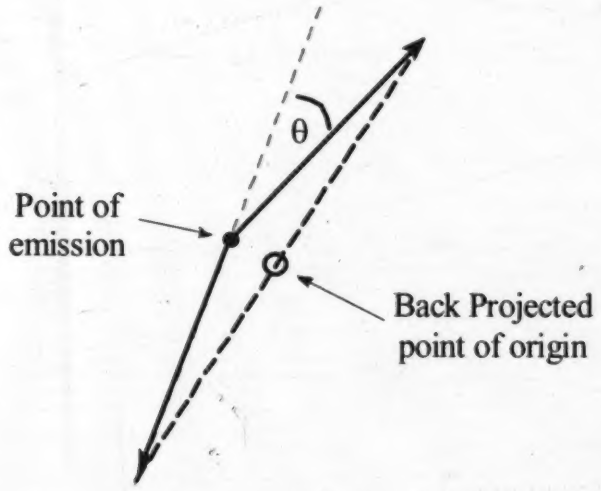

Figure 2.7: Emission photons deviate by an angle θ from colinearity causing an error in the point of origin as identified by back projection.

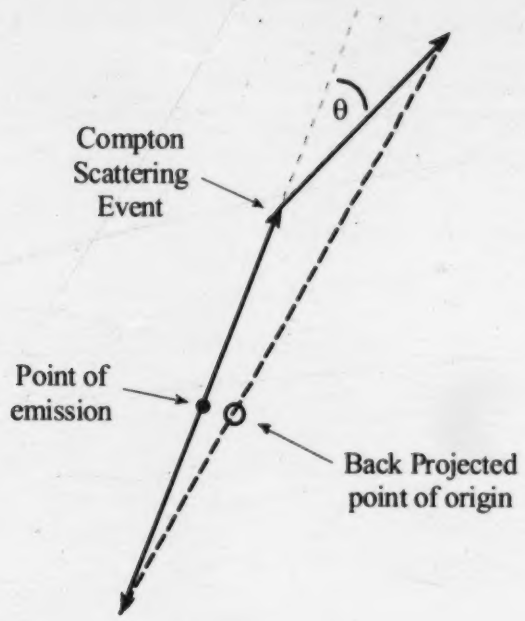

Figure 2.8: Compton scattering through an angle θ of one emission photon leads to an error in the point of origin as identified by back projection.

Compton scattering is by far the most probable interaction process by which annihilation photons may be deflected from their original direction of motion. In this process the incident photon imparts a fraction of its initial energy to an electron of the medium and a scattered photon of reduced energy results. The differential Compton interaction cross section as a function of scattering angle is given by

$$\frac{d\sigma}{d\omega} = \frac{r_o^2}{2}\left(1-\cos^2\theta\right)\left[\left(\frac{1}{1+\alpha\left(1-\cos\theta\right)}\right)^2\left(1+\frac{\alpha^2\left(1-\cos\theta\right)^2}{\left[1+\alpha\left(1-\cos\theta\right)\right]\left(1+\cos^2\theta\right)}\right)\right] \qquad (2.3)$$

where $\alpha = \frac{h\nu_o}{m_o c^2}$ and $h\nu_o$ = energy of the incident photon . **Equation 2.3** is plotted for 511 keV photons in **Figure 2.9**. While small angle scattering clearly dominates, the distribution is sufficiently broad to render Compton scattering a significant contributor to the degradation of PET image resolution (see **Figure 2.8**). In principle, Compton scattered annihilation photons can be distinguished from their unaltered counterparts by means of energy discrimination but doing so in practice is limited by the energy

resolution of the detector system, typical energy windows over which coincident photons are analyzed in PET are fairly broad, 350 – 670 keV. This finite energy interval admits large Compton scattering angles (> 50°) and contributes a significant broadening of the effective annihilation emission volume. Photon scattering serves to render every atom of the surrounding medium a potential annihilation scattering center. The combined effects of positron flight, non-colinear emission and Compton scattering serve to set fundamental physical limits on the image resolution which may be achieved with PET imaging. Practical aspects of coincidence detection contribute additional degradation to the fidelity of PET images.

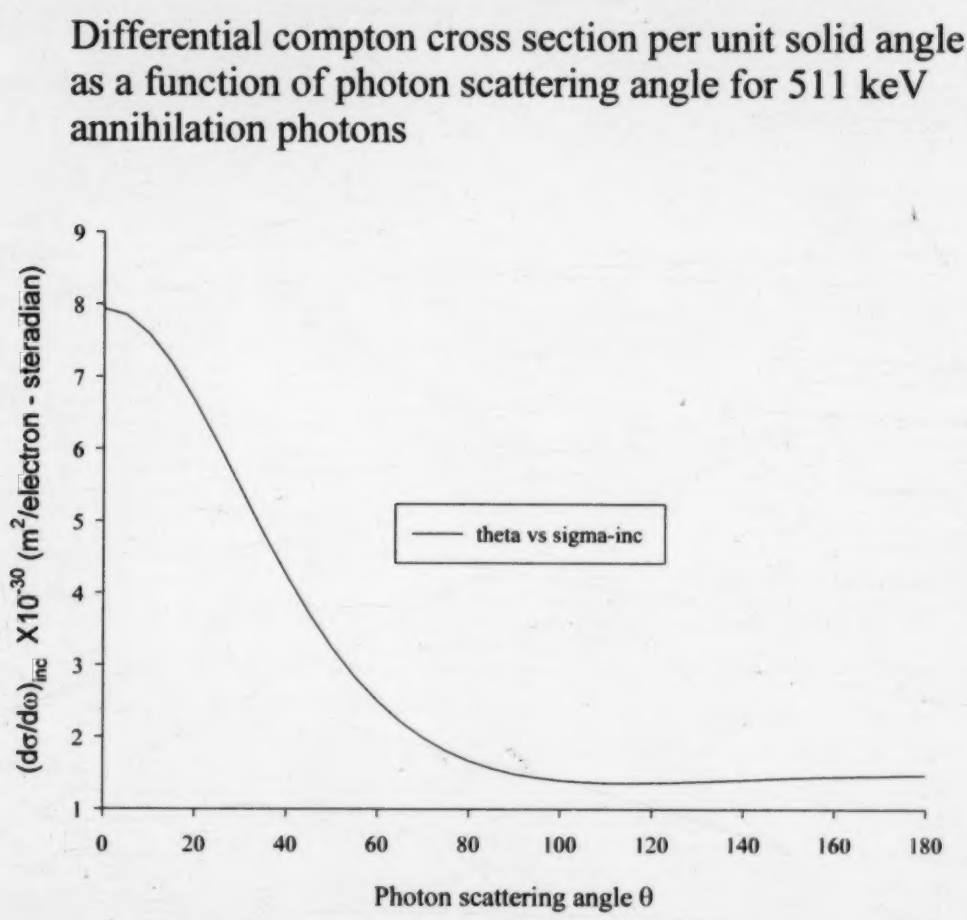

Figure 2.9: Differential Compton cross section per unit solid angle as a function of photon scattering angle for 511keV annihilation photons.

2.2 Detection

Positron emission tomography uses scintillation detectors with coincidence timing circuits to record annihilation photon interactions. A scintillation detector functions by converting high-energy photons into lower energy photons. These lower energy photons are directed to interact with photomultiplier tubes which convert visible light into an electrical signal. Amplifiers amplify and reform the electrical signal created and energy discrimination circuitry rejects prompts that fall outside of a predetermined energy window. Finally coincidence timing circuits are used to discard signals that do not arrive within a fixed time interval.

2.2.1.1 Scintillation

PET cameras use inorganic crystal scintillators to convert high-energy annihilation photons into lower energy visible photons. As shown in **Figure 2.10**, two energy bands exist in the inorganic crystal structure of the scintillator; the lower energy band is known as the valence band while the higher energy band is known as the conduction band[2.24]. In a non-excited scintillator the valence band is full, but incoming radiation with sufficient energy may raise an electron from the valence band to the conduction band. The raised electron will quickly fall back from the conduction band to the valence band by emitting a photon with energy equivalent to the spacing between the two bands. This spacing, or energy gap, is usually about 4eV in width. To reduce self-absorption of the light, and to increase the probability of photon emission, small amounts of impurities are often added to the crystals. These impurities are known as activators. In scintillators doped with impurities the emission of light occurs between the activator sites which are energetically situated within the gap between valence and conduction bands. Since the light is emitted between different energy states in the doped crystal than exist within the pure crystal the wavelength of the resulting light is different and self absorption of the optical photons produced is considerably reduced.

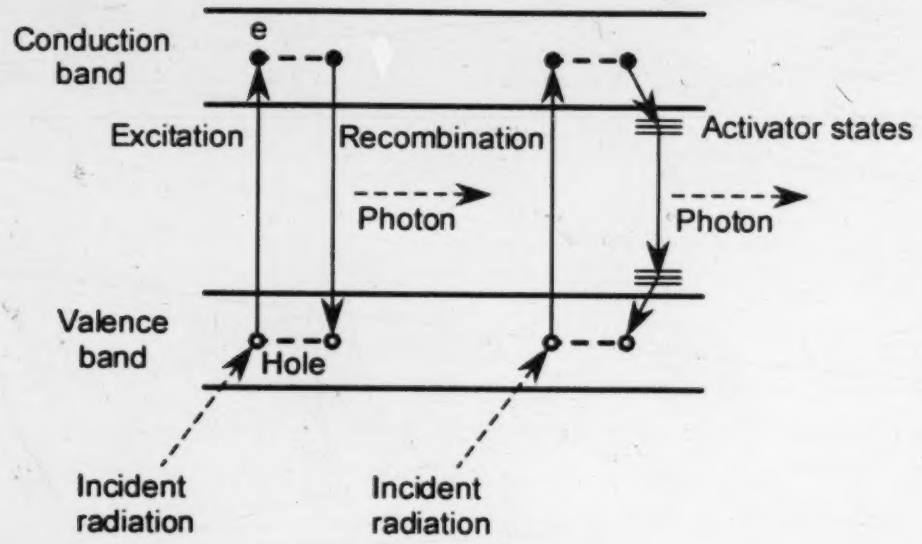

Figure 2.10: Energy bands in a crystal. At left are the processes characteristic of a pure NaI scintillator, at right are the processes in the presence of an activator, such as Tl in NaI(Tl).

2.2.1.2 Characteristics of Scintillators

For an inorganic crystalline scintillator to be of use in a PET system it must meet several criteria. First, the atomic number and the density of the scintillator must be as high as possible. Second, the decay time between absorption and subsequent emission must be short and the light output of the crystal should be high with an emission wavelength near 400nm for optimal photocathode absorption. Further, it is important that the crystal be transparent at the emission wavelength with an index of refraction near 1.5, which is similar to the glass window at the end of the PMT. It is also beneficial that the crystal is radiation hard, nonhygroscopic, rugged, and can be produced at a minimal cost[23,24].

The crystal should have a high effective atomic number and a high density to improve the interaction probability of photons with the crystal. The higher the density and atomic number the more likely a photon is to interact through either of the photoelectric or Compton processes. Since the annihilation photons are of relatively high energy, scintillators of higher density and atomic numbers are desired.

Once a photon has excited an electron to the conduction band it is important that this electron fall back to the valence band as quickly as possible. The shorter the decay time the better the coincidence timing of

PET scanner. If the decay time is too long the PET scanner will need a wide coincidence-timing window. A broad time window will reduce the efficiency of the scanner. It is also important that the crystal emit as much light as possible per interaction with the incident radiation. The emitted light should have a wavelength as close as possible to 400nm to ensure that the photomultiplier tubes are efficiently converting the light produced into electrons at the photocathode. Another important consideration is that the crystal should be as transparent as possible to the emitted light. If the scintillator absorbs the emitted light before it can interact with the photomultiplier tube, the information carried by that light is lost. It is also important that the index of refraction of the crystal should be close to that of the entrance window of the photomultiplier tube for optimal photon coupling between the two devices. This will ensure that more of the light will interact with the photomultiplier tube.

Finally an ideal scintillator should be radiation hard in order to minimize radiation induced changes in the properties of the crystal. Also, it is beneficial that the crystal be nonhygroscopic as this will eliminate the need to ensure a hermetic seal. When the crystals are rugged they are easier to manufacture and less likely to break while in use. Since each PET scanner uses multiple scintillating detectors it is also important that the manufacturing process of the crystal be economical. These properties describe an ideal scintillator. Unfortunately no known scintillator possess all of these desired characteristics. Therefore, it is necessary to compromise on some characteristics in order to obtain the best overall detectors for PET imaging. Three scintillators that are commonly used in PET systems: thallium-doped sodium iodide, NaI(Tl), bismuth germanate, BGO, and cerium-doped lutetium oxyorthosilicate or LSO. As the experimental work of this thesis was performed using a PET scanner with NaI(Tl) detectors the following discussion will focus on NaI(Tl). A summary of the properties of three common scintillators, NaI(Tl), BGO and LSO is presented in **Table 2.2**.

Crystal	Density (g/cm^3)	Effective Atomic Number	Primary Decay Constant (ns)	Secondary Decay Constant (ns)	Relative Emission Intensity	Emission Wavelength (nm)	Index of Refraction
NaI(Tl)	3.67	51	230	~10000	100	410	1.85
BGO	7.13	75	300		15	480	2.15
LSO	7.40	65	40		75	420	1.82

Table 2.2: Summary of the properties of three common scintillators, NaI(Tl), BGO and LSO.

While NaI(Tl) is rather ill suited to use in PET scanners it has nevertheless seen extensive utilization in the past since its relative emission intensity is very high, the emission wavelength of the crystal is very close to 400nm, the index of refraction is close to 1.5 and the production of NaI(Tl) is very economical.

The major drawbacks of using NaI(Tl) as a scintillator in PET scanners are the long secondary decay constant, the low density and the low effective atomic number. The long secondary decay constant of the crystal requires that the coincidence timing window must be much longer than for two other common PET detector crystals shown in **Table 2.2**. The low density and low effective atomic number of the crystal translate into a low detection efficiency for NaI(Tl) at PET photons energies. Further, the low density of the crystal necessitates the use of a very thick crystal. The long secondary decay constant and the necessity of using a very thick crystal further degrade the quality of the resulting image. A thick crystal affects the resolution of the image through the depth of interaction effect. Minor difficulties are also associated with using NaI(Tl) as a scintillator in a medical system include that the crystals are neither nonhygroscopic nor rugged. These crystals need to be protected from the moisture in the air as well as mechanical and thermal shocks. This requires that the crystals be hermetically sealed and well insulated.

Since the annihilation photons have energy of 511keV the scintillation crystal must be quite thick to effectively stop these photons. The thicker the scintillation crystal the larger the apparent width of the detector becomes, as the apparent width of the detector increases the resolution of the PET scanner decreases. The effect of the depth of interaction on the resolution of the detector is related to the width and thickness of the detector element as well as the angular offset of the detector element in the ring. The effective detector size may be determined according to **Equation (2.4)**, where d is the width of the detector, x is the thickness of the detector and θ is the angular offset, as shown in **Figure 2.11**.

$$d' = d\cos\theta + x\sin\theta \qquad \textbf{(2.4)}$$

The depth of interaction effect can cause significant degradation of the detector resolution. As θ decreases the effective width of the detector element decreases and the resolution is not as degraded. Since the degradation of the resolution is decreased with a decrease in angle θ a technique to improve image resolution would be to create a scanner with a larger radius. For example if a detector element was one

centimeter away from the vertical detector and the radius was 30cm the angle would be approximately two degrees. However if the radius of the bore was 60cm the angle from the vertical would be approximately 1 degree. Therefore, PET scanners are designed with larger bore radii than are necessary to accommodate the patient.

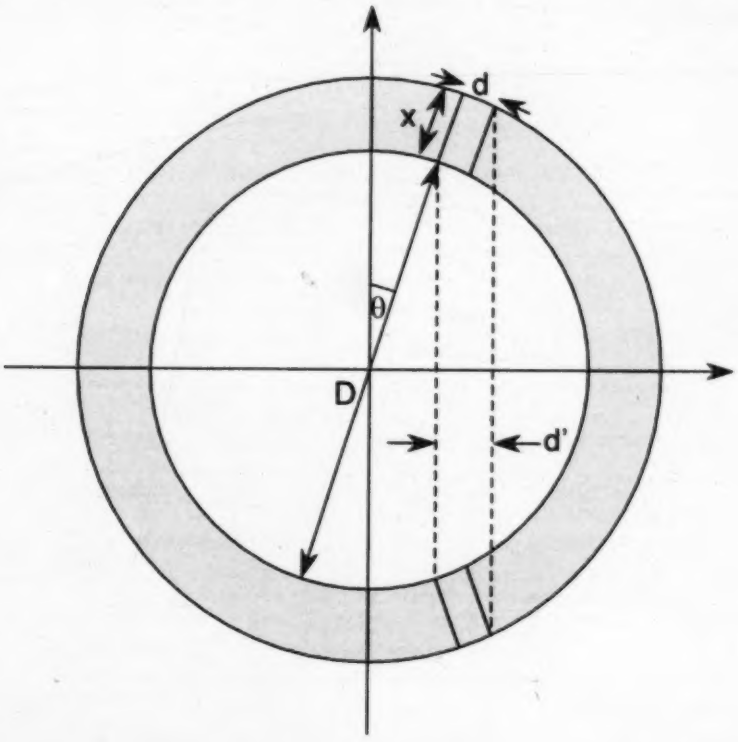

Figure 2.11: Apparent width of a detector element d' increases as the radial offset from the centre of the PET scanner. Because the depth at which the scintillation event occurred is unknown the annihilation event could occur at any position between the two dashed lines.

2.2.2 Photomultiplier Tubes

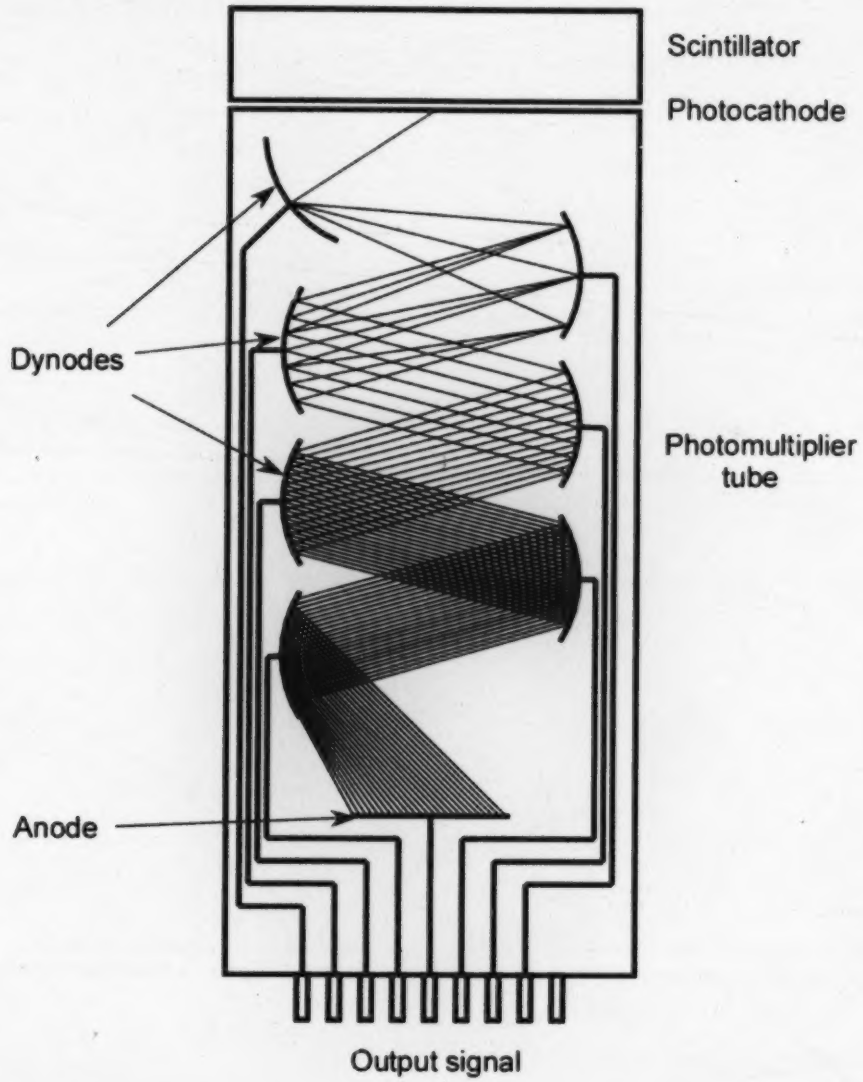

Figure 2.12: Schematic of photomultiplier operation. Electrons released from the photocathode are attracted to the first dynode and multiplied. Each successive dynode is at a higher potential than the previous. The final signal is collected at the anode and output to the remaining electronics.

After the excited scintillation crystal releases a low energy photon, this photon may interact with one of the photomultiplier tubes, shown schematically in **Figure 2.12**, through the photoelectric effect to create an electrical signal which is then recorded by the PET scanner.

Scintillation photons collide with the metal of the photocathode at the base of the PMT and photoelectrons are liberated. A photoelectron so produced is steered and accelerated by means of an applied electric field towards the first dynode. As the photoelectron collides with the dynode more electrons are released which subsequently travel together towards the next dynode. At each dynode the number of departing electrons is five times greater than the number of incident electrons. As there are between ten and fourteen dynodes per PMT the electronic signal is magnified many times before the electrons reach the anode where the signal is measured.

2.2.3 Amplification

The electrical signal that is produced by photomultiplier tubes is, relatively speaking, quite small, on the order of 0.1 to 1 volt. Further, the signal is not a sharply peaked pulse but rather consists of a sharp rise followed by an exponential decay. The exponential decay of the signal is shown in **Equation (2.5)**, where V_o is the initial voltage, t is the elapsed time, τ is the time constant of the circuit and V is the voltage.

$$V = V_o e^{-t/\tau} \qquad \textbf{(2.5)}$$

The purpose of the amplifier is to both increase the amplitude of the signal and suitably reshape the form of the pulse. The amplitude of the signal needs to be increased in order to facilitate further analysis of the signal as required to drive pulse height analyzers. Since the tail of the pulse form is excessively long it needs to be significantly shortened in order that sequential pulses do not add together to form one elongated waveform that is not representative of individual signals.

2.2.4 Discrimination

Once the signal has been amplified and reshaped it must pass through a series of tests to determine if the event that has been measured should be recorded and processed. An important step in PET imaging is performed by a pulse-height analyzer which is used to determine if a signal falls within the desired energy window.

Pulse-height analyzers (PHA) count only those amplifier output pulses which fall within the desired amplitude range. The amplitude range is related to the acceptable energy window. For PET imaging the energy range is centered about 511keV. Energy discrimination is used to remove scattered radiation and random events that are of lower energy than true coincident events.

2.2.5 Coincidence Detection

After the pulse height analyzer identifies an initial signal the electronics will wait a predefined time, known as the coincidence-timing window, for a subsequent signal, of sufficient energy, to be created in a second PMT. When two candidate events are recorded within the coincidence timing window the coincident signals can be one of three types: true, scattered or random. True coincidences occur when the two recorded prompts originate from the same annihilation event. Scattered coincidences occur when one or both of the annihilation photons are scattered before interacting with the detectors. Random coincidences occur when two photons from different annihilation events are recorded as coincident.

Scattered and random events do not carry useful information suitable for image reconstruction. Both scattered and random events reduce the quality of the reconstructed PET image. Scattered events depend on the geometry of the PET scanner and the amount of activity that is within the patient, but outside the field of view of the scanner. Random events depend on both the geometry of the scanner, the activity that is within the patient, but outside the field of view of the scanner and the amount of activity that is in the scanner. Activity that is outside the field of view of the scanner can contribute annihilation photons to the detector system since the annihilation photons are produced isotropically.

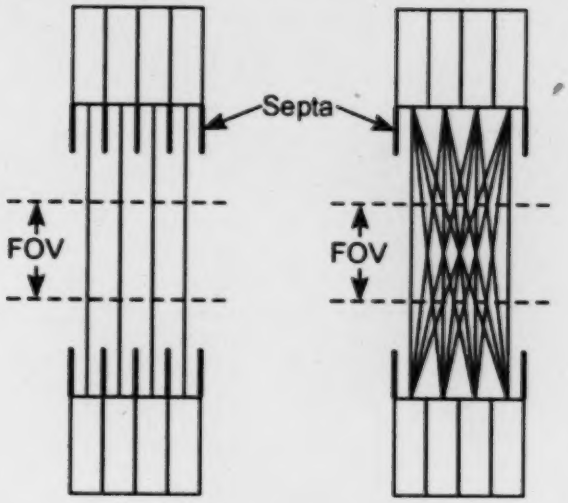

Figure 2.13: Side view of a stack of detector rings. The leftmost image shows the 2D mode in which only coincident events from the same ring are recorded. The right image shows the 3D mode in which coincident events from any pair of detectors are recorded.

To avoid detecting scattered and random events from outside the PET scanner, shielding can be used between rows of detector elements, see **Figure 2.13**. Using shielding between the rows of detector elements is known as 2D imaging and is less efficient than 3D imaging where no shielding is used. To further reduce the number of random events that are detected the amount of activity injected into the patient may be reduced. Since random events occur when there is a time overlap in the occurrence of two pulses, fewer pulses result in fewer random events. When the activity administered to the patient is doubled the number of random events increases as the square of the activity of the source while the number of true events increases only by a factor of two. Therefore the amount of activity used to form a PET image must be carefully considered to provide enough true events to form an image but also keep the number of random events low.

2.3 Conclusion

PET images are formed when the nucleus of an atom decays through β+ decay to produce a positron. This positron will carry away a fraction of the energy of the decay as kinetic energy. As the positron travels it

interacts with the surrounding media and the direction of travel of the positron can change many times before it slows to thermal energies. The range of travel of the positron before annihilation degrades the resolution of the final PET image, since the positron is, for image reconstruction purposes, assumed to annihilate at the site of its creation. The range of positron travel is not corrected for since it depends on the density of the surrounding material as well as the direction of travel of the charged particle.

Once the positron slows it will come in contact with a free electron and either undergoes annihilation as a quasi-free particle or form a short lived atom of positronium. Positronium atoms quickly decay predominantly through annihilation producing two photons each with approximately 511keV of energy. Assuming the positron was at rest at the moment of annihilation the angle between the annihilation photons must be 180 degrees to conserve the momentum of the system. However, the positron may not be at rest at the moment of annihilation and deviations from exact colinearity may occur. Any deviation from colinearity will further degrade the resolution of the final PET image since the line of response connecting the two photomultiplier tubes that recorded the annihilation event will not pass through the point where the annihilation occurred.

After annihilation occurs the photons produced may interact with scintillation crystals forming the detector system producing lower energy photons which will, in turn, interact with photocathodes at the base of photomultiplier tubes. The depth at which the interaction occurs within the scintillation crystal will affect the final resolution of the PET image. The depth of interaction depends on the density and the effective atomic number of the scintillation crystal. The higher the density and effective atomic number, the thinner the crystal may be, which, in turn, reduces the depth of interaction effect.

The photomultiplier tube will increase the signal and send it on to amplifier circuits where the pulse will be reshaped and amplified further. This step is necessary so that the signal may be properly analyzed by pulse-height analyzer and coincidence timing circuitry. Pulse-height analysis is used to discriminate the energy of the incident radiation and thus count only those events which fall within a specified energy window. Finally, coincidence timing allows pairs of events which occur within a certain time interval to be

recorded. The circuitry involved in these last three steps serves to reduce noise and provide a cleaner final image. The finite time required for each of these steps reduces the total number of events which may be recorded without the detector system being overwhelmed.

Finally the electric signals produced are sent to the reconstruction computer and the image is reconstructed and displayed on a computer monitor.

3. Introduction to Segmentation

3.1 Introduction

Segmentation of non-trivial images poses one of the most challenging problems in current image processing. Numerous methods abound and their characteristics can vary significantly according to their specific application and imaging modality. Currently, no single segmentation scheme exists which will yield acceptable results over the entire spectrum of medical image types which may be contemplated. Classic image segmentation may be defined as the partitioning of an image **I** into distinct constituent sub-regions or subsets $\mathbf{S}_i$ which are themselves homogeneous with respect to some defining characteristic. Thus these subsets must satisfy the following relations

$$\mathbf{S}_i \subset \mathbf{I} \qquad \mathbf{I} = \bigcup_{i=1}^{N} \mathbf{S}_i \qquad \mathbf{S}_i \cap \mathbf{S}_j = \emptyset \quad \forall i \neq j \qquad (3.1)$$

and every $\mathbf{S}_i$ is connected. When the constraint of connectedness is relaxed, as is often the case in medical image segmentation, the subsets $\mathbf{S}_i$ are referred to as classes. A further relaxation may be allowed by removing the constraint of non-intersection between subsets in order to encompass partial volume effects in which a single image element (pixel) may belong to multiple tissues. In what follows the classic definition of segmentation will be retained.

For the purpose of this thesis three segmentation techniques were explored. The first of these is simple threshold segmentation in which an image is divided according to pixel intensity level into regions corresponding to object and background. While this method of delineation is simple and straight forward for implementation, threshold values which yield correct object demarcation prove to vary as a function of object size. In response to this inherent limitation of the threshold technique, two alternative segmentation approaches were investigated. These are the Sobel and watershed methods. The Sobel technique relies on edge detection to identify the transition from background to object. The watershed algorithm is a region based approach which relies upon concepts drawn from mathematical morphology. The basic theory which underlies each of these three distinct approaches to segmentation is presented in this chapter.

3.2 Thresholding

Thresholding is a very simple and intuitive method of segmentation in which all pixels which meet a given criteria are regarded as belonging to the target while all others are relegated to background status. Application to PET images is intuitive as higher pixel values correspond to regions of elevated activity. The chief drawback of this method is selection of the correct threshold level at which to perform segmentation. Consider a grey scale image set **I** defined as

$$I = \{x, y, f(x, y)\} \tag{3.2}$$

where x and y are the spatial coordinates of the points which constitute the image and f(x,y) is the grey scale intensity at (x,y). Now let there exist a partition value $\tau \in \boldsymbol{R}$ and a partition function $\pi = \pi(\tau)$ such that

$$\pi : I \rightarrow T \tag{3.3}$$

where

$$T \subset I \tag{3.4}$$

such that

$$T = \{x, y, f(x,y) \mid f(x,y) \geq \tau\} \tag{3.5}$$

From this new set **T** let a further set **B** be defined as

$$B = I - T \tag{3.6}$$

In this manner the original grey scale image set **I** has been partitioned into the two disjoint grey scale image sub-sets **T** and **B** according to the partition value τ such that

$$I = T \cup B \tag{3.7}$$

The sub-sets **T** and **B** are commonly referred to as the target and background images respectively. For segmentation purposes it is customary to transform **T** and **B** to produce the images $\mathbf{T}'$ and $\mathbf{B}'$ where

$$T' = \{x, y, 1 \ \forall (x,y) \in T\} \text{ and } B' = \{x, y, 0 \ \forall (x,y) \in B\} \tag{3.8}$$

And form a new image $\mathbf{I}'$ from their union

$$I' = T' \cup B' \tag{3.9}$$

′ is thus a binary image composed of the target and background as two distinct objects. For medical applications the challenge is to determine a partition value τ such that the target image corresponds to meaningful clinical entity.

3.3 Sobel Edge Detection

The Sobel edge detection method performs segmentation according to maximums in the absolute value of the gradient of the image[25]. Inherent to this approach is the assumption that maximums in image gradient correspond to boundary locations. This method has the advantage of being less sensitive to image noise than most other edge detection methods and can also yield estimates of edge direction and magnitude which can be useful for subsequent processing. The magnitude and direction of the image gradient are determined according to

$$|\nabla f(x,y)| = \sqrt{\left(\frac{\partial f(x,y)}{\partial x}\right)^2 + \left(\frac{\partial f(x,y)}{\partial y}\right)^2}$$

$$\theta(x,y) = \tan^{-1}\left(\frac{\partial f(x,y)}{\partial x} \Big/ \frac{\partial f(x,y)}{\partial y}\right) \qquad (3.10)$$

where $f(x,y)$ is, as before, the grey scale image intensity. Digital images, of course, present intensity as a discrete, rather than continuous, function of spatial location and thus cannot be differentiated analytically, hence numerical approximations to the gradient must be employed. These numerical approximations are often represented as 3x3 matrices that operate on the image and are referred to as masks. The structure of a typical mask is shown in **Equation (3.11)**, where each matrix value is a weight value to be applied in the calculations.

$$\begin{bmatrix} w_1 & w_2 & w_3 \\ w_4 & w_5 & w_6 \\ w_7 & w_8 & w_9 \end{bmatrix} \qquad (3.11)$$

The response of the mask is defined at the center of the matrix and is given by

$$R = w_1\mathbf{I}_1 + w_2\mathbf{I}_2 + \ldots + w_9\mathbf{I}_9 \qquad (3.12)$$

where $\mathbf{I}_i$ is the gray level of the pixel being operated on and w_i is a mask coefficient. After application of the mask the remaining steps in the numerical edge detection are identical to those of analytical edge detection.

3.4 Watershed

Watershed segmentation is a region based technique which is based upon concepts derived from mathematical morphology. This technique yields closed contours unlike the Sobel and threshold approaches. The watershed method treats the gradient of the image as topography in which greater pixel values correspond to higher points in the landscape[26,29]. Conceptually this method searches for points in the topography where a drop of water is equally likely to run off in more than one direction. Connecting these points creates the watershed lines that segment the image. Another way of visualizing this technique is to imagine that wells have been drilled at all the local minima and the water table begins to rise. Eventually water from one local minimum would join with water from a second local minimum; dams are built to prevent the water from joining. In the end all that is left of the landscape are the dams which are the watershed segmentation lines.

Mathematically the watersheds can be found using the concepts of set theory. Let $g(x, y)$ represent the gradient of the image, and $M_1, M_2, \ldots, M_R$ be the set of coordinates representing the local minima. Points which are members of a catchment basin $C(M_i)$ form a connected component. The flooded level, $T[n]$, for some gradient level n, is defined as

$$T[n] = \{(s,t) | g(s,t) < n\} \qquad (3.13)$$

Processing the original grey scale image in this manner yields a binary map consisting of points which are either above or below the flood level. Mathematically, one has

$$C_n(M_i) = C(M_i) \cap T[n] \qquad (3.14)$$

Further, let $C[n]$ represent the union of the flooded portions of the catchment basins at level n

$$C[n]=\bigcup_{i=1}^{R}C_n(M_i) \tag{3.15}$$

where R is total number of catchment basins. The union of all catchment basins is then

$$C[\max+1]=\bigcup_{i=1}^{R}C(M_i). \tag{3.16}$$

The final union of all the catchment basins occurs at max+1, one intensity level above the flood. This is done so that the dams can be built above the flood.

With the above definitions, along with the fact that each connected component of $C[n-1]$ is contained in a single connected component of $T[n]$ it is possible to find the watershed lines of an image.

Straight forward application of the watershed methodology, as detailed above, often results in over segmentation of images. Overly segmented images contain no useful information hence methods of avoiding over segmentation need to be explored. One method of achieving this is to limit the region on which the watershed algorithm can operate. A second approach entails operating on an alternative to the gradient of the image.

The use of markers serves as an efficient means of limiting the region of the image that the watershed can operate on. A marker is a connected component that exists in the image. The approach taken here relies on the identification of two sets of markers; the first is a set of internal markers that are associated with a region internal to the object of interest while the second set of markers is external to the object of interest. A marker-based watershed approach is a powerful method for segmenting images but the quality of the segmentation is dependent on the choice of markers.

A second cause of over segmentation of an image is noise, which is amplified in the gradient. To avoid the over segmentation due to noise the gradient vector flow may be utilized instead of the gradient[27]. The gradient vector flow, GVF, was calculated using the method developed by Xu and Prince[28], using a Matlab module provided by Xu[38].

3.5 Conclusion

The segmentation of an image to extract useful information is a very complex task. Three methods for segmenting an image were introduced: thresholding, Sobel edge detection and the watershed method. The thresholding method is mathematically and conceptually the most intuitive. In this method each pixel is in turn compared to a threshold value, if the pixel meets this criterion it is included in the region of interest, if it does not it is excluded. The Sobel edge detection method searches for maximums in the absolute value of the gradient of the image. The maximums are found by calculating the response of each pixel to the Sobel mask, then comparing them to some threshold. If the pixels meet the threshold they are included in the edge line. The watershed method uses techniques from set theory to find the watershed points in the gradient vector flow of the image. The watershed points form lines known as the watershed lines, which are the end result of the segmentation of the image. Since a marker-based technique is required to avoid oversegmentation of the image, two sets of markers must be chosen before the watersheds can be found. The marker sets were determined by finding the location of the maximum pixel value in the image. The pixel intensity of the GVF image at this location was evaluated and used to threshold the image. This gives an image with two sets of markers which were separated and used as markers for the watershed method. Each of the three methods has advantages and weaknesses in the segmentation of an image. The main strength of thresholding is that it is very simple in concept; the main weakness is that the proper threshold has to be chosen to segment the image correctly. The main advantage of the Sobel edge detection is that it finds the edges in the image directly, but the Sobel edge detection experiences difficulty when the differences between the region of interest and the background are not large. The advantage of the watershed method is that no threshold value needs to be chosen before hand and it is not overly sensitive to noise in the image. However, an appropriate set of markers needs to be chosen in order for this method to segment an image properly.

4. Measurement Methodology

A phantom study utilizing simple geometric objects is employed to investigate the relative efficacy of the threshold, Sobel and watershed segmentation approaches to accurately delineate F-18 activated volumes in PET. Doing so makes possible a rigorous comparison of experimentally derived cross sectional areas and volumes to their physical or true values. A phantom study also eliminates the uncertainties associated with an assessment based on clinical data which, of necessity, involves uncertainties in both the physical extent of the tumor and the activity distributions involved. Hollow refillable cylinders and spheres constructed of polymethyl methacralate (PMMA) serve as target volumes. These were placed within a larger PMMA cylinder which itself may be loaded with activity to provide a surrounding background. The target cylinders, oriented with their axis of rotation orthogonal to the image plane and coincident with that of the external cylindrical phantom, provide volumes with cross sectional areas which are, apart from end effects, invariant in the longitudinal dimension. These yield data in which partial volume effects are restricted to the two dimensions of the image plane. The spheres, in contrast, exhibit cross sectional variations in all three dimensions in closer accord with real clinical volumes. Cylinders were constructed with inside diameters of 12.4, 25.4 and 47.5 mm and a wall thickness of 4 mm. Spheres, with a wall thickness of 1 mm were fabricated with inside diameters of 23, 35 and 59 mm. These diameters were chosen to represent the range from small to large tumors observed clinically. For imaging, the cylinders and spheres were suspended by a PMMA support rod within the larger outer cylindrical phantom (see **Figures 4.1** and **4.2**).

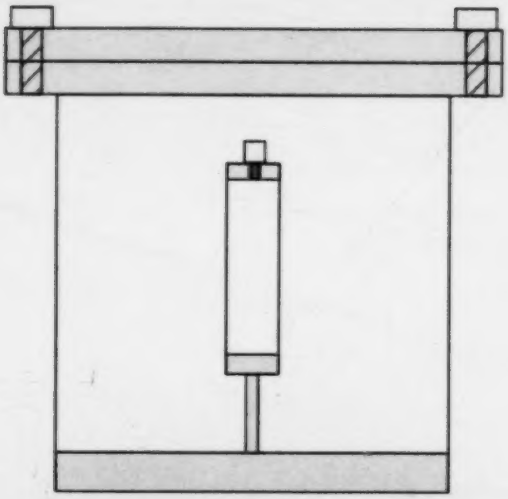

Figure 4.1: Diagram of phantom with the medium cylindrical target centered in the phantom.

Figure 4.2: Photograph of the phantom. Note the pump assembly on the top of the phantom lid.

Both internal and external volumes were filled with F-18 in water suspension. Activity concentrations ratios between internal and external surrounding volumes ranged from approximately 2:1 to 15:1 [internal:external][29,30] in accord with values found in the literature and also seen clinically.

To ensure high quality PET images it is important to use an activity concentration that corresponds to a high noise equivalent count (NEC) rate. The NEC is expressed as the quotient of the square of the number

of true events divided by the total number of events recorded. Higher the NEC values result in better image quality. The NEC has been measured using numerous different methods, each of which results in a different peak in the NEC plot in conjunction with various associated activity concentrations. Published peaks in the NEC curve for the CPET scanner used in this work are associated with activity concentrations that range from 0.0038 to 0.0123 MBq/ml depending on the particular technique used[32]. Measurement of PET image quality usually employs phantoms consisting of target volumes contained within a surrounding background. Target to background activity concentration ratios of between 4:1 and 8:1 are typical for these measurements[32]. Background activity concentrations used experimentally in this work ranged from 0.001 to 0.008 MBq/ml. Target volumes contained activity concentrations ranging from 0.008 to 0.079 MBq/ml. These experimental background activity concentrations thus fall within the range of published peak NEC values for the PET scanner used in this work. Further, these concentrations are similar to those used clinically. A typical 70 kg patient will often be injected with 141-156 MBq of activity. Assuming the patient consists entirely of water this produces an activity concentration of approximately 0.002 MBq/ml.

All measurements were conducted with the axis of rotation of the external cylinder orthogonal to the image plane and coincident with the center of reconstruction. All internal target volumes were either radially centered within the external cylinder, or 32mm or 64mm radially offset from the centre of the external cylinder. The phantom was scanned with a CPET® Plus (Philips Medical Systems) scanner (see **Figure 4.3**) using a clinical whole body protocol (CCI-PET_WB_FF) with a slice width of 4 mm. While a number of other reconstruction algorithms were available, this protocol is the one used to provide images to clinicians upon which current radiotherapy planning augmentation is based. PET data is acquired in a volumetric manner spanning a length of 256 mm in the axial direction. After processing, this data is presented to the user as a series of images which may include axial, coronal and sagittal views. For the majority of this analysis axial images alone are analyzed as these are the common format for comparison with and augmentation of CT data. Images from all three cardinal planes (axial, coronal and sagittal) are employed for the tri-axial iterative threshold technique.

Figure 4.3: Photograph of PET scanner used.

Great care was taken throughout to ensure thorough mixing of F-18 within the water suspension in order to ensure uniform activity distributions both within the target and surrounding background volumes. First the target volumes were partially emptied to allow for the introduction of activity. The activity was then injected and the syringe was rinsed several times by withdrawing and re-injecting the water F-18 solution in the target. Next enough water was added to the target to fill the volume. This process ensured a well mixed target volume. The phantom was mixed using a pump to circulate the water F-18 solution. The pump was contained in a watertight structure at the top of the phantom, see **Figures 4.2** and **4.4**. Each time activity was added to the phantom the pump assembly was allowed to mix the phantom for approximately 30 seconds.

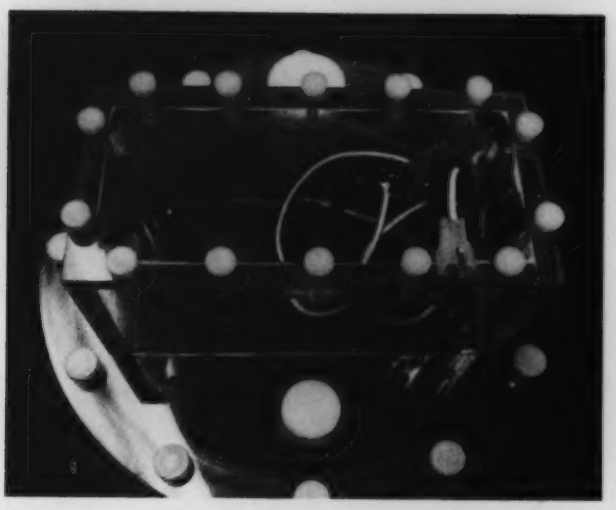

Figure 4.4: Photograph of the pump assembly contained in a watertight structure on the lid of the phantom.

All images were analyzed using an in-house developed Matlab (The MathWorks, Inc., version 7.0.1 release 14 service pack 1) program. Cross sections determined by each of the three segmentation approaches for the cylinders, at a central target volume slice location, and the spheres, at all slice locations throughout their respective volumes, were compared to their true physical values as a function of the activity concentration ratio between target and background and target cross section size. The variability with respect to threshold level was also investigated for the threshold technique. Agreement was deemed to occur when cross sectional areas differed by less than 5 % and their centroids deviated by less than 2 mm.

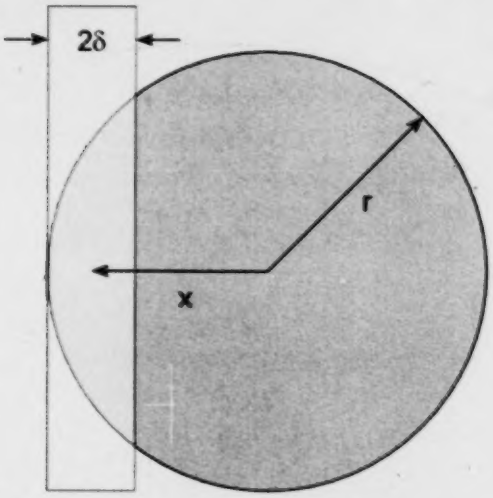

Figure 4.5: The white rectangle, representing a large slice width, demonstrates the difficulty in choosing the physical area, of a spherical target represented by the dark circle, on each image slice.

As the slice thickness, 4mm, of the PET scans is relatively large, the effect of longitudinal (orthogonal to the scan plane) variations in cross section of scanned volumes may not easily be ignored. Each image gathered from a volume of variable cross section will inevitably present partial volume effects even if activity concentrations within sub-volumes are uniform. Slices through the spherical target volumes used here generate images of activity distribution integrated over thick disks of varying diameter, see **Figure 4.5**. The physical area of the sphere represented on any slice image can not simply be taken as the physical area at either end or the geometric middle of the slice, but rather must be determined as a mean weighted area over the volume of the disk. This is done by calculating the mean weighted physical area for each slice according to

$$\overline{A(x)} = \frac{\pi \int_{x-\delta}^{x+\delta} \left(r^2 - x'^2\right) dx'}{\int_{x-\delta}^{x+\delta} dx'} \qquad (4.1)$$

where r is the radius of the sphere, x is the offset from the centre of the sphere and δ is half the slice thickness (see **Figure 4.5**). Solving the above yields

$$\overline{A(x)} = \pi\left[r^2 - x^2 - \frac{\delta^2}{3}\right] \qquad (4.2)$$

Most PET reconstruction computers provide images scaled according to the standardized uptake value, or SUV. Unfortunately, numerous variant definitions of SUV abound within the literature[33,34]. Further, physicians often analyze PET images using only the maximum SUV which occurs within a region. This technique offers little guidance as to the particular SUV value which is most appropriate for use in finding the geometric edges of a target volume[36]. The most likely place for image segmentation to occur for radiotherapy purposes is within a radiation treatment planning system which handles anatomic data on an axial or slice by slice basis[35,36]. Importing PET data into a radiotherapy planning system will, in general, result in the loss of SUV information as the original voxel information is converted to grey scale values for comparison with X-ray CT data. For these reasons raw visual pixel intensities, as opposed to SUV values, were employed for the three segmentation methods examined and the image data was analyzed on a slice by slice basis.

4.1 Thresholding

Partition values τ for segmentation are derived with respect to contrast range which is defined as the difference between maximum pixel intensity IT_{max} within the target and effective mean pixel intensity IB_{mean} of the background region containing the phantom but excluding the target. Note that the contrast range used here is not equivalent to the standard definition of image contrast. The effective mean pixel value of the background region is determined through an examination of the image histogram. **Figure 4.6** shows the frequency distribution of pixel values present in the PET data at the central slice location for the large 47.5 mm target cylinder with a target to background activity concentration ratio of 15:1. The large peak at zero pixel value corresponds to the empty space surrounding the phantom and the null corners of the image matrix which result from mapping the circular reconstruction onto a square image matrix. The second prominent peak centered about a pixel value of 2266 corresponds to the modal pixel value within the phantom, and is chosen to be the effective mean background pixel value. The large gap between the effective mean background peak and the maximum pixel value serves to define the contrast range between

background and target volumes. A fraction or percentage of the contrast range is then used to define the partition value τ at which to perform image segmentation. The partition value τ, more commonly referred to as the threshold level or threshold value, is functionally defined as

$$\text{threshold level } \tau = \left(\frac{\text{threshold \%}}{100}\right)\left(IT_{max} - IB_{mean}\right) + IB_{mean}. \quad \textbf{(4.3)}$$

While this definition of a threshold level is historically non-standard, recent literature[35] has presented definitions similar to **Equation 4.3** in application to PET volume delineation. Target cross sections were thus determined using a simple threshold technique in which all pixels with a value greater than or equal to a specified percentage of the contrast range were deemed as belonging to the volume of interest while all others were designated as constituting the encompassing background.

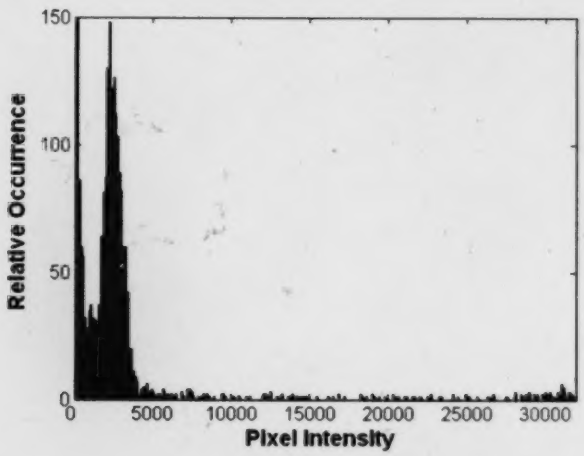

Figure 4.6: Histogram of number of occurrences versus pixel values for a PET image of the large cylindrical target centered in the phantom.

4.2 Sobel

The absolute value of the image gradients $|\nabla I(x, y)|$ are numerically calculated for each pixel in the image. If the absolute value of the gradient at a specific location is greater than some threshold value (12% of the maximum pixel per frame for the cylinders and 12% of the maximum pixel of the entire image set for the spheres) that point is designated a candidate edge point. These lower bounding threshold values

were chosen to eliminate the detection of edges which result from image reconstruction artifacts within the surrounding uniform background volume. This method yields overly thick edges that are thinned through the comparison of the horizontal and vertical partial derivative at each candidate point. If the partial derivative is a maximum in both the horizontal and vertical directions then the candidate point is determined as an edge point. If, however, a maximum exists in only one direction then the point is designated as belonging to an edge only if its magnitude is twice that of the gradient in the other direction[24]. In the case of a horizontal local maximum, for example, one has

$$\left|\frac{\partial I(x,y)}{\partial x}\right| > 2\left|\frac{\partial I(x,y)}{\partial y}\right| \tag{4.4}$$

The Sobel masks

$$\begin{bmatrix} -1 & 0 & 1 \\ -2 & 0 & 2 \\ -1 & 0 & 1 \end{bmatrix} \quad \text{and} \quad \begin{bmatrix} 1 & 2 & 1 \\ 0 & 0 & 0 \\ -1 & -2 & -1 \end{bmatrix} \tag{4.5}$$

are used to analyze the grey scale PET images and yield horizontal and vertical edges respectively.

4.3 Watershed

The watershed technique was applied to the gradient vector flow[28] of each image rather than their respective gradients. Use of the gradient vector flow results in images in which rapid change in pixel intensity are located near edges and thus provides for a more robust analysis[27]. The gradient vector flow of each image is calculated and mapped onto 256 grey levels to allow more efficient processing. The problem of oversegmentation, which often results from simple implementation of the watershed technique, may be avoided through the judicious use of markers which serve to limit the range over which the algorithm can operate. Two sets of markers were employed, the first of which identifies the inner region of the target while the second specifies a location external to the region of interest[26, 27, 29]. Since the results of watershed segmentation are very sensitive to the choice of markers used, an automated method for their identification was implemented. Marker sets were found through an analysis of the images of the original PET data and their respective GVF counterparts. The location of the maximum pixel intensity in each PET image was

found. Target to background activity concentration ratios greater than one guarantee these maximum pixel intensity locations will always lie within the target volume. Next, the GVF pixel intensity at the same location is determined and used to threshold the GVF image. Thresholding was performed such that all pixels with intensity values between the GVF image minimum and the threshold level are included in regions of interest. As pixel intensity values in the GVF image are largest near edge locations and lowest in non-edge regions, this form of thresholding yields two disjoint regions of interest. One of these regions resides within the target volume while the other is located external to it. The watershed algorithm is then applied to that portion of the GVF image which lies between these two regions.

The watershed process begins by setting $C[n] = T[n]$, where $n = \min+1$. The process then iterates from this point by increasing the gradient level n by one. The flooded level which results is calculated using **Equation (3.13)**. A set Q is then defined as containing all the connected components in $T[n]$. The intersection of each connected component $q \in Q[n]$ with $C[n-1]$

$$q \cap C[n-1] \tag{4.6}$$

yields three possible results; the null set, a set containing a single connected component, or a set containing multiple connected components. The null case indicates a new minimum has been found which is added to $C[n-1]$ to form $C[n]$. A single connected component signifies inclusion within one of the known catchment basins. This point will be added to $C[n]$ by forming the union of q and $C[n-1]$. Multiple intersection elements occur when a ridge has been found. A dam must be built at this level in order to prevent the merging of distinct catchment basins.

Dams are constructed by dilating $q \cap C[n-1]$ with a 3x3 structuring element of ones. The dilation must be constrained to allow only the dilation of points within q and must not be performed on points that would result in the union of two connected components. If these two constraints are satisfied, a dam location has been found. Dams are built by setting the pixels at boundary locations to a value of $\max+1$. The process iterates until $n = \max+1$.

5. Experimental Results and Discussion

5.1 Introduction

Data was gathered for three sizes of cylindrical and spherical targets at three radial positions in the phantom. The effect of multiple targets was also analyzed using two similarly shaped targets in the phantom at the same time. Results will be presented for each of the three segmentation techniques: thresholding, Sobel edge detection and the watershed technique. Thresholding results will first be presented for the three cylindrical targets centered in the phantom, next the effect of offset on the ideal threshold is examined, and then the effect of multiple cylindrical targets will be demonstrated. The thresholding results for the spheres will be presented in the same order. Next the Sobel segmentation results will be presented for the cylindrical targets followed by the spherical targets centered in the phantom. Finally the watershed segmentation results will be presented for both the cylindrical and spherical targets also centered in the phantom.

5.2 Thresholding

5.2.1 Cylinders

Experimental cross sectional diameters as a function of threshold for the three cylinders over the range of target to background activity concentration ratios, from about 3:1 to approximately 15:1, investigated and generated by averaging experimental diameters measured along the length of the target cylinder, are presented in **Figures 5.1a**, **5.1b** and **5.1c**. Also indicated is the true physical diameter of each cylinder. The target cylinders were initially located with their axes of rotation coincident with that of the external cylindrical phantom. As seen in **Figure 5.1** measured diameter can vary dramatically as a function of both threshold level and, to a lesser degree, the ratio of target to background activity concentration densities. The variation with activity concentration ratio is least for the largest cylinder and greatest for the smallest cylinder. For the smallest cylinder, threshold levels which yield correct diameters (within experimental error) vary from about 40% to approximately 65%. Threshold levels which correspond to correct diameter

determination for the medium sized cylinder range from about 30% to 40%. For the largest cylinder the threshold interval which yields correct physical diameters narrows to approximately 34% to 40%.

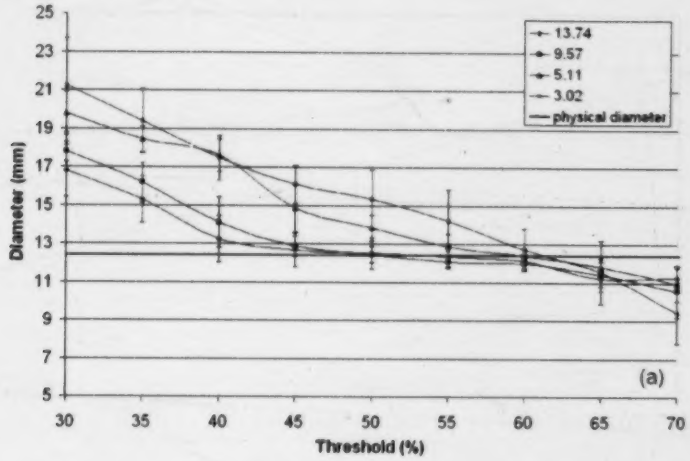

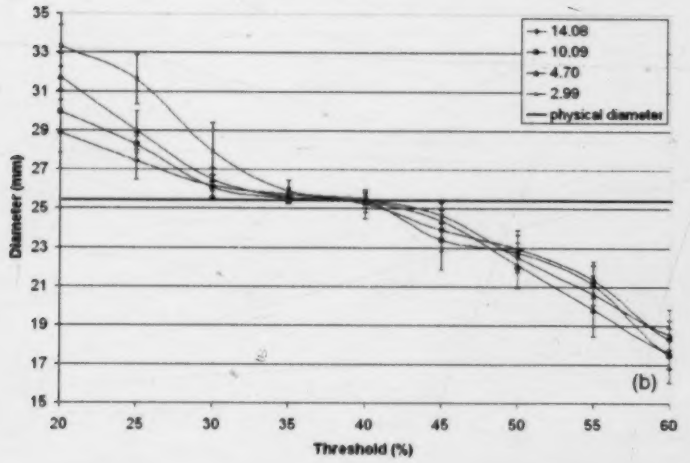

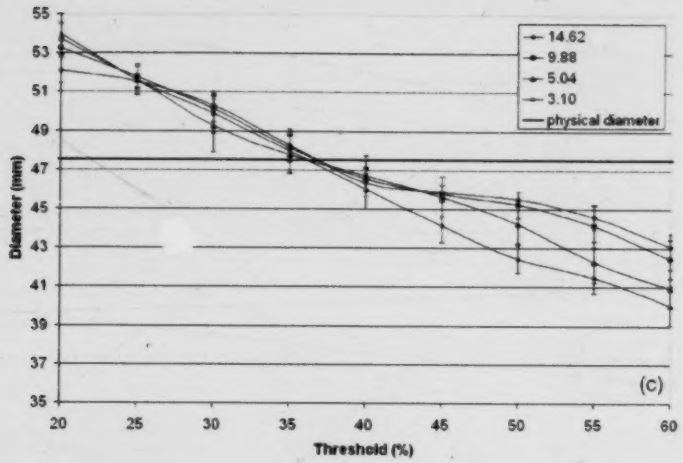

Figure 5.1: Calculated diameter versus threshold for the (a) small, (b) medium, and (c) large cylinder for different target to background activity concentration ratios.

The effect of radial offset for the three target cylinders is demonstrated in **Figures 5.2** through **5.6**. The data presented in these graphs is representative of the entire data set covering the three offset values (0 mm, 32 mm and 64 mm) for each combination of cylinder size and target to background activity concentration ratio. Here the offset value refers to the radial distance between the rotational axes of the outer encompassing cylindrical volume and inner target cylinders. It can be seen from these graphs that the results for the 32mm and 64mm offset positions agree within error to the central position (0 mm) with but a few exceptions. Therefore, the effect of offsetting the target in the phantom is deemed very small.

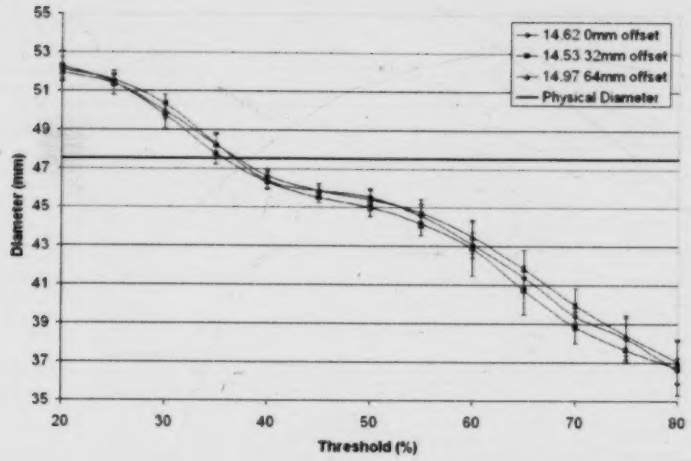

Figure 5.2: Ideal threshold versus physical area for the large cylinder at three radial offsets, 0mm, 32mm and 64mm, for a target to background activity concentration ratio of approximately 15:1.

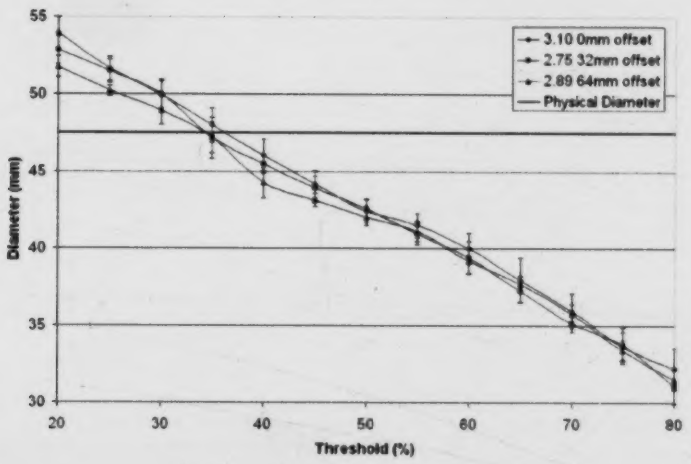

Figure 5.3: Ideal threshold versus physical area for the large cylinder at three radial offsets, 0mm, 32mm and 64mm, for a target to background activity concentration ratio of approximately 3:1.

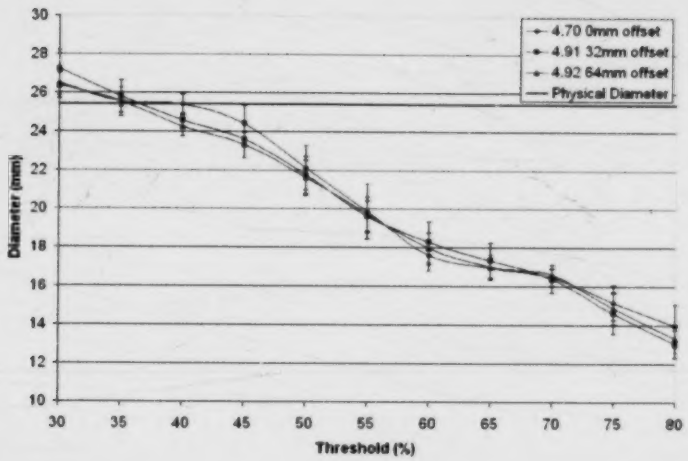

Figure 5.4: Ideal threshold versus physical area for the medium cylinder at three radial offsets, 0mm, 32mm and 64mm, for a target to background activity concentration ratio of approximately 5:1.

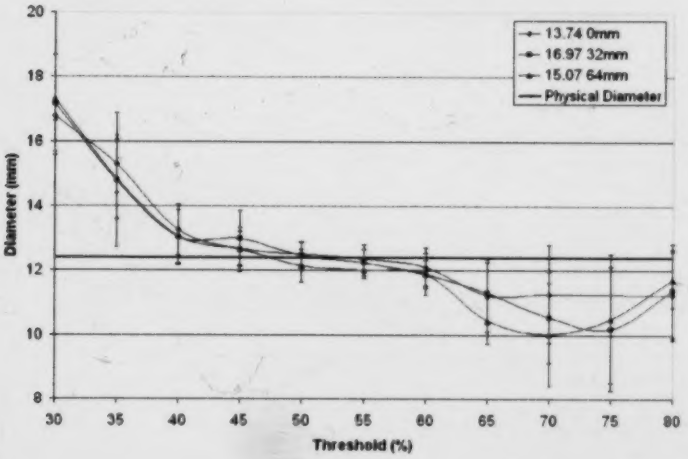

Figure 5.5: Ideal threshold versus physical area for the small cylinder at three radial offsets, 0mm, 32mm and 64mm, for a target to background activity concentration ratio of approximately 15:1.

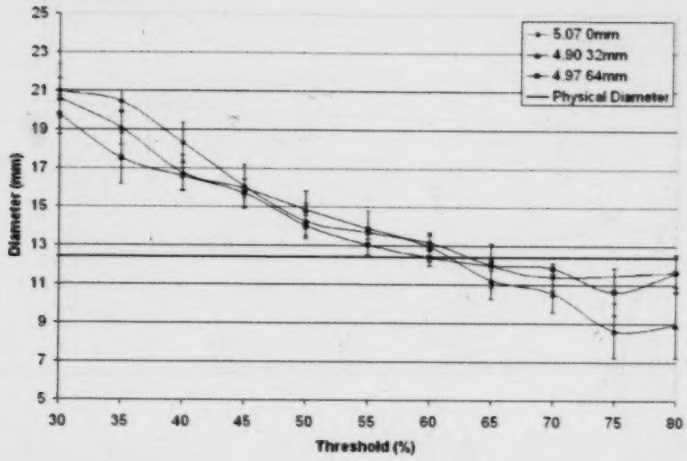

Figure 5.6: Ideal threshold versus physical area for the small cylinder at three radial offsets, 0mm, 32mm and 64mm, for a target to background activity concentration ratio of approximately 5:1.

Table 5.1 summarizes the ideal threshold values (those which yield the correct cross sections) for the entire radial offset data set covering the three offset values (0 mm, 32 mm and 64 mm) for each combination of cylinder size and target to background activity concentration ratio. From **Table 5.1** it can be seen that the ideal threshold is largest for small target to background ratios for the small cylinder. Maximum differences in ideal threshold value as a function of radial position occur for the medium cylinder, with the greatest variation seen at the target to background ratio of 3:1. Apart from these generalities no discernable relationship between ideal threshold and radial position may be identified which is consistent amongst all the cylinders. In all but three cases the ideal thresholds at each radial position agree within experimental uncertainty for a given target to background activity concentration ratio. In those instances where agreement in ideal threshold value is not observed at all three radial positions, disagreement is realized at only a single location. Ideal threshold values which disagree with their other two counterparts are shown in bold italicized text.

		Radial Distance from Axis (mm)		
	Ratio	0	32	64
Large Cylinder	15	37.0±0.7	35.9±0.5	37.3±0.5
	10	37.0±0.9	35.8±0.6	37.6±0.7
	5	36.4±1.4	34.0±1.4	***38.4±1.1***
	3	36.2±1.4	34.4±1.2	34.0±1.5
Medium Cylinder	15	38.3±1.6	35.5±1.4	36.1±2.1
	10	40.1±3.7	35.1±1.4	35.0±1.7
	5	***39.6±1.3***	36.6±1.4	35.5±1.4
	3	40.5±1.5	40.5±3.7	***33.6±1.7***
Small Cylinder	15	54.1±3.1	51.5±3.0	47.5±3.8
	10	50.6±2.5	55.5±7.9	56.5±4.5
	5	59.8±4.2	61.7±8.3	60.0±3.8
	3	61.4±13.5	63.2±10.3	61.7±52.6

Table 5.1: Ideal threshold values for large, medium and small cylinder at three radial offsets and multiple target to background activity concentration ratios.

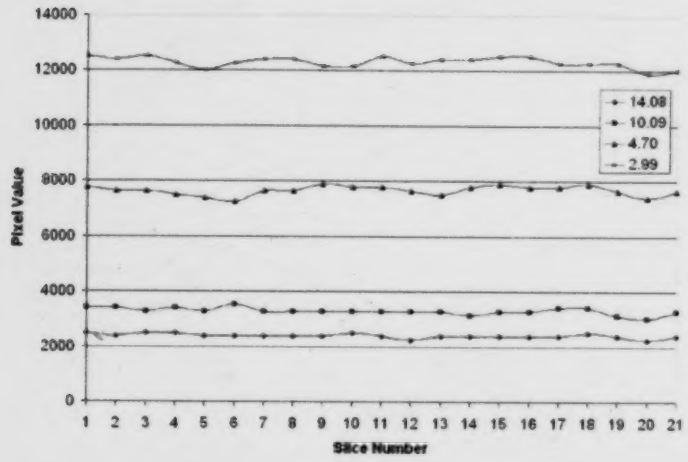

Figure 5.7: Mean background pixel intensity along the length of the medium cylinder centered in the phantom for different target to background activity concentration ratios.

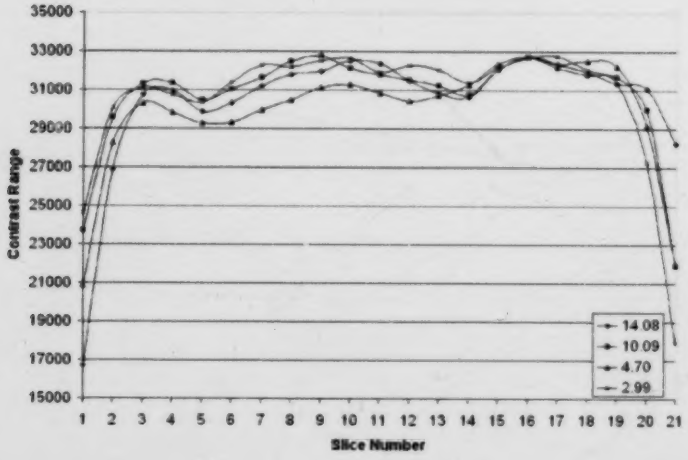

Figure 5.8: Contrast range along the length of the medium cylinder centered in the phantom at different target to background activity concentration ratios.

When data from a single acquisition spanning the full length of each cylinder is examined on a slice by slice basis, significant variations in both mean background pixel value and contrast range are observed. Representative of the variability encountered are the results for the medium cylinder, located at the radial center (0 mm offset) of the external volume, as shown in **Figures 5.7** and **5.8**. **Figure 5.7** reveals the

variation in mean background pixel intensity as a function of slice number of the image data set. **Figure 5.8** demonstrates the contrast range, the difference between the maximum pixel intensity and the mean background pixel intensity, at each slice location. Great care was taken in phantom preparation to ensure the uniform distribution of activity throughout both target and surrounding background volumes. The large spread in these variables results from the particular imaging properties of the PET scanner in combination with differential scattering properties which exist throughout the volume of the phantom and the statistical nature of PET imaging in general. This variability translates directly into the identification of slice location as a functional variable further affecting the threshold value required for accurate target segmentation and is the likely cause of the few radial position discrepancies (greater than experimental error) seen above. Threshold values that yield correct cross sectional areas as a function of slice location for the three cylinders are shown in **Figures 5.9a**, **5.9b**, and **5.9c**. Variations in required contrast level of greater than 15% are observed for some target to background activity concentration ratio combinations, as seen in **Figures 5.9 a-c**. That any given plot on these three graphs is derived from a single volumetric data set is indicative of the variability inherent in PET and the difficulty which may be anticipated when automated threshold segmentation is contemplated.

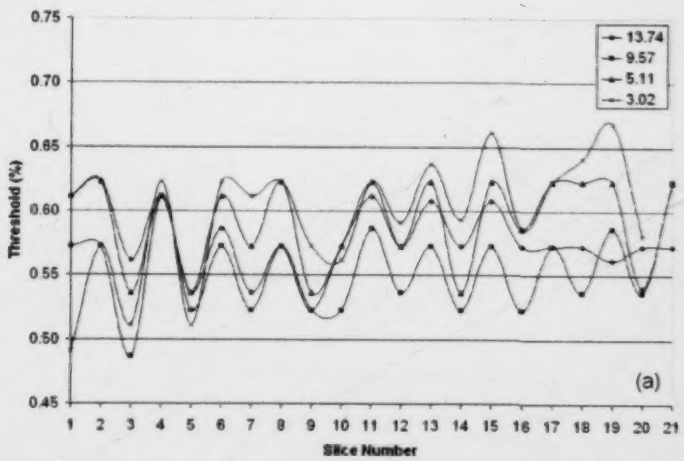

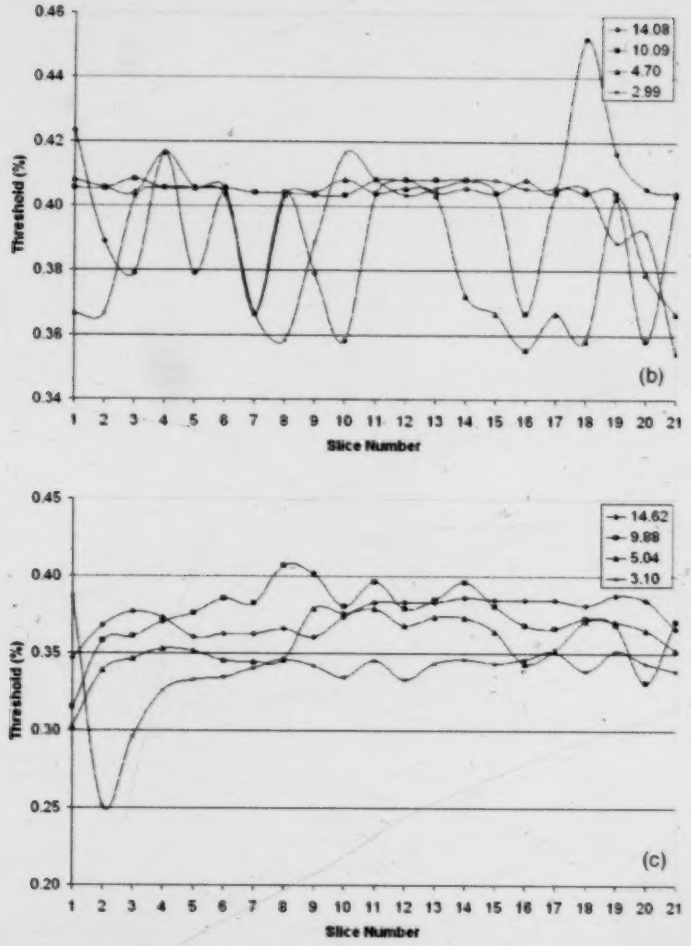

Figure 5.9: Threshold values that produce the correct physical area versus slice number for the (a) small, (b) medium, (c) large cylinders centered in the phantom for different target to background activity concentration ratios.

The effect of a confounding region of activity on the diameter versus threshold results of the cylindrical target volumes was also examined. Several combinations of confounding and target cylinders were studied: two large cylinders, two medium cylinders, a large cylinder centered in the phantom with a medium cylinder offset 64mm and a small cylinder centered in the phantom with a large cylinder offset 64mm. The centres of the cylinders were separated by 64mm for all cases except for the two large cylinders, which were separated by 128mm. With these results the 'hot' cylinder contains approximately

two times the concentration of activity as the 'cold' cylinder. The results for these combinations are shown in **Figures 5.10** through **5.14**. The results for a large confounding cylinder with a small target cylinder will be discussed. The large confounding cylinder was given an activity concentration one and a half times greater than that of the small target cylinder. This combination provided the largest observable effect on the thresholding results. The small target cylinder was centered in the phantom with the large confounding cylinder 64mm radially offset from the centre. This provides a gap of just over 26mm between the small and large cylinders and represents the closest arrangement which was possible between these two volumes with the physical setup available. **Figure 5.14d** shows the diameter versus threshold results for a three to one target to background activity concentration ratio for both the small target cylinder with the large confounding cylinder in the phantom as well as the results for the solitary small cylinder. Results obtained with the nearby confounding hot volume present agree within experimental error with those of the solitary target cylinder at all but one threshold value. Thus the effect of a large, hot, nearby confounding volume is seen to be negligible, which also holds for the other target and confounding volume configurations.

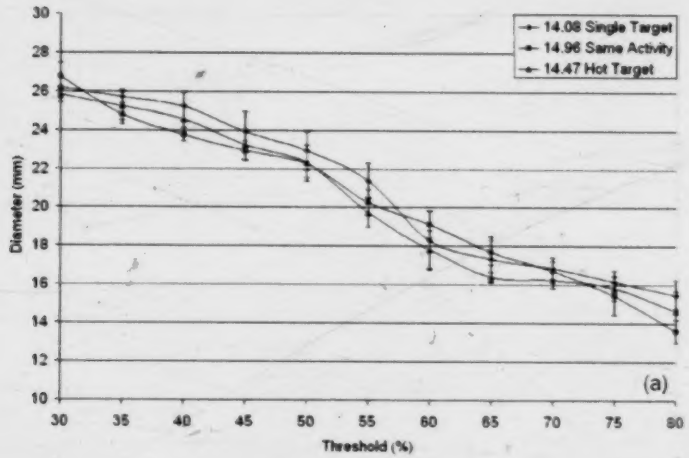

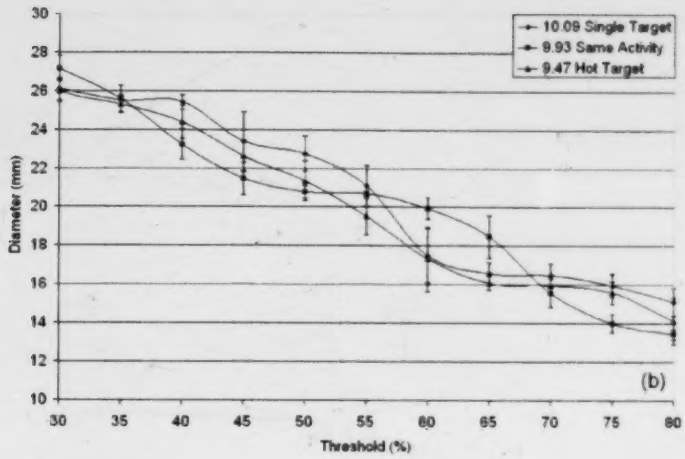
10.09 Single Target
9.93 Same Activity
9.47 Hot Target
Diameter (mm)
Threshold (%)
(b)

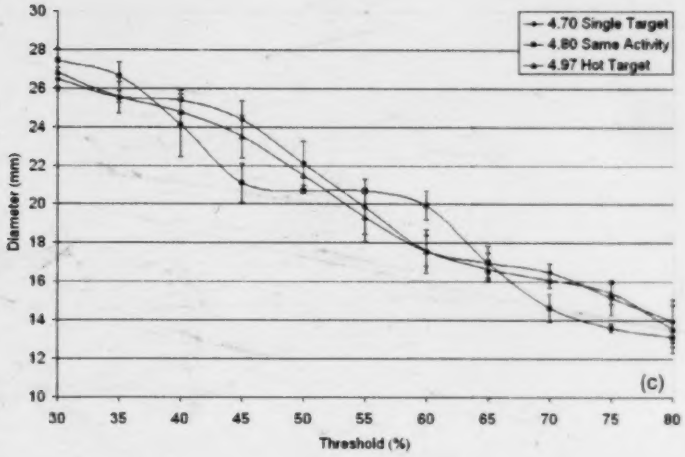
4.70 Single Target
4.80 Same Activity
4.97 Hot Target
Diameter (mm)
Threshold (%)
(c)

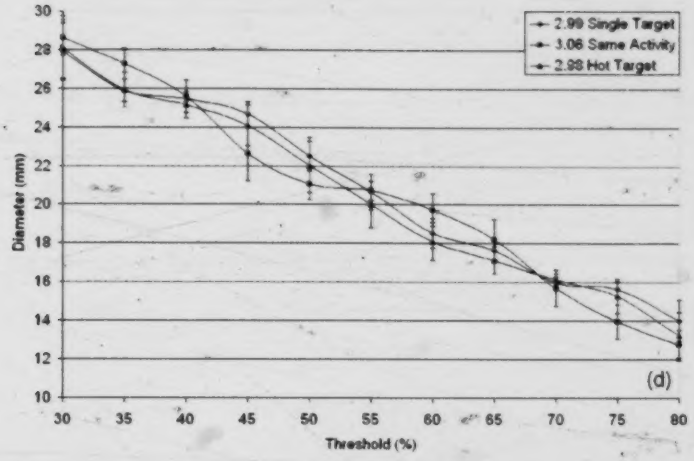

Figure 5.10: Diameter versus threshold for a medium target cylinder with a medium confounding cylinder for different target to background activity concentration ratios (a)-(d). Target centered in the phantom, confounding volume 64mm offset from centre.

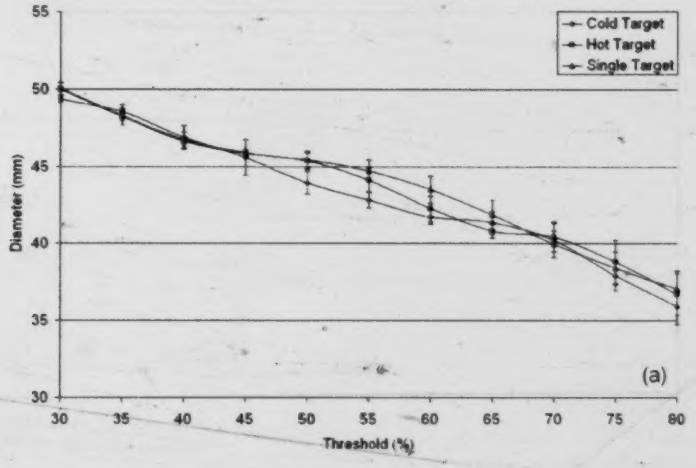

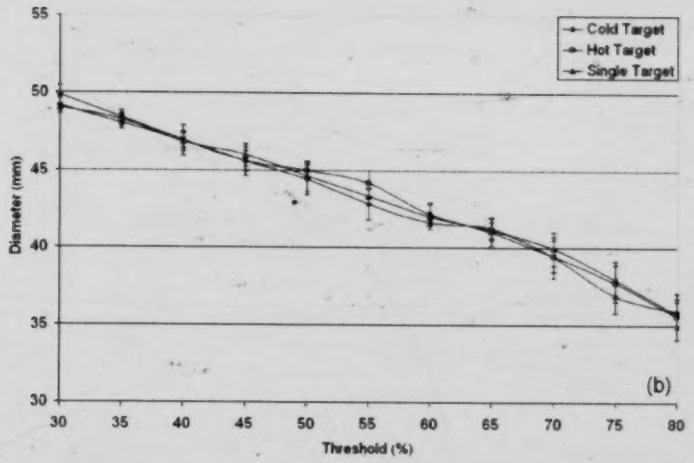
Cold Target
Hot Target
Single Target
Diameter (mm)
Threshold (%)
(b)

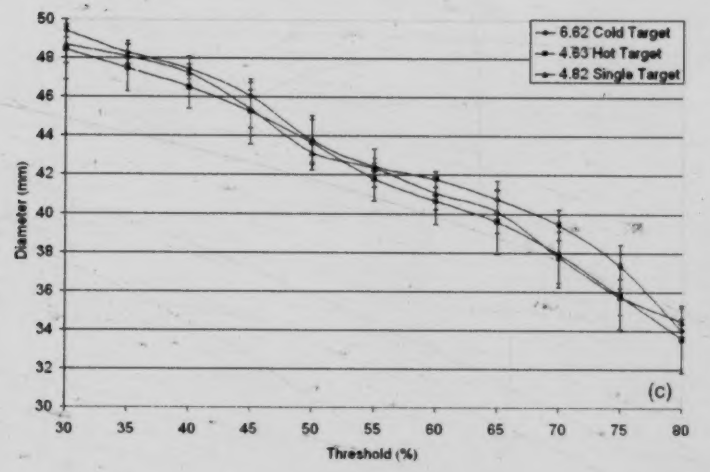
6.62 Cold Target
4.83 Hot Target
4.82 Single Target
Diameter (mm)
Threshold (%)
(c)

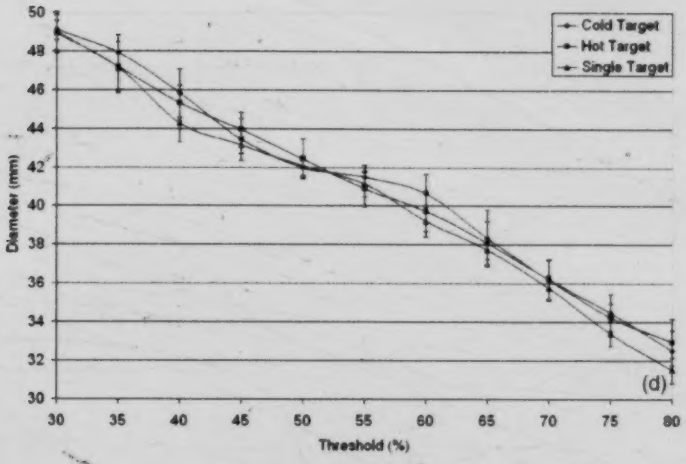

Figure 5.11: Diameter versus threshold for a large target cylinder with a large confounding cylinder for different target to background activity concentration ratios (a)-(d). Target offset 64mm from centre of phantom, confounding volume 128mm from centre of target

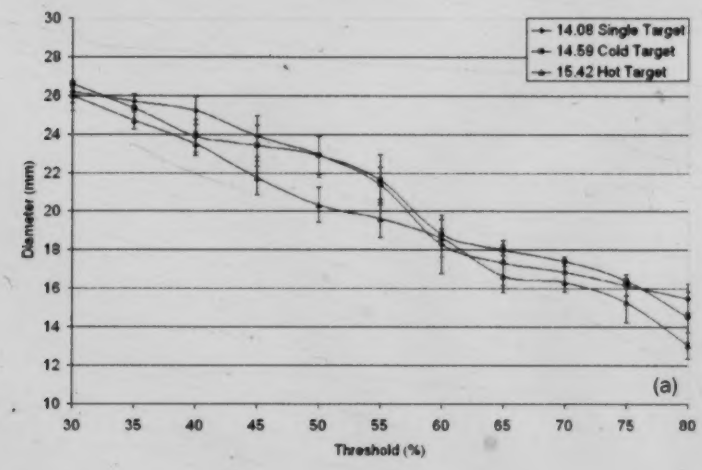

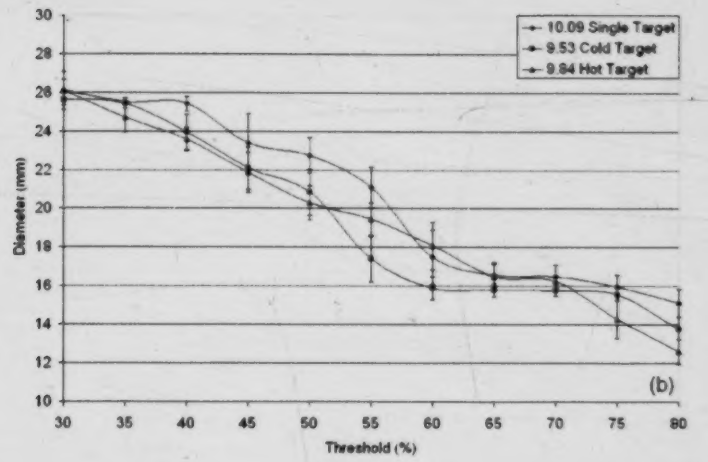
10.09 Single Target
9.53 Cold Target
9.84 Hot Target
Diameter (mm)
Threshold (%)
(b)

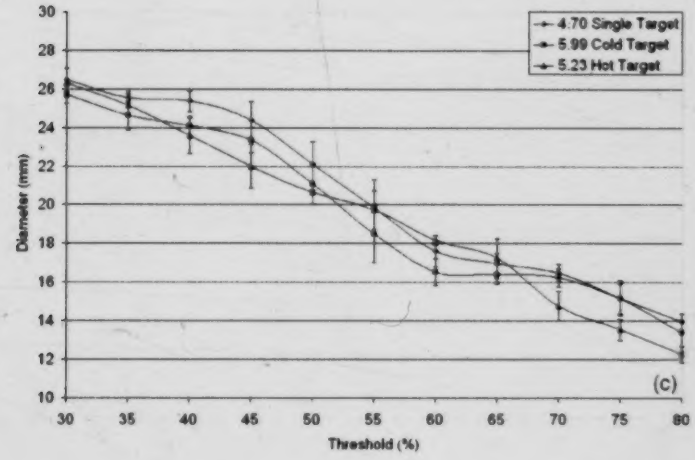
4.70 Single Target
5.99 Cold Target
5.23 Hot Target
Diameter (mm)
Threshold (%)
(c)

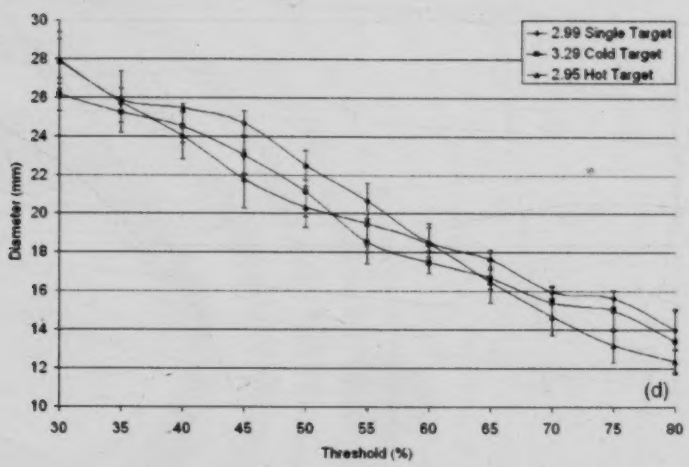

Figure 5.12: Diameter versus threshold for a medium target cylinder with a large confounding cylinder for different target to background activity concentration ratios (a)-(d). Target offset 64mm from centre of phantom, confounding volume centered in phantom.

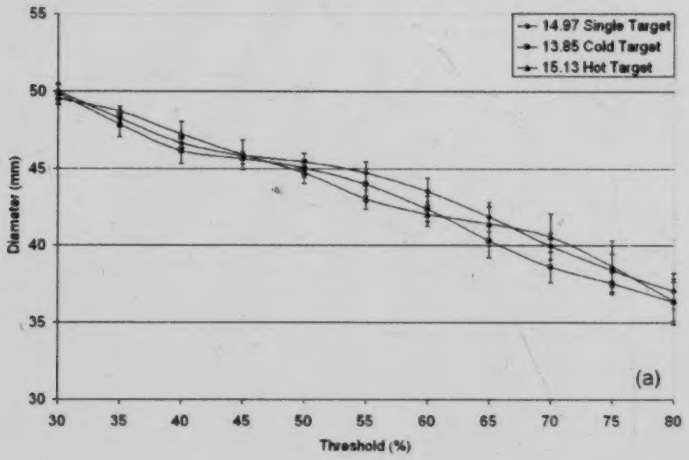

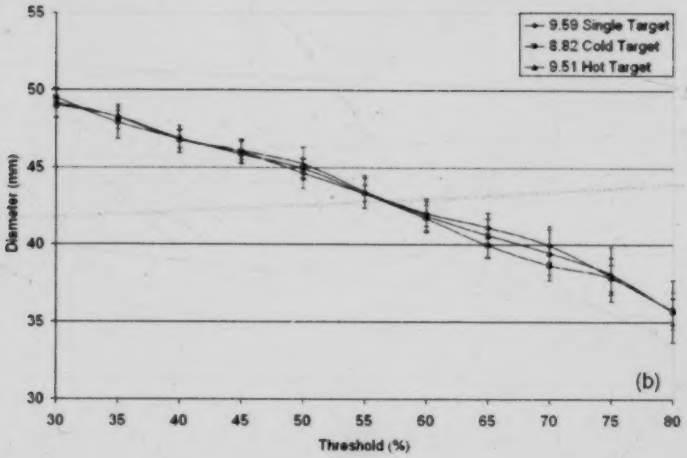
9.59 Single Target
8.82 Cold Target
9.51 Hot Target
Diameter (mm)
55
50
45
40
35
30
30 35 40 45 50 55 60 65 70 75 80
Threshold (%)
(b)

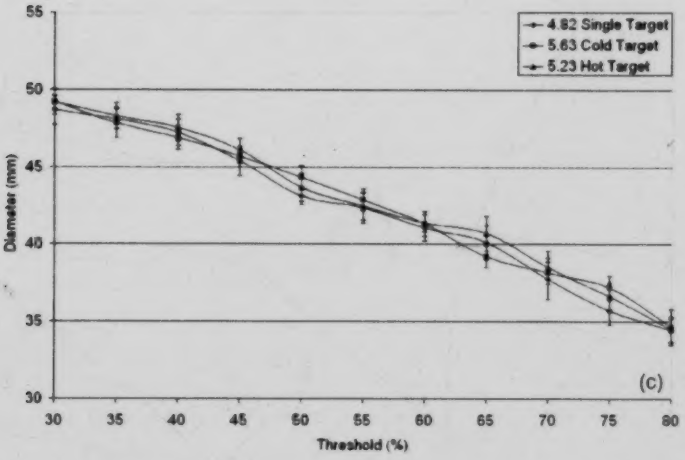
4.82 Single Target
5.63 Cold Target
5.23 Hot Target
Diameter (mm)
55
50
45
40
35
30
30 35 40 45 50 55 60 65 70 75 80
Threshold (%)
(c)

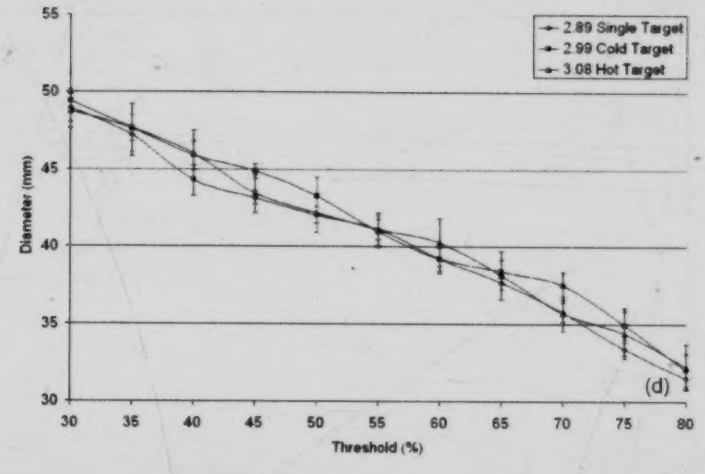

Figure 5.13: Diameter versus threshold for a large target cylinder with a medium confounding cylinder for different target to background activity concentration ratios (a)-(d). Target centered in phantom, confounding volume offset 64mm from centre of phantom.

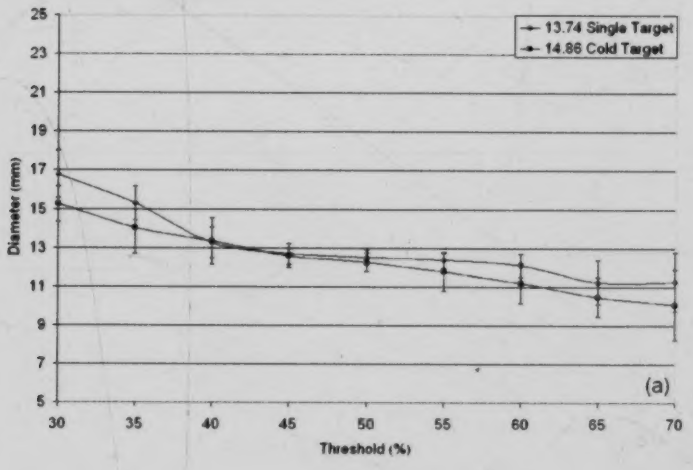

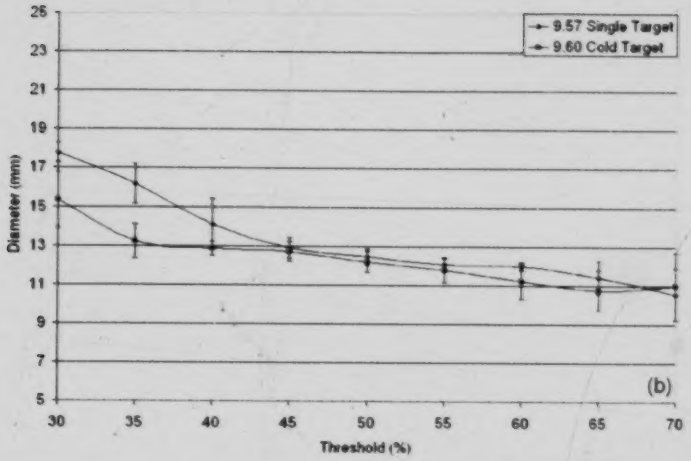
9.57 Single Target
9.60 Cold Target
Diameter (mm)
Threshold (%)
(b)

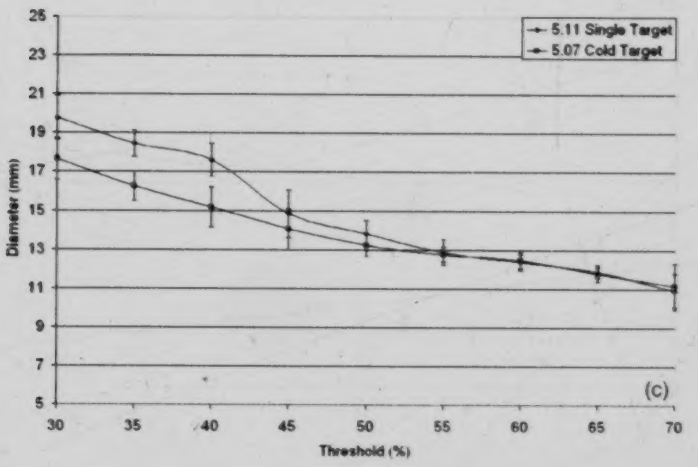
5.11 Single Target
5.07 Cold Target
Diameter (mm)
Threshold (%)
(c)

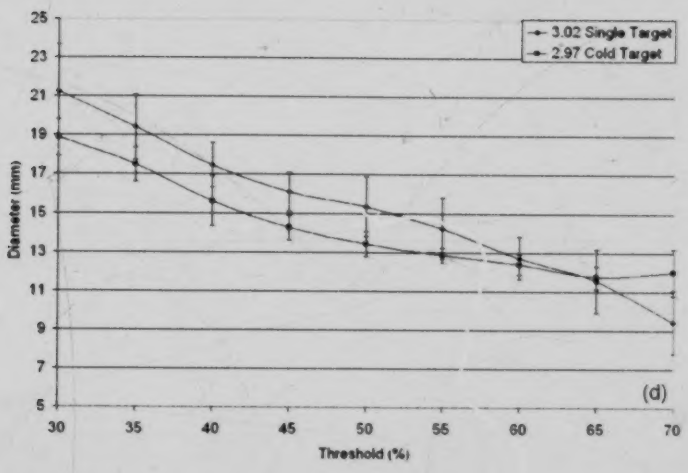

Figure 5.14: Diameter versus threshold for a small target cylinder with a large confounding cylinder for different target to background activity concentration ratios (a)-(d). Target centered in phantom, confounding volume offset 64mm from centre of phantom.

5.2.2 Spheres

Spherical volumes present variable cross sectional area as a function of slice location and hence, based upon the preceding results obtained with cylinders, are ineligible for the application of a single threshold level for correct geometric delineation. Interestingly, single threshold values may be identified in some cases which yield correct total volumes. In these cases, however, the indicated singular threshold level yields cross sectional areas as a function of slice location for which some are greater than, and others less than, their true value, see **Figures 5.15**, **5.16**, and **5.17**. By happenstance the errors generated by the application this global threshold cancel out and the sub-volumes (the product of cross sectional area and slice width) defined at each slice location erroneously sum to the correct total value within experimental error, this effect becomes more apparent when smaller spherical targets are contemplated. The only two papers which have been identified in the literature to date which address PET segmentation are both predicated upon the use of a single threshold value to yield correct volumetric delineation[31,37]. The results presented here strongly suggest that the conclusions drawn in these two publications should be reconsidered.

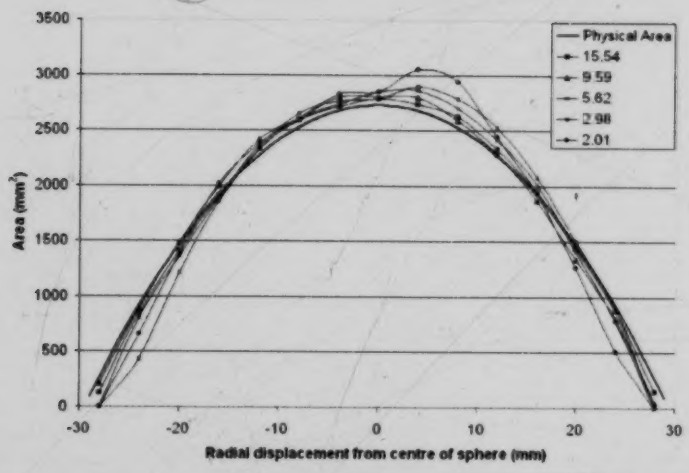

Figure 5.15: Area calculated using a threshold value that produces the correct volume versus the radial displacement from the centre of the large sphere for different target to background activity concentrations.

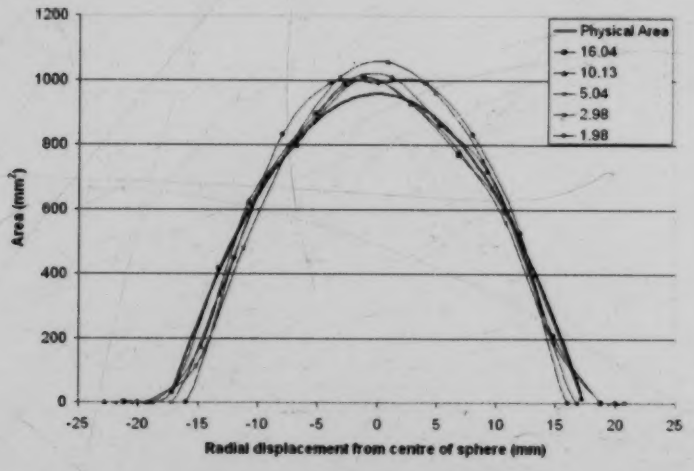

Figure 5.16: Area calculated using a threshold value that produces the correct volume versus the radial displacement from the centre of the medium sphere for different target to background activity concentrations.

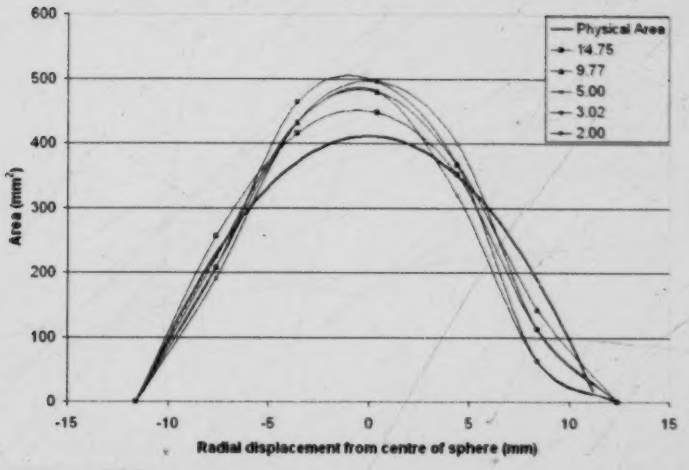

Figure 5.17: Area calculated using a threshold value that produces the correct volume versus the radial displacement from the centre of the small sphere for different target to background activity concentrations.

Two methods of slice specific threshold determination were investigated. For brevity sake only results derived from spheres located at the central radial position of the imaging phantom are presented. The effects of radial position are examined later and found to be similar to those observed with cylindrical volumes.

The first approach to determining the ideal threshold value at each slice location employs the use of a single common contrast range derived from the histogram of the centrally located image (largest cross section) for each sphere. This position also presents the largest contrast range of any slice location. Based upon this contrast range, the contrast level required to yield correct cross sectional area at each slice location is determined and the results are presented in **Figures 5.18(a-c)** for the small, medium and large spheres respectively. Here, and in **Figures 5.19(a-c)**, to follow, the two threshold values from each pair of corresponding slice locations symmetric about the center of each sphere are averaged to yield the mean threshold value required as a function of physical cross sectional area. The error bars associated with each data point reflect the standard deviation between pairs of threshold value. Using a single common contrast range defined on the central slice of the sphere, the general trend of lower thresholds required with smaller cross sections and higher levels associated with larger cross sectional areas is observed in Figures **5.18(a-**

c). Applying the largest contrast range throughout, as derived from the central slice location, necessitates a diminishing ideal threshold level as cross sectional areas decrease. Ideal threshold levels indicated by this method range from less than 10% to more than 42%.

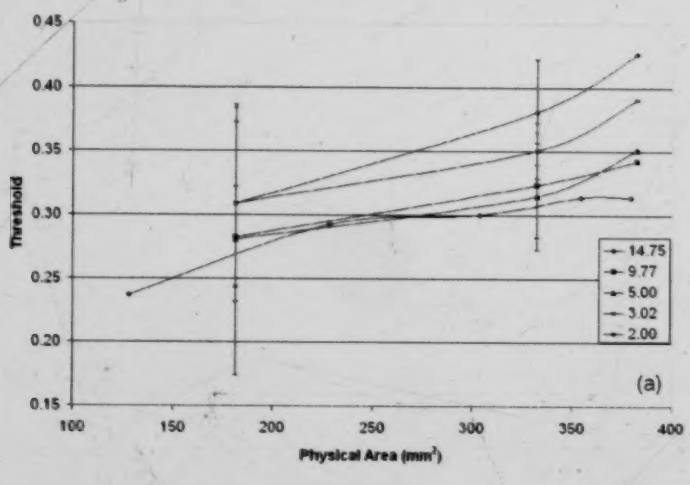

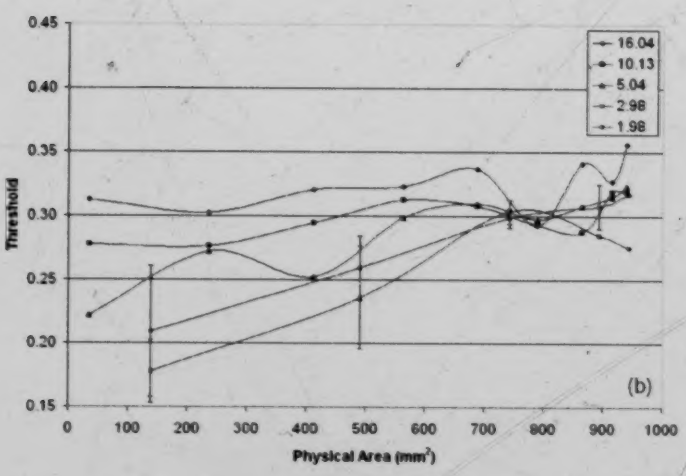

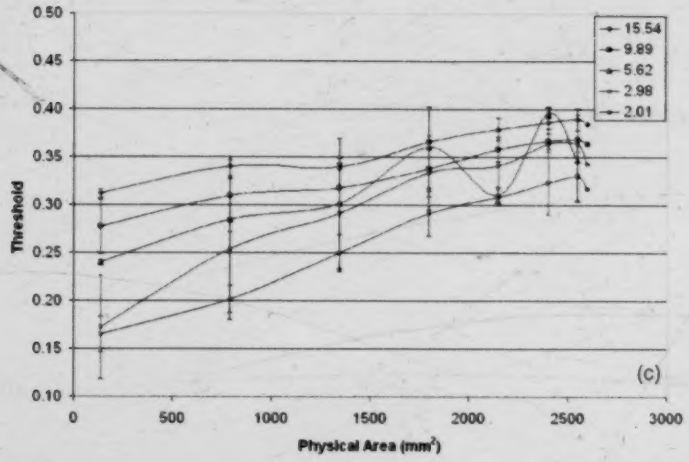

Figure 5.18: Ideal threshold based on the central slice contrast range, versus the physical area for the (a) small, (b) medium, and (c) large sphere.

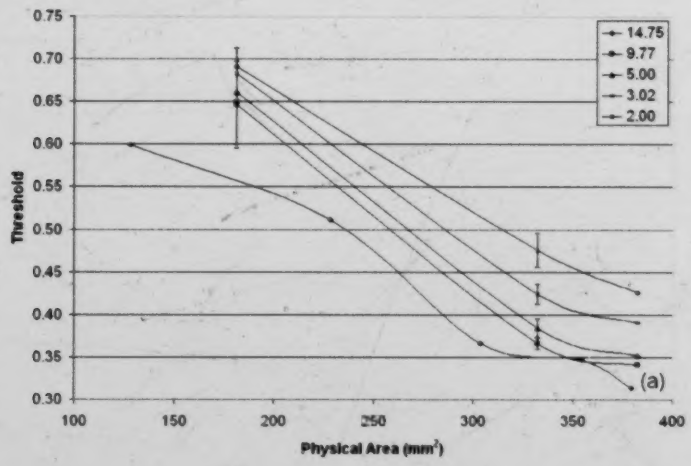

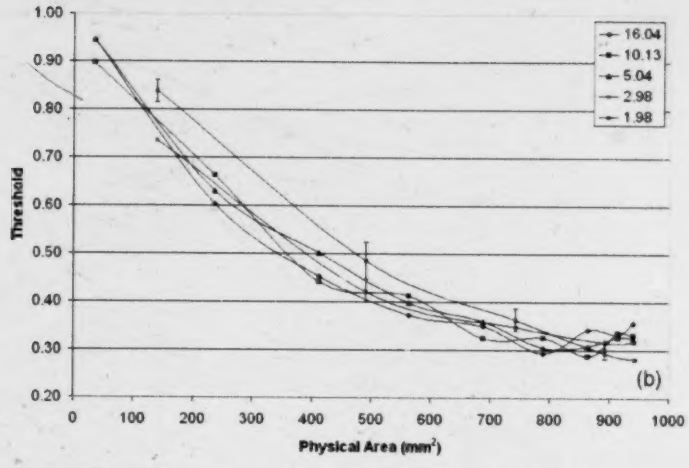

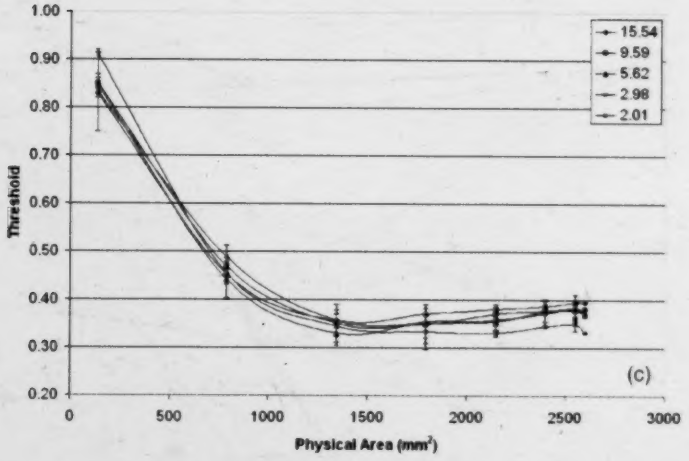

Figure 5.19: Ideal threshold based on the contrast range from each slice, versus the physical area for the (a) small, (b) medium, and (c) large sphere.

The second approach to a producing slice specific threshold values which faithfully reproduce physical cross sections is based upon the contrast range derived from each individual image. Proceeding in this manner yields the results presented in **Figures 5.19(a-c)** for the small, medium and large spheres respectively.

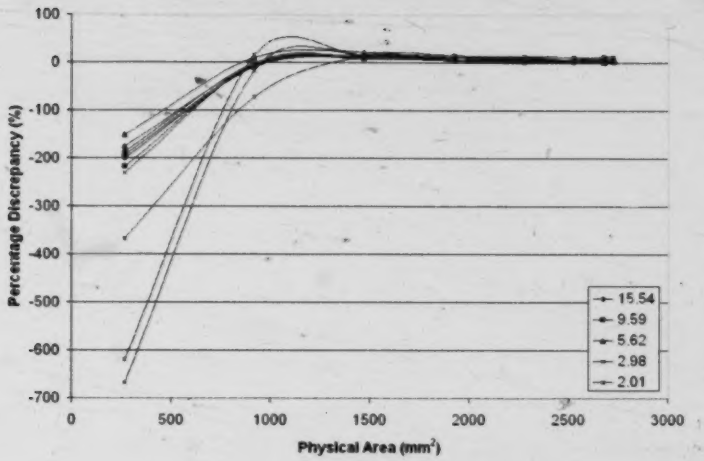

Figure 5.20: Percentage error, (physical area-measured area/physical area)*100%, between the true physical area and the calculated area by applying a single mean threshold to the large sphere.

A much larger variability in ideal threshold is seen with this methodology in comparison to the single contrast range approach. The trend observed, proceeding from large thresholds required with smaller cross sections to smaller thresholds associated with larger cross sectional areas, is opposite to that seen with the single contrast range calculation method. This effect is a direct result of the decrease in contrast range associated with smaller target cross sectional areas which, in turn, necessitates increases in ideal threshold levels. The greatest variation in cross sectional area occurs with the largest sphere. Here the ideal threshold levels decrease rapidly from a maximum in excess of 90% near the periphery of the sphere where target areas are smallest, pass through a minimum of about 35% at intermediate dimensions and rise slowly thereafter as cross sectional areas increase further. Over the region of this slow rise one might expect that a single suitably chosen mean threshold level would yield cross sectional data of reasonable accuracy. This same level will, however, surely fail at slice locations corresponding to smaller cross sections of the sphere where ideal threshold values depart dramatically from their more sedately varying counterparts. The error in doing so is illustrated in **Figure 5.20** where the percentage difference between measured and true cross sectional areas is plotted as a function of physical cross section for this large sphere. The single threshold value applied here is the mean of all values in **Figure 5.19c** in the range between 30% and 40%, and results in overestimation of cross sectional areas nearest the periphery of the sphere. While the percentage error

incurred in these regions is exceedingly large, their exaggerated contribution results in measured total volumes of only 0.01% to 4.4% greater than their true physical values. These results suggest that in the arena of clinical application, where neither tumor size nor the activity concentration ratio between tumor and background are well known at the outset, use of a single threshold level may be applied subject to the caveat that doing so will overestimate target cross sections. In order to minimize the possibility of geometric miss based upon PET derived target volumes one must ensure that no cross sectional areas are underestimated. Achieving this necessitates use of the smallest ideal threshold observed in association with all three spheres. The degree of overestimation resulting from this methodology will be greatest for smallest cross sections which contribute least to determination of overall volume. Examination of **Figures 5.19(a-c)** reveals 28% as the lowest ideal threshold (medium sphere) over all three spheres. Universal application of this minimum threshold level results in measured volumes for the three spherical volumes examined as much as 108% in excess of their true value. The greatest errors between measured and true volumes occur for the medium and small spheres at low target to background activity concentration ratios. The error associated with this approach is illustrated in **Figures 5.21(a-c)** where the percentage difference between measured and true cross sectional areas is plotted as a function of physical cross section for each sphere. **Figures 5.22(a-c)** shows the physical area per slice plotted against slice number obtained by applying the single 28% threshold. A summary of the results for each sphere and target to background activity concentration ratio combination is presented in **Table 5.2**. Also indicated are the absolute volumes of surrounding background encompassed by this segmentation approach. Application of this methodology is contraindicated when a single contrast range is applied throughout each volume (**Figures 5.18(a-c)**). In this case, the use of a maximum threshold value is required if large cross sections are not to be overestimated, but doing so will result in dilation of measured smaller cross sections in comparison to their true value. This will result in failure to delineate the full extent of the tumor leading to the possibility of geometric miss. While the use of a minimum threshold would ensure that no cross sections are underestimated, an exaggeration of large cross sections which contribute most to overall volume would result. Doing so would include even greater amounts of uninvolved surrounding tissue within target volumes than result with the slice specific contrast range method.

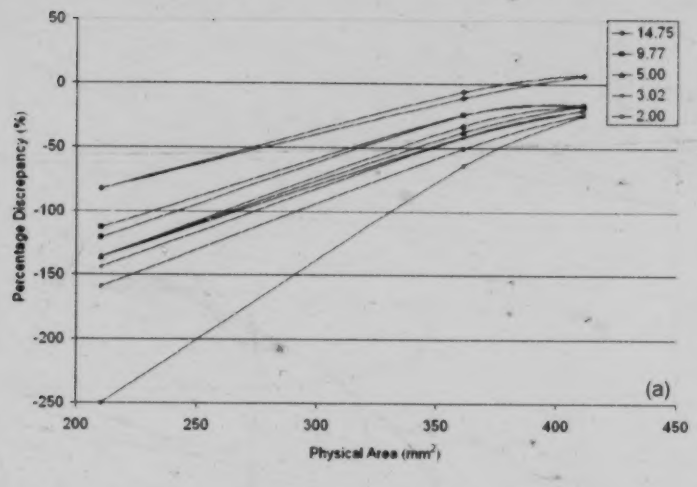
14.75
9.77
5.00
3.02
2.00
Percentage Discrepancy (%)
50
0
-50
-100
-150
-200
-250
200
250
300
350
400
450
Physical Area (mm²)
(a)

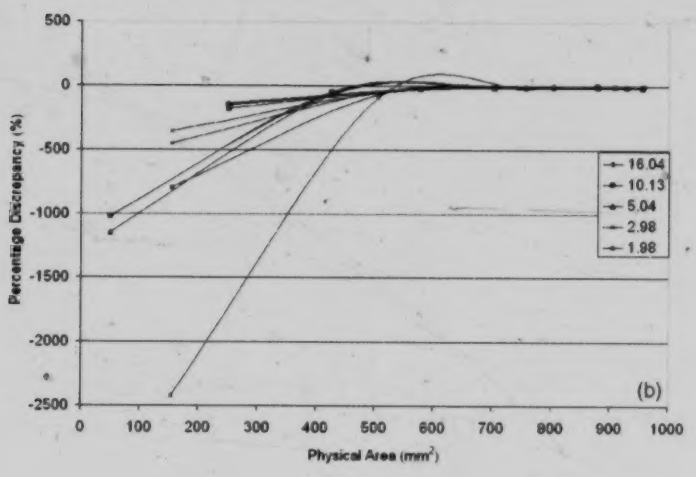
16.04
10.13
5.04
2.98
1.98
Percentage Discrepancy (%)
500
0
-500
-1000
-1500
-2000
-2500
0
100
200
300
400
500
600
700
800
900
1000
Physical Area (mm²)
(b)

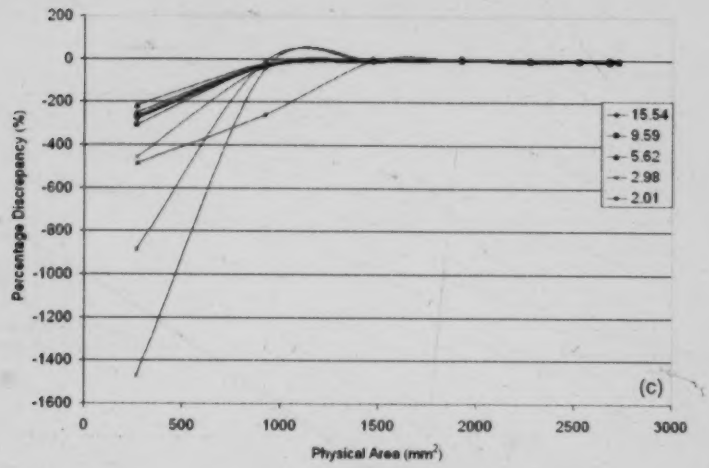

Figure 5.21: Percentage difference, (physical area-measured area/physical area)*100%, between measured and true cross sectional areas versus the physical cross section for the (a) small, (b) medium, and (c) large sphere.

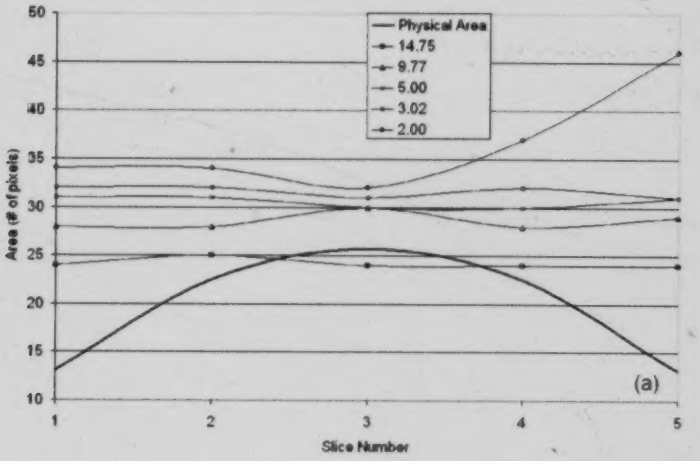

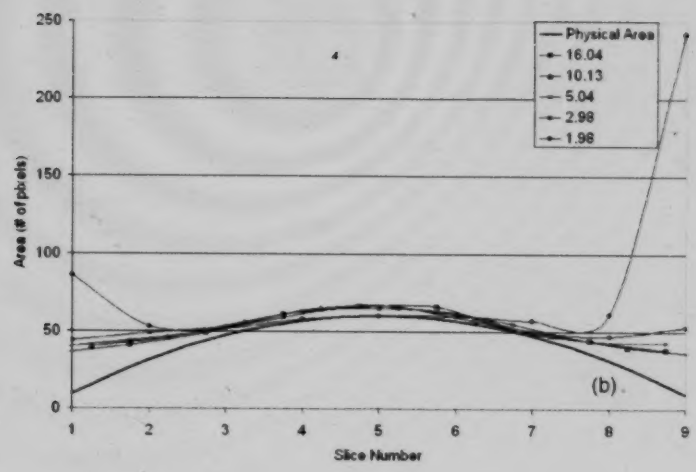

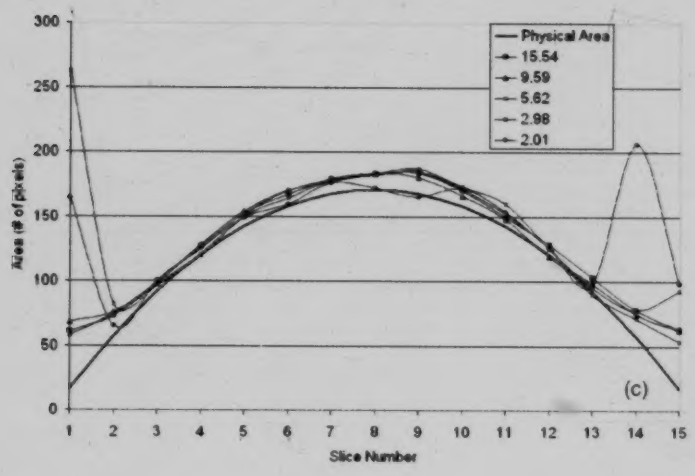

Figure 5.22: Calculated area, using a 28% threshold, versus slice number for the (a) small, (b) medium, and (c) large spheres.

		Single Threshold	
Sphere Size	Ratio	Percentage Discrepancy	Absolute Volume (cm^3)
Large	15.54	14.1	15.1
	9.59	13.4	14.4
	5.62	11.5	12.4
	2.98	28.2	30.3
	2.01	26.8	28.8
Medium	16.04	29.4	6.6
	10.13	30.0	6.7
	5.04	33.1	7.4
	2.98	38.7	8.7
	1.98	108.1	24.2
Small	14.75	37.3	2.1
	9.77	47.3	2.9
	5.00	57.6	3.6
	3.02	62.7	3.9
	2.00	88.4	5.5

Table 5.2: Summary of the percentage differences between the physical volume and the single threshold volume for the three spheres, and the absolute volume difference for the different target to background activity concentration ratios.

The effect of the presence of a large confounding spherical volume on the thresholding of a small spherical target centered in the phantom was investigated. The choice of small target volume with a large, hot, confounding volume was chosen as a limiting case, as the effect of the confounding volume is largest with this combination. **Figure 5.23** shows the ideal threshold versus the physical area for the small single sphere alone and also in the presence of the large confounding volume at a two to one target to background activity concentration ratio. The two lines are very close to one another; however not all the points agree

within experimental error (obtained by taking the standard deviation of the two data points at each physical area). The difference between the points is around 2% and is most likely due to setup variability. Therefore, in concordance with the results observed with cylinders, the effect of the presence of hot, confounding volumes is deemed not to have an appreciable effect, ~2%, on the ideal threshold of spherical target volumes.

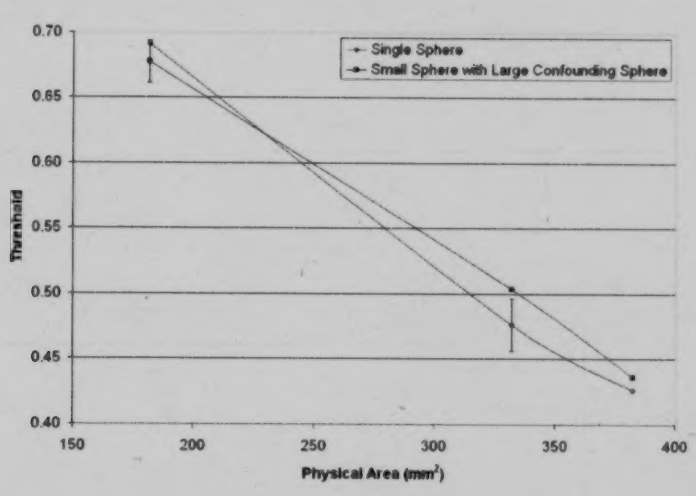

Figure 5.23: Ideal threshold versus the physical area for a small spherical target with a large confounding volume offset from the target by 64mm, for a target to background activity concentration ratio of 2:1.

The effect of position (radial offset) upon the thresholding of spherical target volumes was also investigated. **Figures 5.24** through **5.28** show the effect of offsetting spherical volumes from the centre of the phantom to be quite small. This is shown by comparing the ideal threshold versus physical area for the three offset positions, 0mm, 32mm and 64mm. The majority of data points at different radial positions (for the same target to background activity concentration ratio) agree within experimental error and suggests that the few instances of deviations greater than experimental error arise due to other undetermined causes. These results indicate that the effect of position within the scan plane may, to a good approximation, be safely ignored.

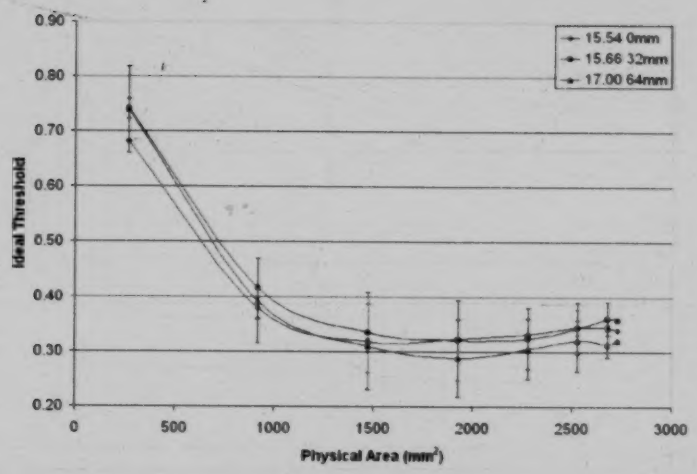

Figure 5.24: Ideal threshold versus physical area for the large sphere at three radial offsets, 0mm, 32mm and 64mm, for a target to background activity concentration ratio of approximately 15:1.

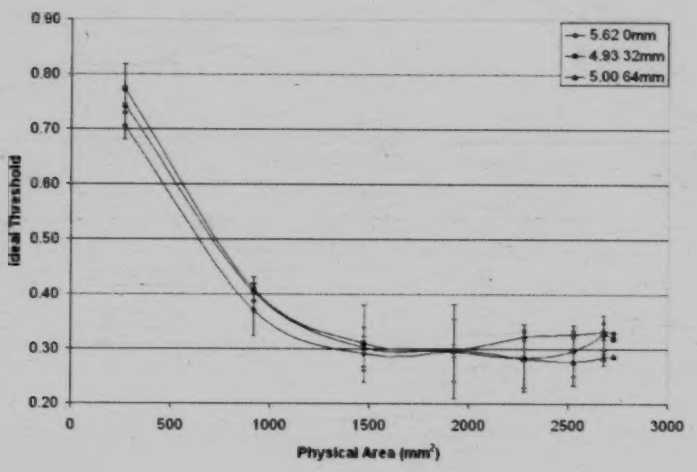

Figure 5.25: Ideal threshold versus physical area for the large sphere at three radial offsets, 0mm, 32mm and 64mm, for a target to background activity concentration ratio of approximately 5:1.

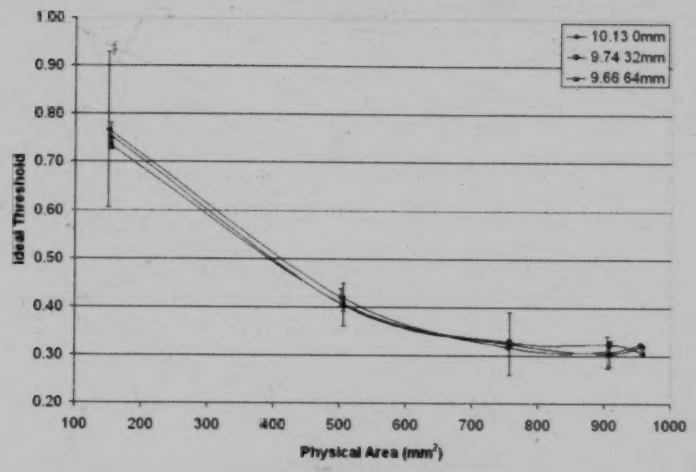

Figure 5.26: Ideal threshold versus physical area for the medium sphere at three radial offsets, 0mm, 32mm and 64mm, for a target to background activity concentration ratio of approximately 10:1.

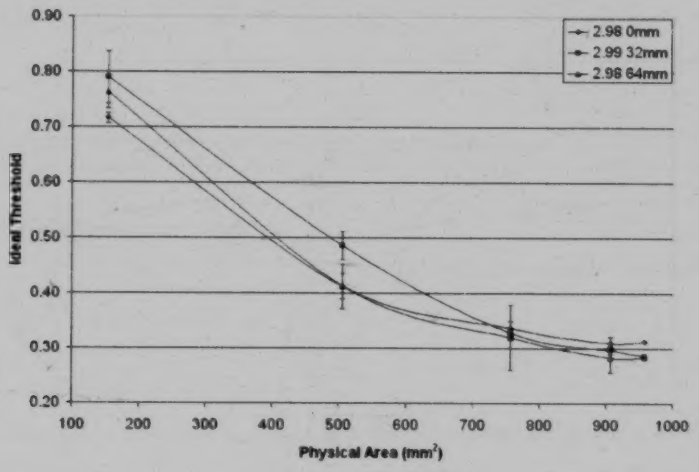

Figure 5.27: Ideal threshold versus physical area for the medium sphere at three radial offsets, 0mm, 32mm and 64mm, for a target to background activity concentration ratio of approximately 3:1.

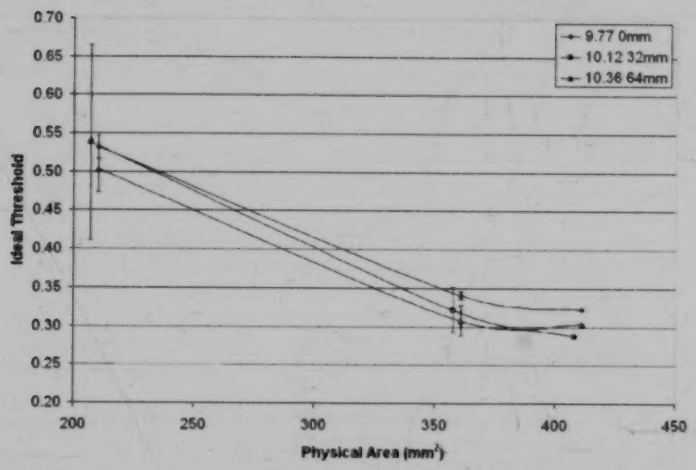

Figure 5.28: Ideal threshold versus physical area for the small sphere at three radial offsets, 0mm, 32mm and 64mm, for a target to background activity concentration ratio of approximately 10:1.

5.3 Sobel

5.3.1 Cylinders

Experimental diameters obtained using the Sobel edge detection method are shown in **Figures 5.29(a-c)** as a function of target to background activity concentration ratio. Also indicated in each of these figures is the true physical diameter of each cylinder. Experimental results obtained with the Sobel technique yield a decidedly poor representation of physical reality as can be seen in **Figures 5.29 (a-c)** for the large, medium and small cylinder. Agreement within experimental error with true physical diameter occurs for neither the small nor large cylinders at any target to background activity concentration ratio. All measured diameters exceed their true size for the small cylinder while the opposite is true for the large cylinder. Only slightly better results are obtained with the medium cylinder where two target to background activity concentration ratios (10.0 and 14.1) yield agreement within experimental error between measurement and reality. The remaining two measurements of diameter lie below their actual values for this cylinder.

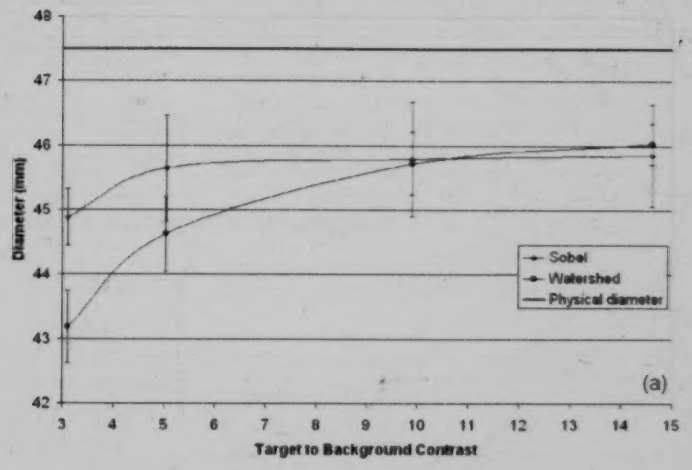
48
47
46
45
44
43
42
Diameter (mm)
3 4 5 6 7 8 9 10 11 12 13 14 15
Target to Background Contrast
Sobel
Watershed
Physical diameter
(a)

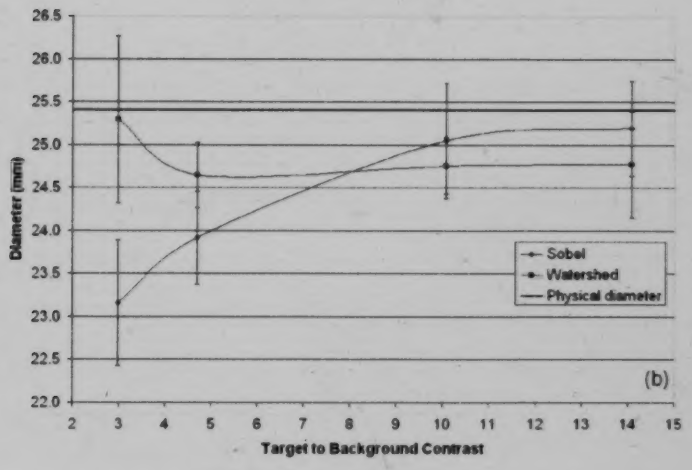
26.5
26.0
25.5
25.0
24.5
24.0
23.5
23.0
22.5
22.0
Diameter (mm)
2 3 4 5 6 7 8 9 10 11 12 13 14 15
Target to Background Contrast
Sobel
Watershed
Physical diameter
(b)

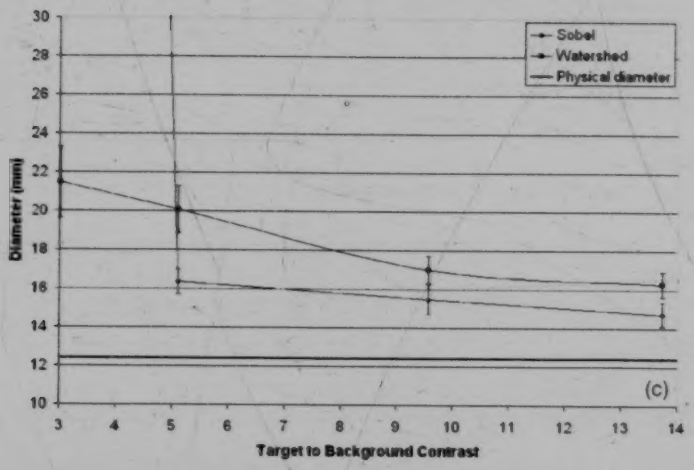

Figure 5.29: Sobel and Watershed experimental diameters versus target to background activity concentration ratio for the (a) large, (b) medium, and (c) small cylinders.

5.3.2 Spheres

Results obtained with the Sobel segmentation technique are presented in **Figures 5.30 (a-c)** where both experimental and weighted mean physical cross sectional areas are plotted as a function of image distance from the center of each sphere. Overall the level of agreement achieved with this method is decidedly poor with the disparity between measurement and reality increasing in the majority of cases as the target to background activity concentration ratio decreases as shown in **Figures 5.29 (a-c)**. Most delineated cross sections are seen to fall short of their actual size with the magnitude of the percentage deviation between these two values generally, but not exclusively, increasing for slice locations further displaced from the center of the spheres. At the lowest target to background activity concentration ratios (~2:1) this technique utterly fails in its application to the medium and large spheres. Cross sectional areas of between 300% and 10,500% their true values are indicated near the periphery of the large sphere for the two lowest target to background activity concentration ratios examined and are well off the plot scale of **Figure 5.30a**. The best agreement between the Sobel derived cross sectional areas and their actual physical values occur for the large sphere at target to background activity concentration levels of 5.6 and higher. Here, however, the

mean absolute percentage differences between measured and true cross sectional area are 11.0%, 6.8% and 6.5% for target to background activity concentration ratios of 5.6, 9.6 and 15.5 respectively.

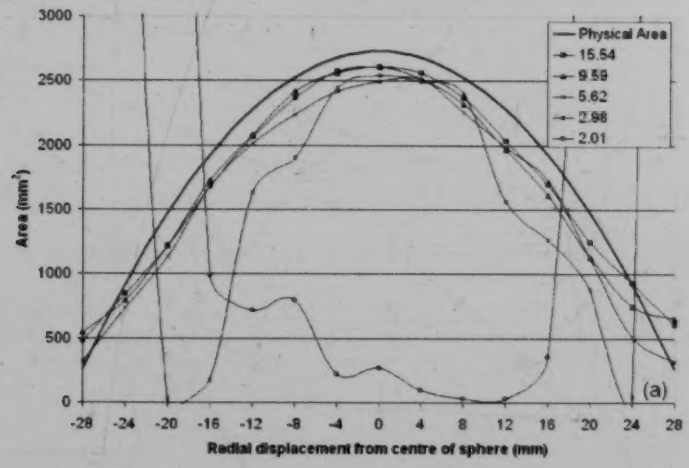

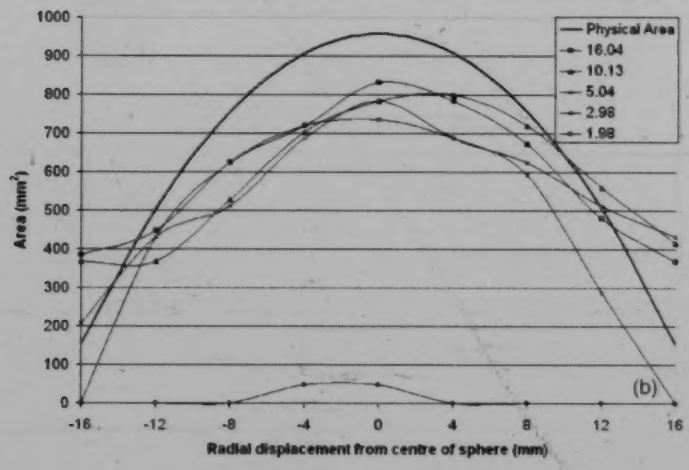

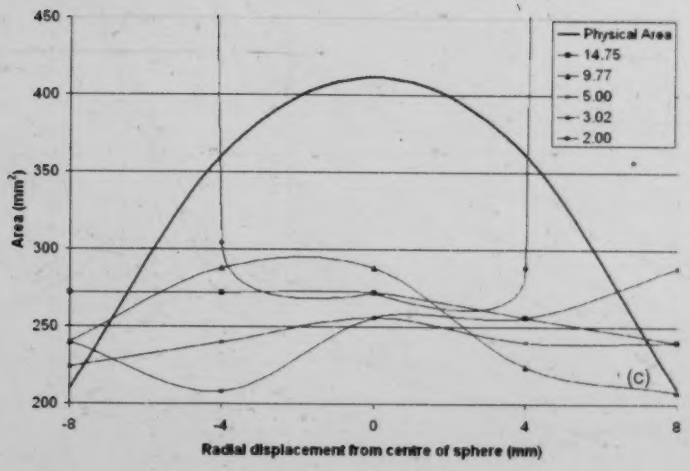

Figure 5.30: Sobel areas versus radial displacement from the centre of the sphere for multiple target to background activity concentration ratios for the (a) large, (b) medium, and (c) small sphere.

5.4 Watershed

5.4.1 Cylinders

Experimentally derived watershed diameters are shown in Figures **5.29(a-c)** as a function of target to background activity concentration ratio. Also indicated in each of these figures is the true physical diameter of each cylinder. Results obtained with the watershed technique prove equally disappointing as the Sobel results as once again no agreement between experiment and reality is achieved for either of the large or small cylinders, see **Figures 5.29(a-c)**. As with the Sobel technique, measured values are too small for the large cylinder and too large for the small cylinder. The medium cylinder results reveal two target to background activity concentration ratios at which measurement agrees with physical reality, but one these does so only at the very limit of experimental error. As with the large cylinder, all measurements of the medium cylinder yield diameters which lie below their physical value.

5.4.2 Spheres

Results obtained with the watershed segmentation technique are presented in **Figures 5.31(a-c)** where both experimental and true physical cross sectional areas are plotted as a function of image distance from the center of each sphere. A similar trend to that produced by the Sobel method is observed for the large and medium spheres where the majority of measured cross sections are less than their true value, see **Figures 5.31(a-c)**. The greatest consistency between the watershed derived cross sectional areas and their actual physical value occurs for the large sphere for target to background activity concentration levels of 9.6 and higher. Here the mean absolute percentage differences between watershed cross sections and their true values are 1.5% and 5.1% for target to background activity concentration ratios of 9.6 and 15.5 respectively. Watershed results obtained with the lowest target to background activity concentration ratio (2.0) for the large sphere are opposite that produced by the Sobel technique. Here the watershed cross sections at image locations nearer the center of the sphere are unrealistically large, ranging from 200% to 10,000% their true size and are well off the plot scale of **Figure 5.31a**. For the small sphere the watershed method yields decidedly deplorable results with no discernable trend with respect to target to background activity concentration ratio.

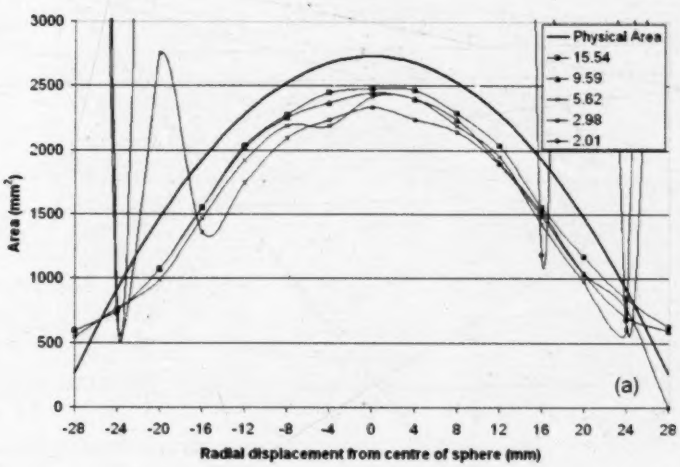

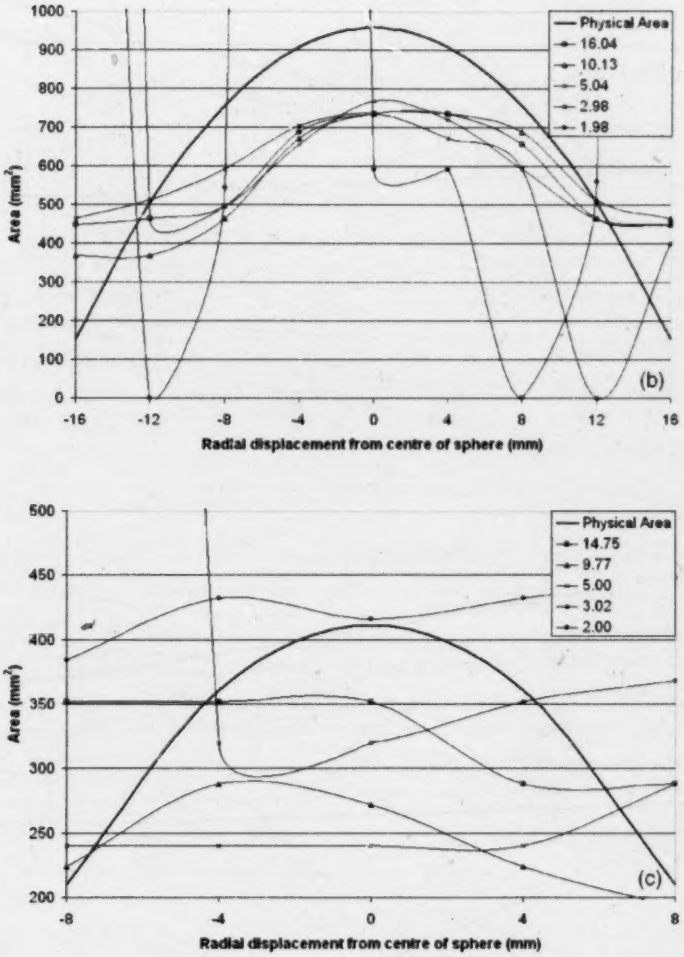

Figure 5.31: Watershed areas versus radial displacement from the centre of the sphere for multiple target to background activity concentration ratios for the (a) large, (b) medium, and (c) small sphere.

5.5 Conclusion

The need for accurate geometric delineation of tumor volumes is essential if PET is to assume a significant quantitative role in both the clinical diagnosis and radiotherapy management of cancer. Of the three segmentation techniques examined here, only the threshold method proved capable of faithfully reproducing cross sections of the simple geometric objects examined. Failure of the Sobel and watershed segmentation schemes, despite being more mathematically robust, arises due to presumptions inherent to

these two approaches. The Sobel method, for example, assumes that the boundary between a target and its surrounding background may be identified by the maximum gradient in the image intensity between these two objects. Inherent to this line of reasoning is the existence of a sharp physical discontinuity between object and background, which was indeed achieved with the experimental setup used here. Substantive partial volume effects inherent to PET images, however, act to blur even the sharpest of physical discontinuities, and, as such, pose a serious impediment to accurate quantitative segmentation using this and other such edge detection methods. Inability of the Sobel technique to yield correct cross sectional areas under these idealized conditions indicates that even poorer results are to be expected in conjunction with real clinical data in which the physical boundaries between tumor and surrounding uninvolved tissues may be less abrupt. The region based watershed technique also proves susceptible to the unique properties of PET images and yields in some cases, as evidenced by the results obtained with the small sphere, an even greater degree of disparity with physical reality.

Thresholding provides a reasonably simple approach to segmentation which can provide accurate delineation of PET target volumes. Threshold levels required to yield accurate delineation of the physical extent of activated volumes are found to be a function of the activity concentration ratio between target and background, target cross section size and radial target position relative to the center of the image plane. Of these three, target cross section size exhibits the largest influence on ideal threshold levels while the dependence on radial target position is minimal. The problematic dependence of threshold level upon target size presents the greatest difficulty associated with this segmentation approach. Examination of the results obtained with cylinders reveals that correct threshold values are also slice position specific but without an identifiable trend. The apparent random nature of the variations associated with slice position strongly suggests that they are the result of the statistical uncertainty inherent to the quantitative analysis of PET images. For the simple geometries provided by cylindrical volumes, threshold levels required for correct segmentation range from about 30% to 65%. Furthermore, the selection of appropriate threshold level is a function of the manner in which the contrast range is defined. A single applied contrast range, derived from the histogram of a suitably chosen centrally positioned slice will yield markedly different ideal threshold levels as compared to those based on a slice specific contrast range. For the more realistic

geometries provided by spherical volumes, threshold levels ranging from 10% to 42% with the single contrast range method, and from less than 30% to more than 90% with the slice specific contrast range approach are required to yield correct cross sectional reproduction.

It is tempting to seek a single threshold level which may be universally applied over the widest range of input data. Taking this approach, based upon the information provided by the three spherical volumes investigated herein, a threshold level of 28% is indicated for the PET scanner used in this investigation in combination with a slice specific assessment of contrast range. This contrast level yields inclusion of the minimum amount of surrounding background volume subject to the constraint that no target cross section over the range presented by these volumes is under represented. Threshold levels of a lesser value will encompass increased amounts of surrounding non-target volume within segmentation boundaries. Use of this particular threshold level results in the inclusion of surrounding non-target volumes ranging from 13% to 108% in excess of the physical extent of these spheres. The absolute volumes associated with these excess inclusions range from 2.1 to 30.3 cm^3. In lung, where typical total surrounding volumes are on the order of 6000 to 7000 cm^3, these amounts of excess may be quite acceptable. In other sites, such as the brain, significant incursions into small immediately adjacent structures such as the optic chiasm may result in unacceptable levels of normal tissue complication. The less than satisfying nature of this conclusion is a clear indication of the need for continued work with regard to the use of thresholding for PET target volume delineation if greater delineation accuracies are to be achieved.

6. Iterative Thresholding

6.1 Introduction

In the preceding chapters three distinct methods of contour delineation: thresholding, Sobel edge detection and a marker based watershed approach, were examined with respect to their abilities to correctly identify the cross sections of well defined targets with uniform activity distributions situated in a homogeneous radioactive surrounding background volume. Results obtained with the Sobel and watershed techniques proved disappointing as both of these segmentation methods failed to accurately reproduce target volumes within acceptable limits. In general these methods identify areas that are too small for large regions of interest and too large for small regions of interest. In some cases these two techniques identified cross sections which were in disagreement with true physical values by as much as 10,000%. Furthermore, in a significant number of cases these two methods also failed to identify any useful portion of the target volume even at slice locations near or coincident with maximums in cross sectional area. Data such as this would, at the present time, seem to warrant against continued investigation of these two techniques and further suggests that other similar methodologies might prove equally unsuitable for the volumetric analysis of PET images.

The threshold segmentation method proved the most viable of the three techniques examined. Unfortunately the threshold level required to yield correct cross section delineation proves to be a function of the physical extent of the target. The dependence of required threshold level upon target size would seem to present a dilemma as accurate threshold segmentation requires an existing knowledge of the extent of the volume to be delineated which is, of course, the very quantity one is seeking to determine. This circular reasoning suggests that a solution might be sought through the application of an iterative approach. Let there exist a function g which yields the threshold level τ required to accurately delineate a cross section of area A such that

$$\tau = g(A) \qquad (6.1)$$

Now consider a threshold measurement function ***f*** which operates on an image set **I** to delineate an experimental cross section of area A^{meas} according to

$$A^{meas} = f(\tau) : I \tag{6.2}$$

where τ is the threshold level used for segmentation. Postulating a reasonable first guess, τ_o, for the required threshold level yields an initial estimate A_o^{meas} of target cross section

$$A_o^{meas} = f(\tau_o) : I \tag{6.3}$$

This initial area estimate may then be used to generate a new value for the required threshold level

$$\tau_1 = g\left(A_o^{meas}\right) \tag{6.4}$$

which, in turn, may be used to generate an updated measure of cross sectional area

$$A_1^{meas} = f(\tau_1) : I \tag{6.5}$$

Presuming convergence one proceeds by repetition to generate

$$\tau_n = g\left(A_{n-1}^{meas}\right) \tag{6.6}$$

and

$$A_n^{meas} = f(\tau_n) : I \tag{6.7}$$

Until one arrives at the condition

$$A_n^{meas} - A_{n-1}^{meas} \leq \delta \tag{6.8}$$

where δ is some predetermined end point value at which one considers the measured cross section to have approached sufficiently close to the true value in order for calculation to cease. Proceeding in this manner presumes that convergence may be achieved. This is certainly not guaranteed when working with experimental data. Even when convergence is achieved there can be no assurance that the result accords with meaningful physical values. Fortunately, in this case, convergence to reasonable values was achieved in most cases, lending credence to this approach.

Examination of the data presented in **Figures 5.19(a-c)** reveals that the functional dependence of slice specific contrast threshold segmentation upon target to background activity concentration ratio is relatively small in comparison to the influence of cross sectional area for the medium and large spherical volumes. A

greater variation in delineated area with respect to activity concentration ratio is seen with results obtained with the small sphere but threshold level remains the dominant effect. To a first approximation, then, the effect of target to background activity concentration ratio will be ignored in the derivation of the function g(A) which yields required threshold values as a function of cross sectional area. To this end the entire data set from **Figures 5.19(a-c)**, which relate required threshold levels to mean weighted physical area, is plotted in the single graph of **Figure 6.1**. This data is well represented by a piecewise continuous function of the form

$$g(A) = \begin{cases} \tau = a_1 e^{-aA} & \text{for } A < A' \\ \tau = a_2 A + c & \text{for } A \geq A' \end{cases} \qquad \textbf{(6.9)}$$

The relative spread of data points for areas less than 50 pixels prompts the use of two distinct threshold functions $g_1(A)$ and $g_2(A)$. These are

$$g_1(A) = \begin{cases} \tau = 0.9078701 e^{-0.03971028\,A} & \text{for } A < 28 \\ \tau = 0.0002465979 A + 0.2876669 & \text{for } A \geq 28 \end{cases} \qquad \textbf{(6.10)}$$

and

$$g_2(A) = \begin{cases} \tau = 0.8658237 e^{-0.02153858\,A} & \text{for } A < 50 \\ \tau = 0.0002465979 A + 0.2876669 & \text{for } A \geq 50 \end{cases} \qquad \textbf{(6.11)}$$

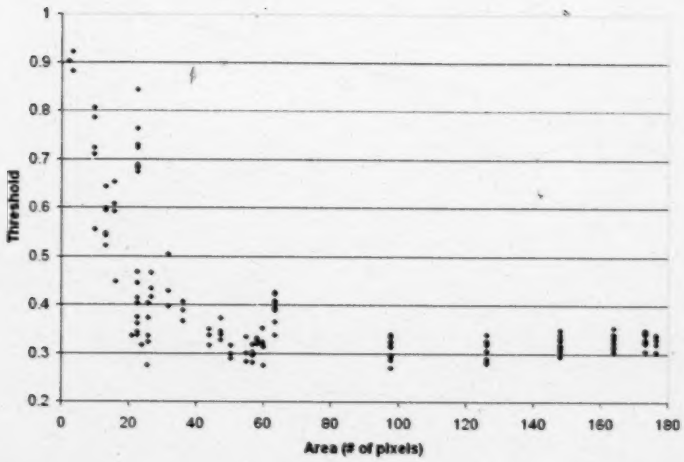

Figure 6.1: Ideal threshold versus physical area for the spherical targets at all target to background activity concentration ratios.

The fit of these two threshold functions to the experimental data is shown in **Figure 6.2**. To determine which of the two functions to use in the iterative thresholding procedure the contrast between the maximum pixel value and the background pixel value is found on each frame. Then the full width at half maximum is determined for the peak that corresponds to the maximum pixel value in the image. If the FWHM is less than 6 frames (24mm) the function shown in **(6.10)** is used, otherwise function **(6.11)** is employed. Once the iterative thresholding function has been determined an initial threshold $\tau_o = 0.4$ is applied to the image to be segmented. The initial threshold value of 0.4 was chosen as it falls in the exponential region of both analytical fits. Other initial τ_o values were examined but no discernable difference was observed in the final result. The iterative process continued through 10 iterations, in most cases the threshold ceased to change ($\delta = 0$) after the first 4 iterations. However, on occasion the process did not converge so a maximum of ten iterations was used to stop the iterative process and the threshold value of the tenth iteration was used.

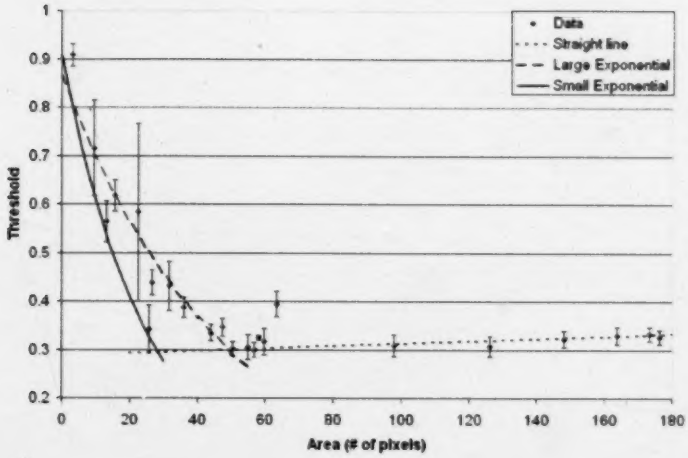

Figure 6.2: Fits to ideal threshold versus area for the spherical targets at all target to background activity concentration ratios.

6.2 Spherical Targets

Unfortunately this approach proved overly simplistic and failed to accurately delineate the volumes of the three spheres. See **Figures 6.3(a-e)** to **6.5(a-e)** for the results of applying iterative thresholding to only the axial data set. While the results for the large sphere are quite accurate this technique clearly fails for the small spheres. Application to the medium size sphere (35 mm diameter), for example, yielded the data shown in **Figure 6.4**. Comparison of the cross sectional areas generated by this iterative approach to the true mean weighted physical area at each slice location reveals reasonable agreement near the center of the sphere but underestimation of cross sections at most locations more distal from the center of this volume. As an inability to identify the full extent of a tumor volume would translate clinically into an increased probability of geometric failure, and hence compromised radio-therapeutic benefit, improvement in segmentation accuracy with this approach is highly desirable.

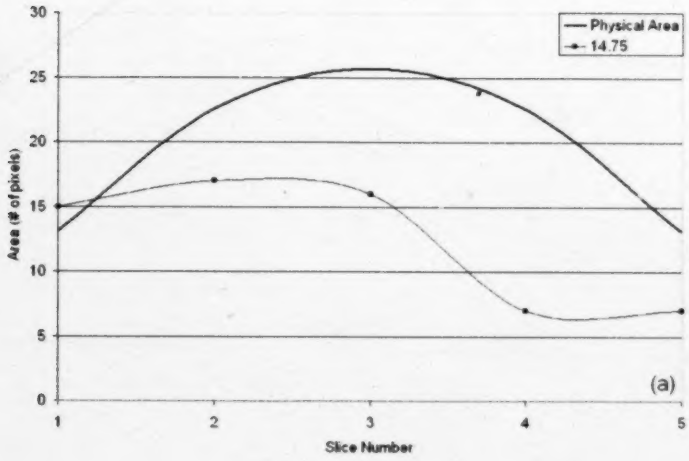
Physical Area
14.75
Area (# of pixels)
Slice Number
(a)

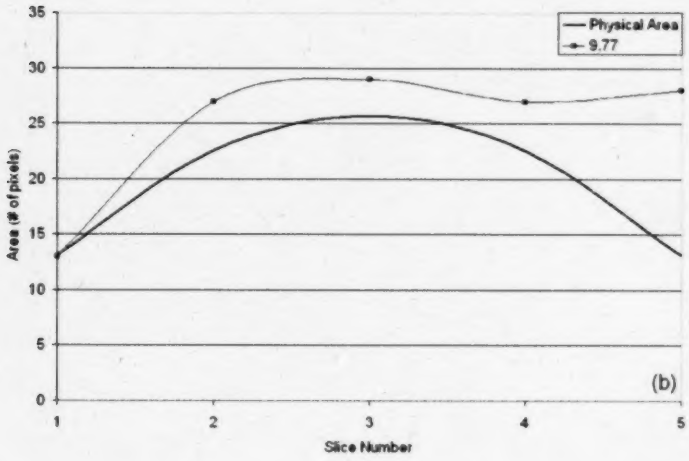
Physical Area
9.77
Area (# of pixels)
Slice Number
(b)

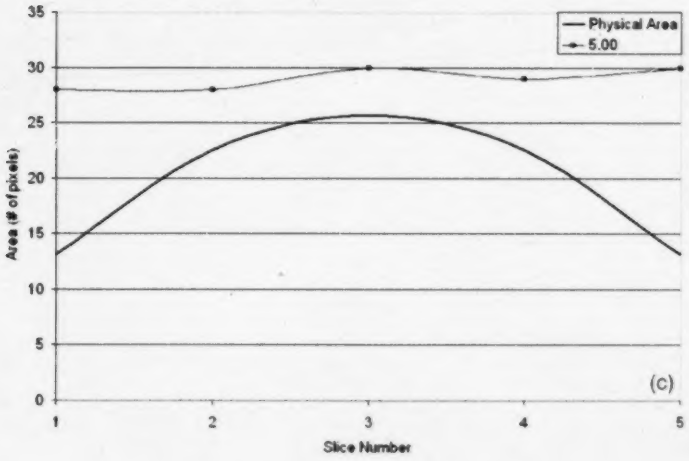
Physical Area
5.00
Area (# of pixels)
Slice Number
(c)

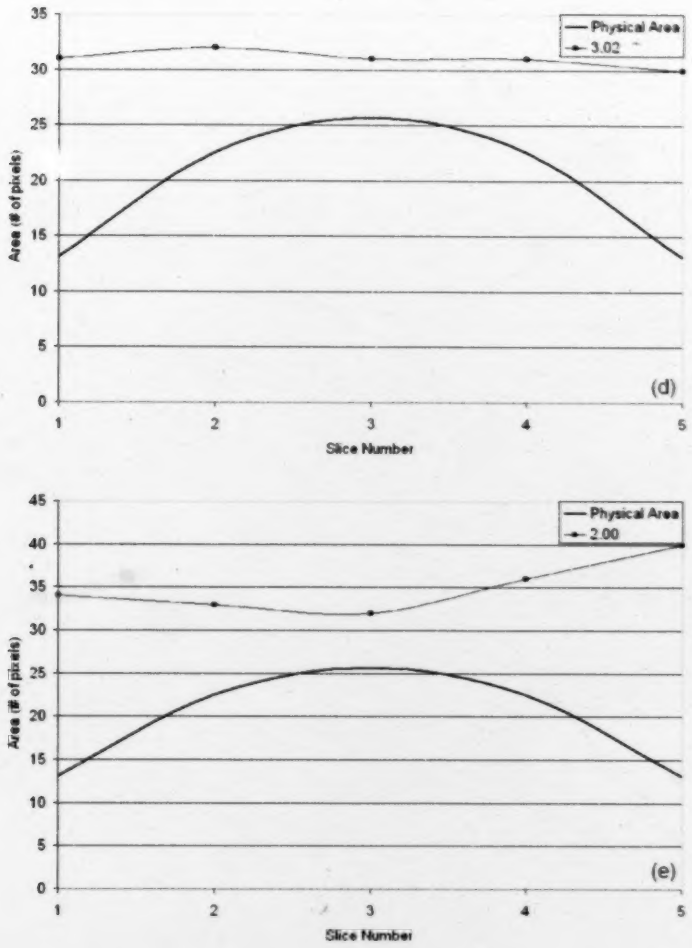

Figure 6.3: Area found using the iterative thresholding technique only on the axial data set for the small sphere at approximately (a) 15, (b) 10, (c) 5, (d) 3, and (e) 2 to one target to background activity concentration ratios versus slice number.

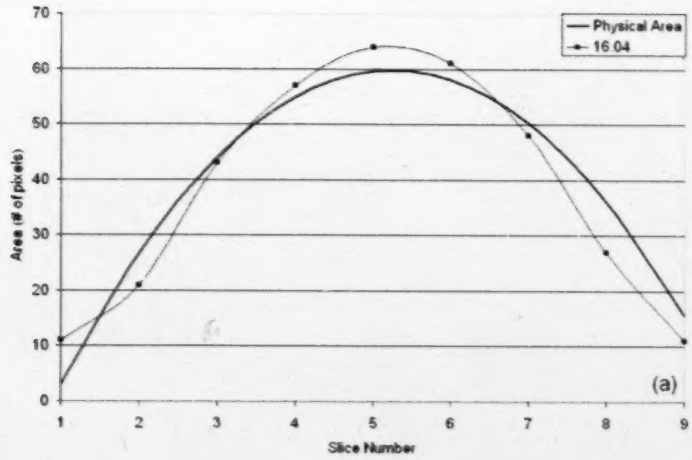
Physical Area
16.04
Area (# of pixels)
Slice Number
(a)

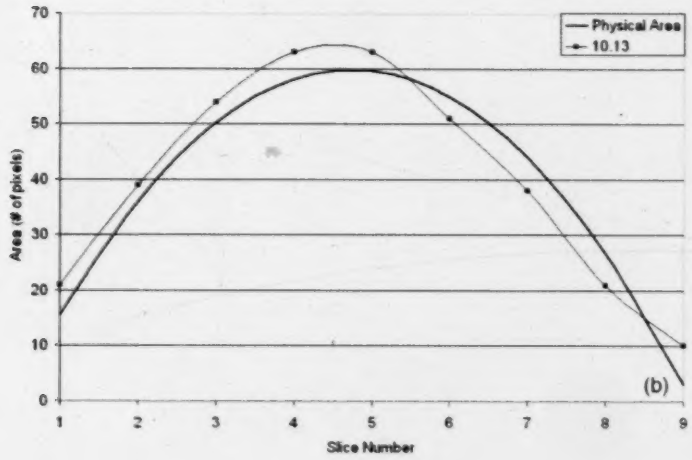
Physical Area
10.13
Area (# of pixels)
Slice Number
(b)

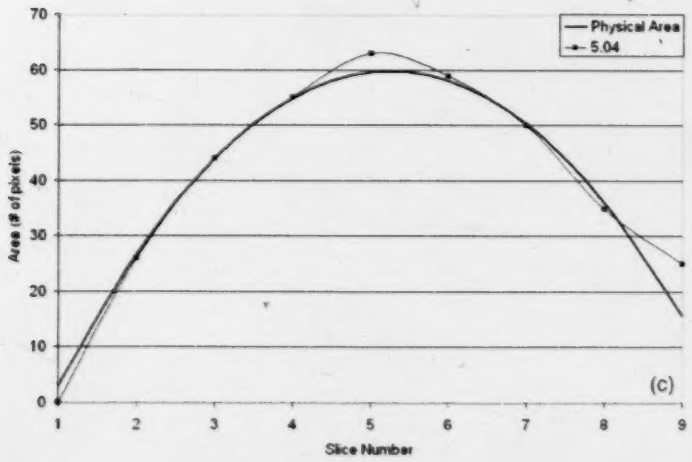
Physical Area
5.04
Area (# of pixels)
Slice Number
(c)

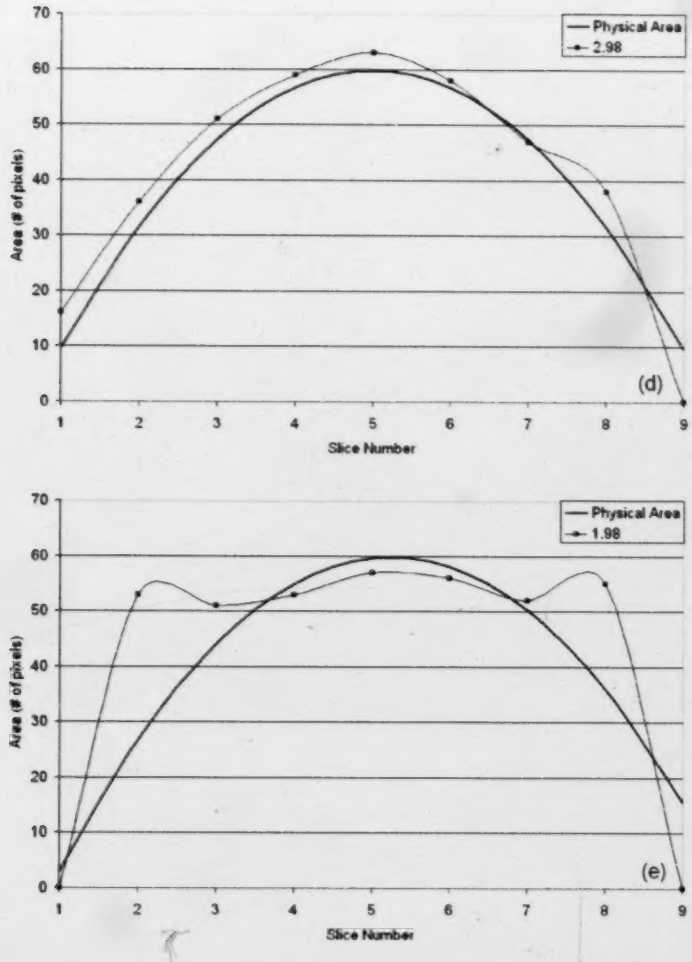

Figure 6.4: Area found using the iterative thresholding technique only on the axial data set for the medium sphere at approximately (a) 15, (b) 10, (c) 5, (d) 3, and (e) 2 to one target to background activity concentration ratios versus slice number.

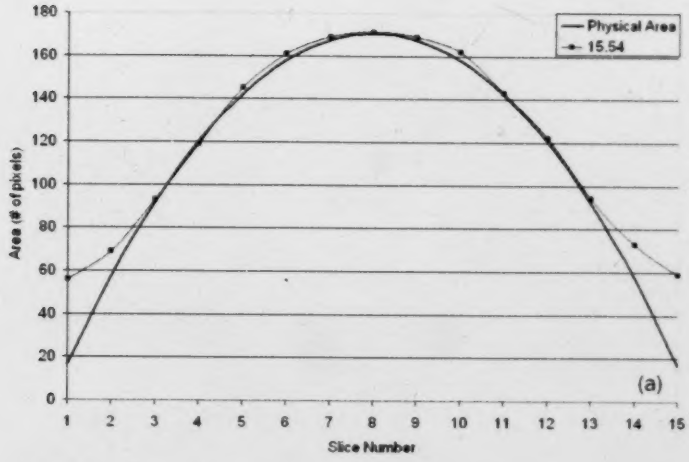
Physical Area
15.54
Area (# of pixels)
Slice Number
(a)

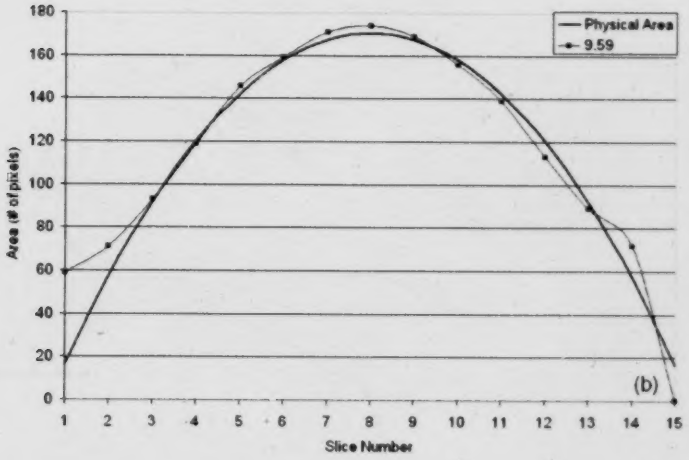
Physical Area
9.59
Area (# of pixels)
Slice Number
(b)

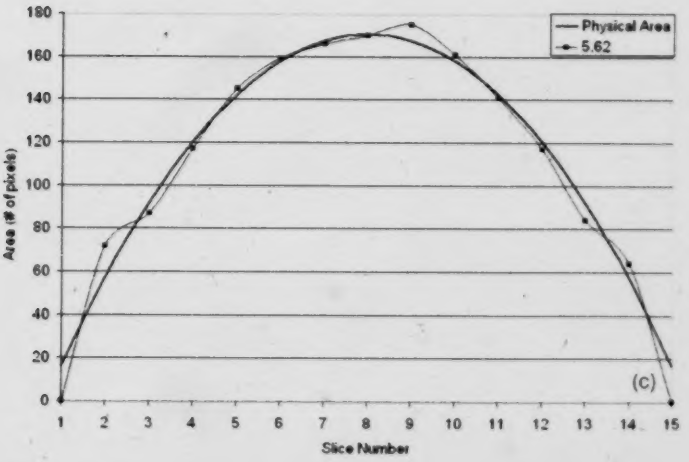
Physical Area
5.62
Area (# of pixels)
Slice Number
(c)

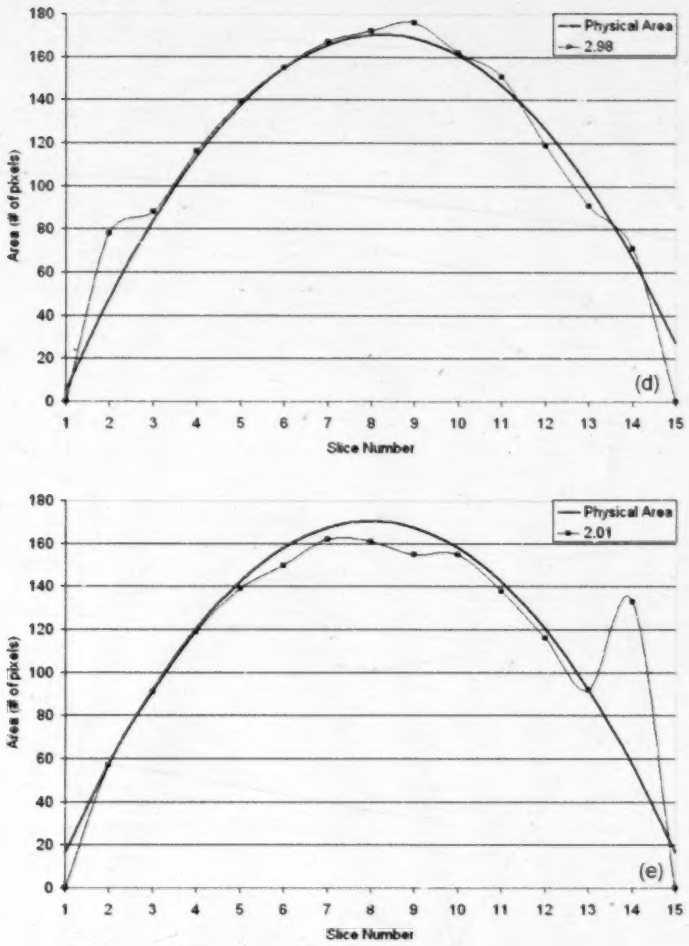

Figure 6.5: Area found using the iterative thresholding technique only on the axial data set for the large sphere at approximately (a) 15, (b) 10, (c) 5, (d) 3, and (e) 2 to one target to background activity concentration ratios versus slice number.

Improvement in the quality of the fit to the tails of the spheres may be achieved by applying the above iterative thresholding approach to each of the axial, coronal and sagittal data sets. After each slice in each of the three cardinal directions is thresholded, a binary image data set is created in which all pixels that are found to be within the target are set to one and all other pixels are set to zero. The corresponding pixels in each data set are then summed, resulting in a new data set with pixel values ranging between zero and three. If this tri-axial thresholding process had performed perfectly, only those pixels belonging to the

object would be found in each of the three directions and the summed image would consist entirely of pixel values equal to three. However, the thresholding process is not perfect so the summed image consists of four possible pixel values, zero through three. Cross sectional areas derived from pixels with a value of one or greater (tri-axial method threshold of one) yield the data shown in **Figures 6.6 (a-e)** through **6.8 (a-e)**. A modest improvement over that achieved with the axial threshold method is realized for the small sphere at high target to background activity concentration ratios (14.75 and 9.77). At the lowest two activity concentration ratios (3.02 and 2.00) the agreement with mean weighted physical cross sectional areas is decidedly poor. At the lowest activity concentration ratio of 2.00 the cross sections derived by the tri-axial method threshold of one exceed their true physical values by more than 700%. For the medium sphere the conformity to physical reality with the tri-axial method threshold of one is poorer than that achieved with the simple axial approach at all activity concentration ratios. At the lowest concentration ratio (1.98) the tri-axial method threshold of once again predicts cross sections which are more than 700% greater than their true physical value. For the largest sphere the simple axial method is seen to yield better conformity to physical reality at all activity concentration ratios than does the tri-axial method threshold of one. Clearly there exists room for improvement with the tri-axial method.

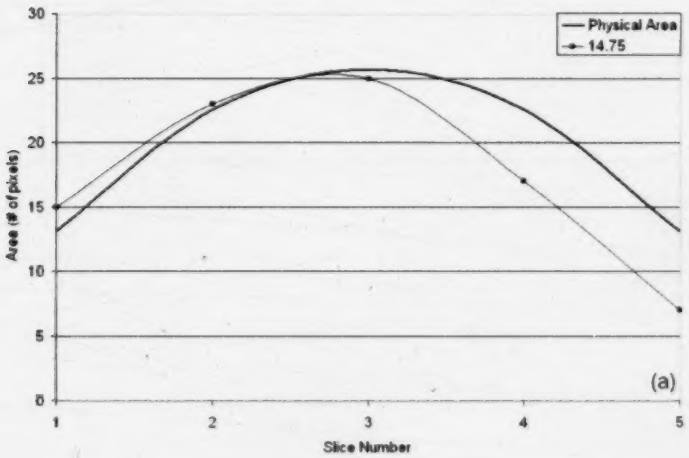

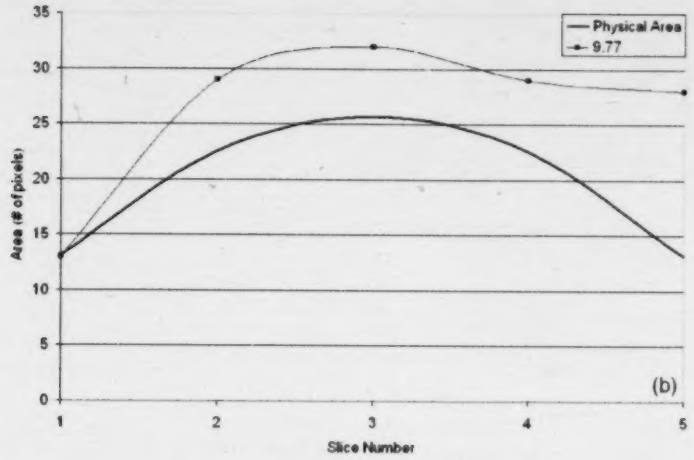
Physical Area
9.77
Area (# of pixels)
Slice Number
(b)

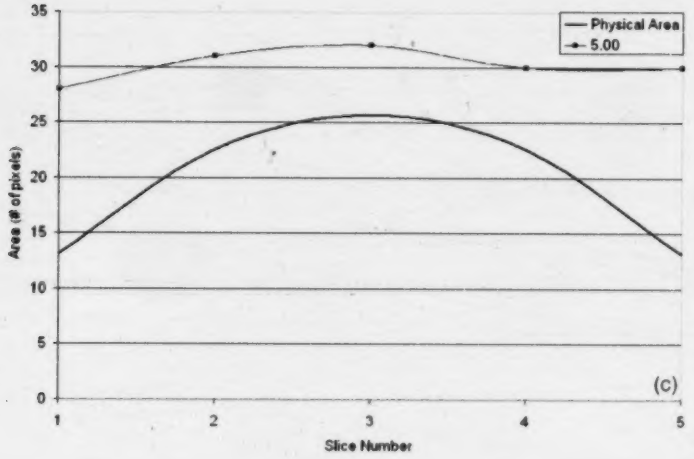
Physical Area
5.00
Area (# of pixels)
Slice Number
(c)

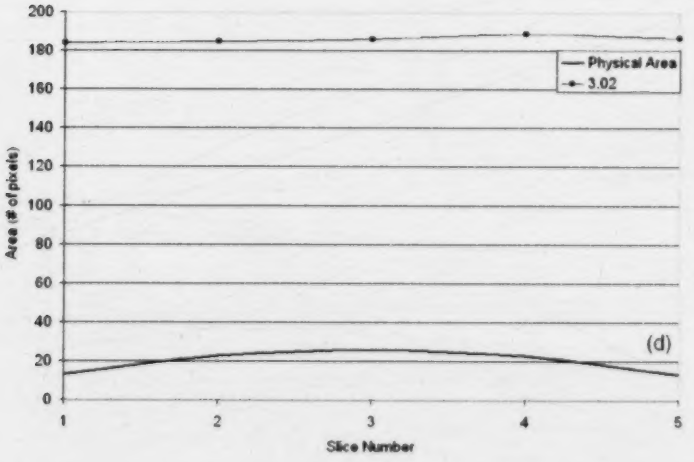
Physical Area
3.02
Area (# of pixels)
Slice Number
(d)

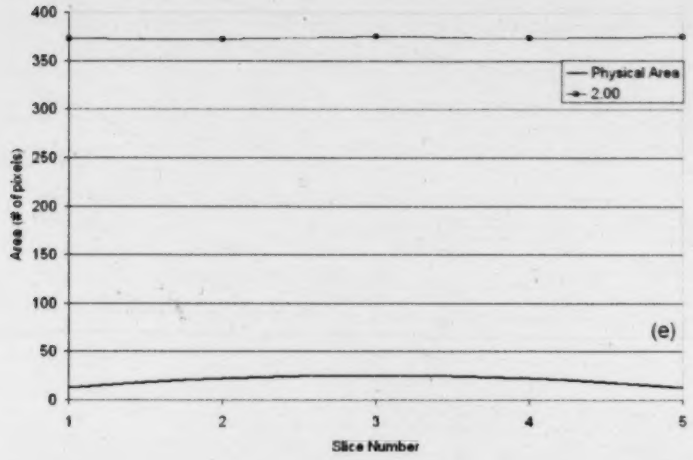

Figure 6.6: Calculated area using the tri-axial iterative thresholding method with a threshold of one for the small sphere for target to background activity concentration ratios of approximately (a) 15, (b) 10, (c) 5, (d) 3, and (e) 2 to one versus slice number.

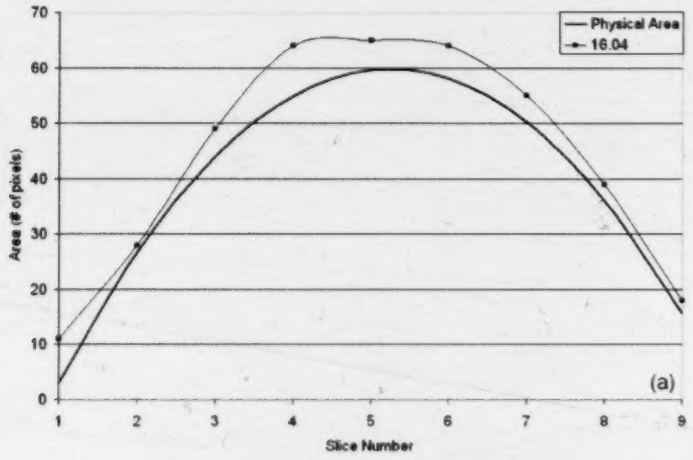

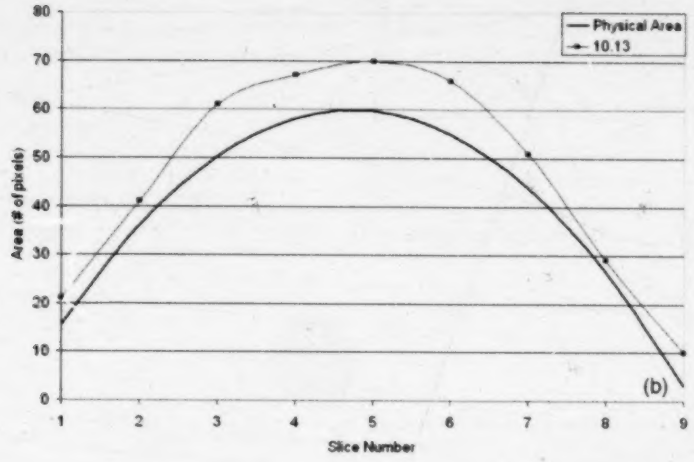
Physical Area
10.13
Area (# of pixels)
Slice Number
(b)

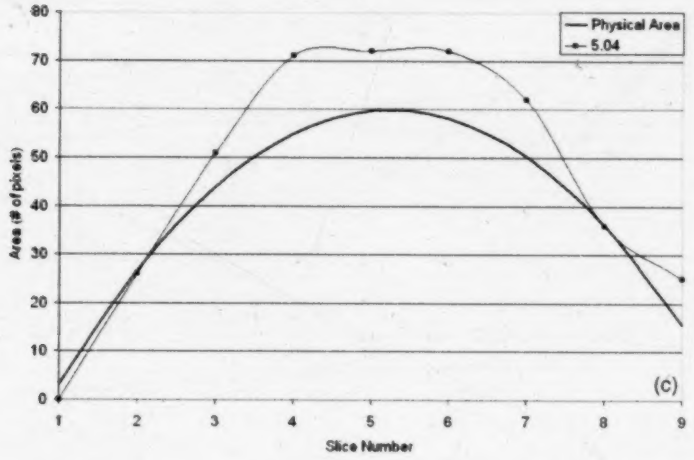
Physical Area
5.04
Area (# of pixels)
Slice Number
(c)

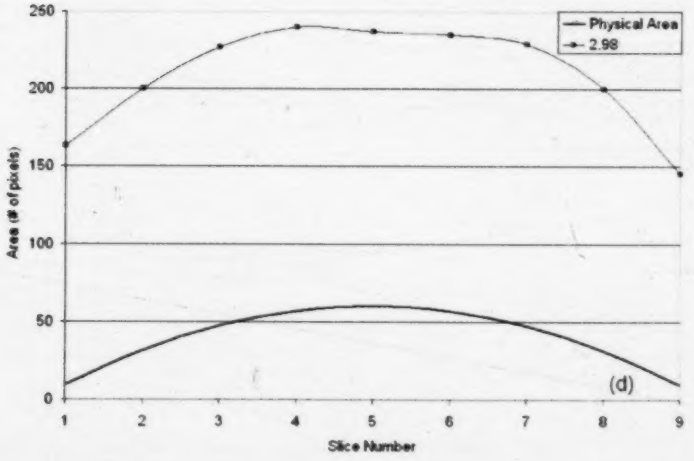
Physical Area
2.98
Area (# of pixels)
Slice Number
(d)

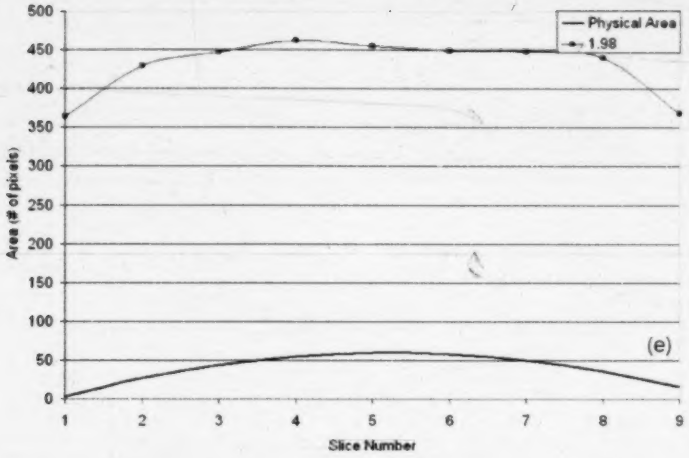

Figure 6.7: Calculated area using the tri-axial iterative thresholding method with a threshold of one for the medium sphere for target to background activity concentration ratios of approximately (a) 15, (b) 10, (c) 5, (d) 3, and (e) 2 to one versus slice number.

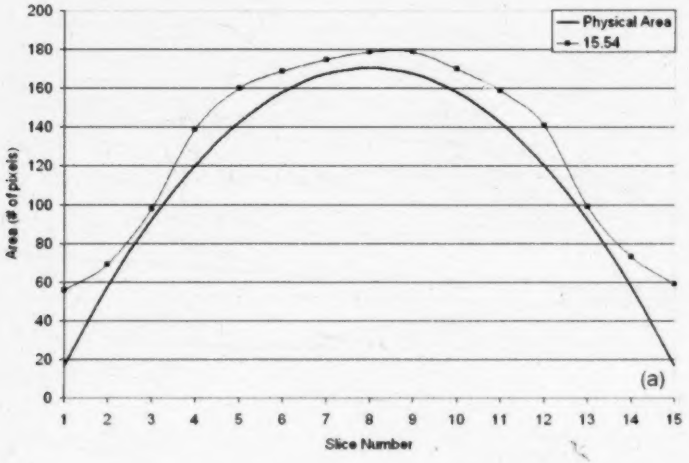

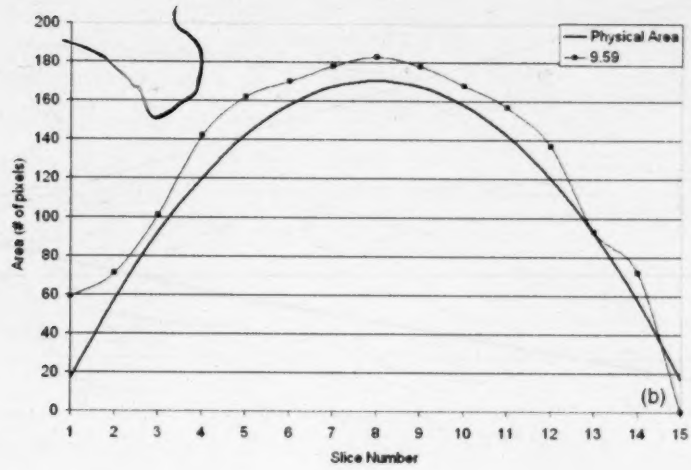
Physical Area
9.59
Area (# of pixels)
Slice Number
(b)

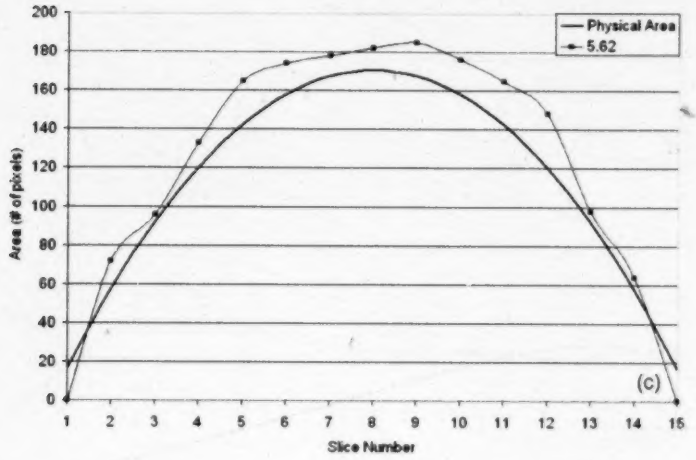
Physical Area
5.62
Area (# of pixels)
Slice Number
(c)

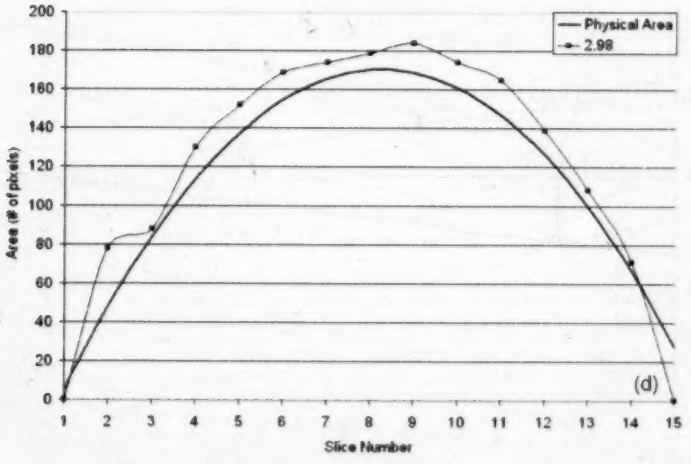
Physical Area
2.98
Area (# of pixels)
Slice Number
(d)

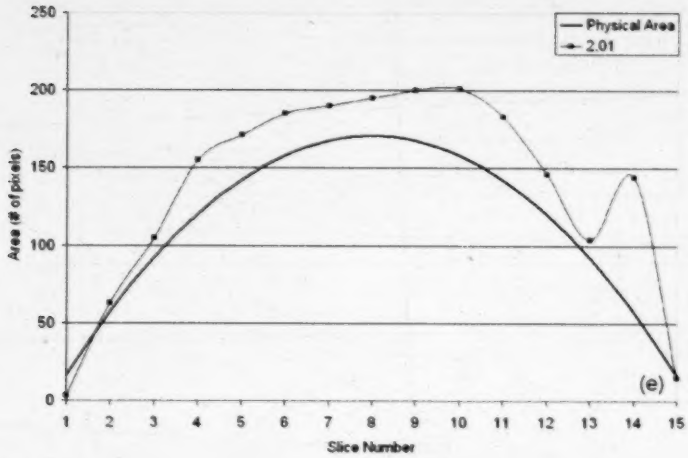

Figure 6.8: Calculated area using the tri-axial iterative thresholding method with a threshold of one for the large sphere for target to background activity concentration ratios of approximately (a) 15, (b) 10, (c) 5, (d) 3, and (e) 2 to one versus slice number.

The tri-axial iterative threshold method using pixel values of two and greater indicate that the pixel in question appears in at least two of the three cardinal data sets, and is thus less likely to be the result of either noise or a failure in the basic iterative process. Cross sectional areas derived from pixels with a value of two or greater (tri-axial method threshold of two) yield the data shown in **Figures 6.9 (a-e)** through **6.11 (a-e)**. Significant improvements in conformity to physical reality are achieved with the tri-axial method threshold of two as compared to the tri-axial method threshold of one for both the medium and large spheres at all activity concentration ratios. For the small sphere the tri-axial method threshold of two is superior to the tri-axial method threshold of one at the lowest two activity concentration ratios. At the highest activity concentration ratio the tri-axial method threshold of two is inferior to the tri-axial method threshold of one. The tri-axial method threshold of two decidedly out performs the simple axial threshold approach for the small sphere at the lowest two activity concentration ratios. For both the medium and large spheres it is difficult to decide which technique better accords with physical reality.

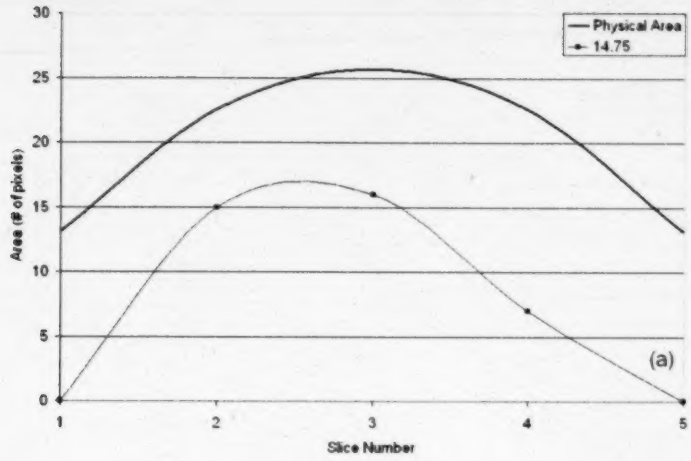
Physical Area
14.75
Area (# of pixels)
Slice Number
(a)

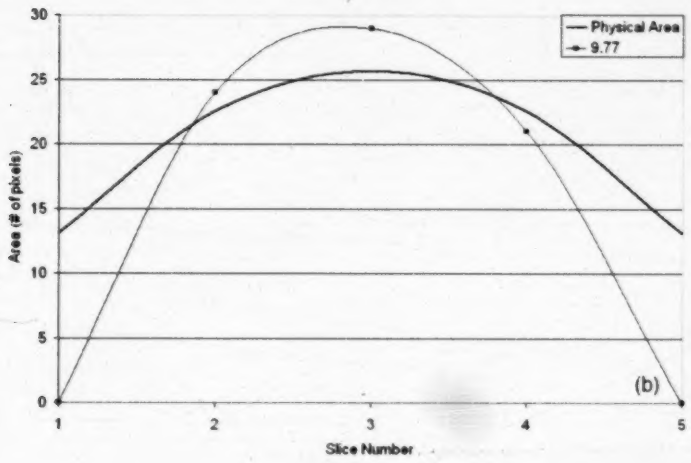
Physical Area
9.77
Area (# of pixels)
Slice Number
(b)

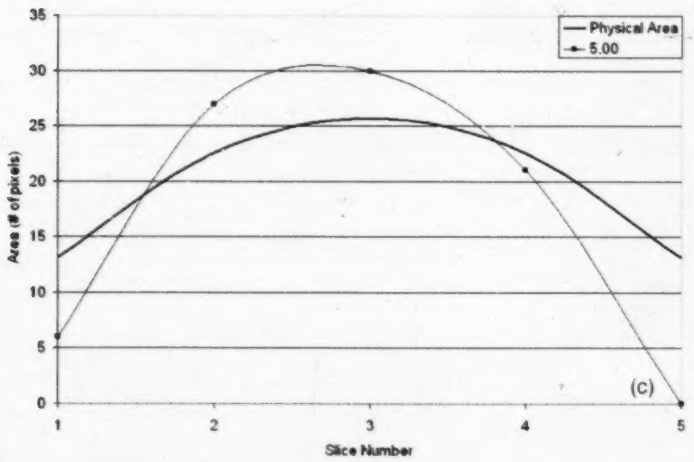
Physical Area
5.00
Area (# of pixels)
Slice Number
(c)

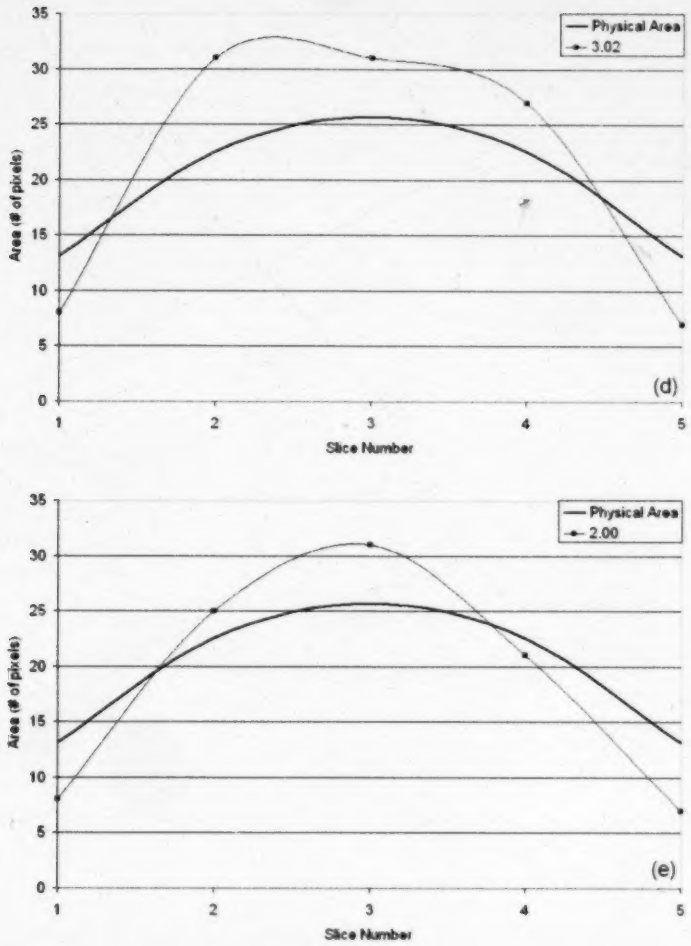

Figure 6.9: Calculated area using the tri-axial iterative thresholding method with a threshold of two for the small sphere for target to background activity concentration ratios of approximately (a) 15, (b) 10, (c) 5, (d) 3, and (e) 2 to one versus slice number.

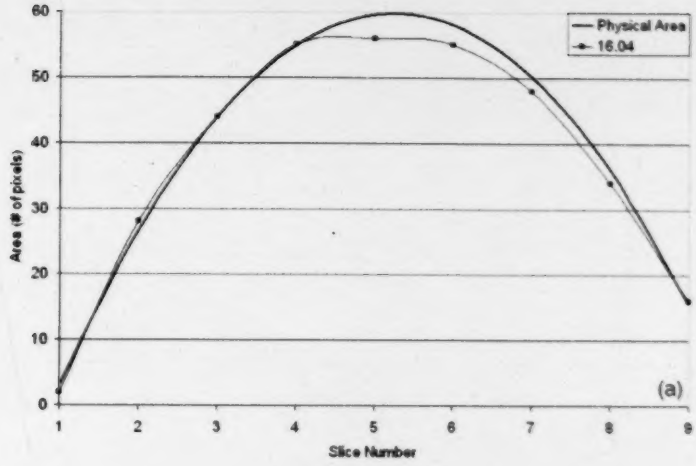
Physical Area
16.04
Area (# of pixels)
Slice Number
(a)

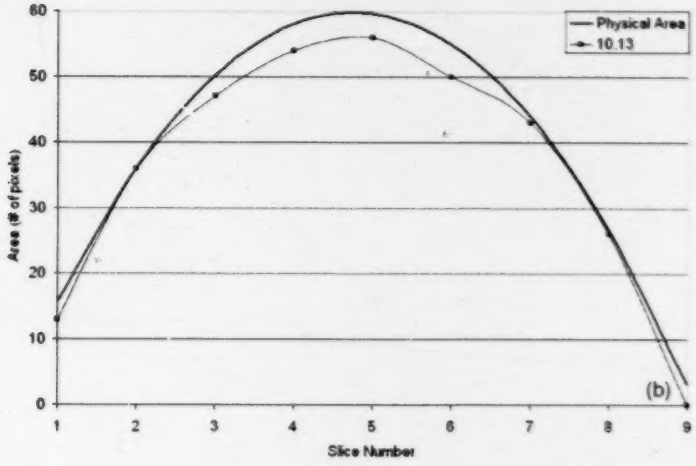
Physical Area
10.13
Area (# of pixels)
Slice Number
(b)

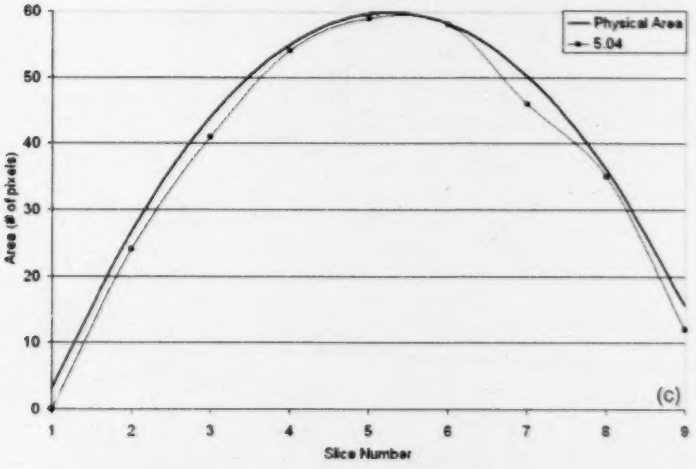
Physical Area
5.04
Area (# of pixels)
Slice Number
(c)

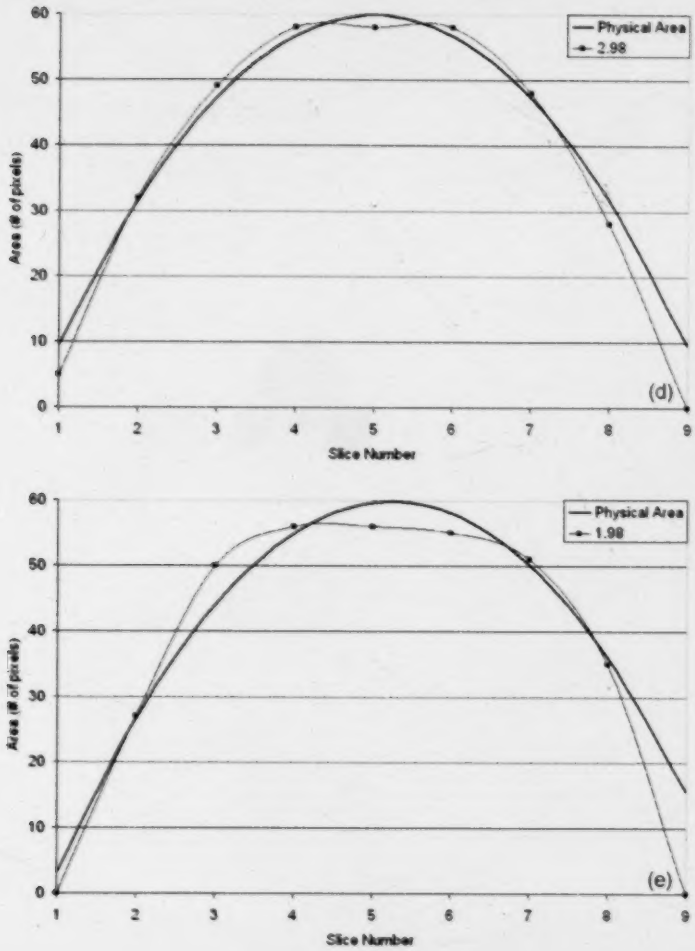

Figure 6.10: Calculated area using the tri-axial iterative thresholding method with a threshold of two for the medium sphere for target to background activity concentration ratios of approximately (a) 15, (b) 10, (c) 5, (d) 3, and (e) 2 to one versus slice number.

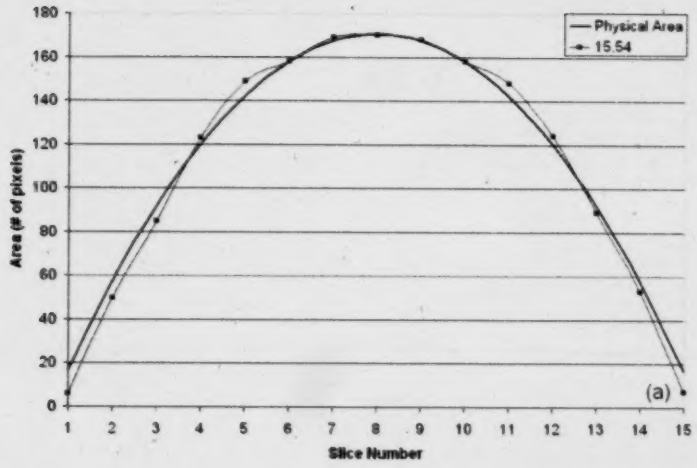
Physical Area
15.54
Area (# of pixels)
Slice Number
(a)

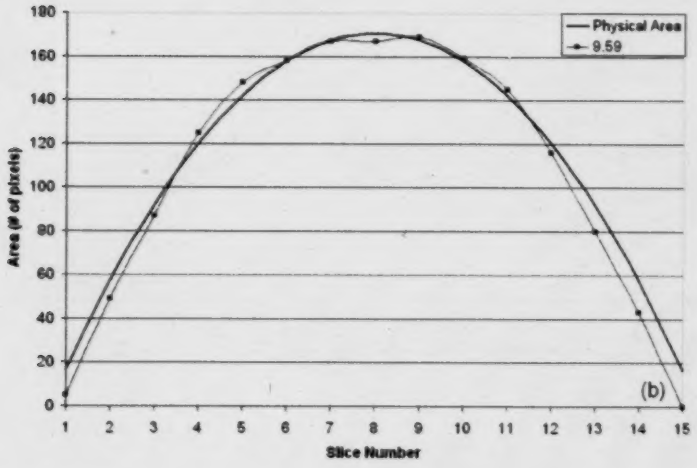
Physical Area
9.59
Area (# of pixels)
Slice Number
(b)

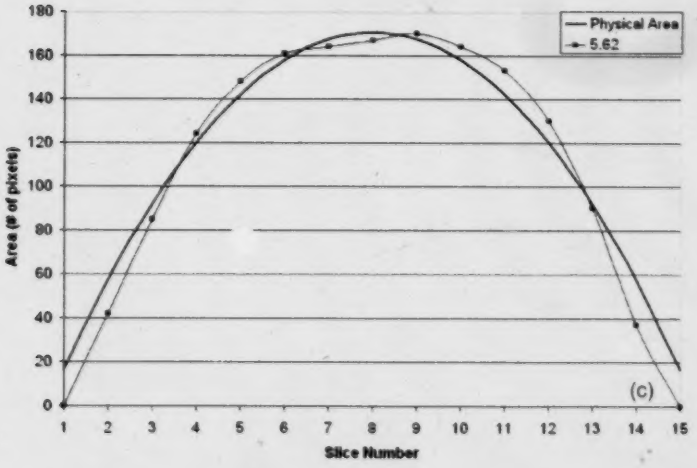
Physical Area
5.62
Area (# of pixels)
Slice Number
(c)

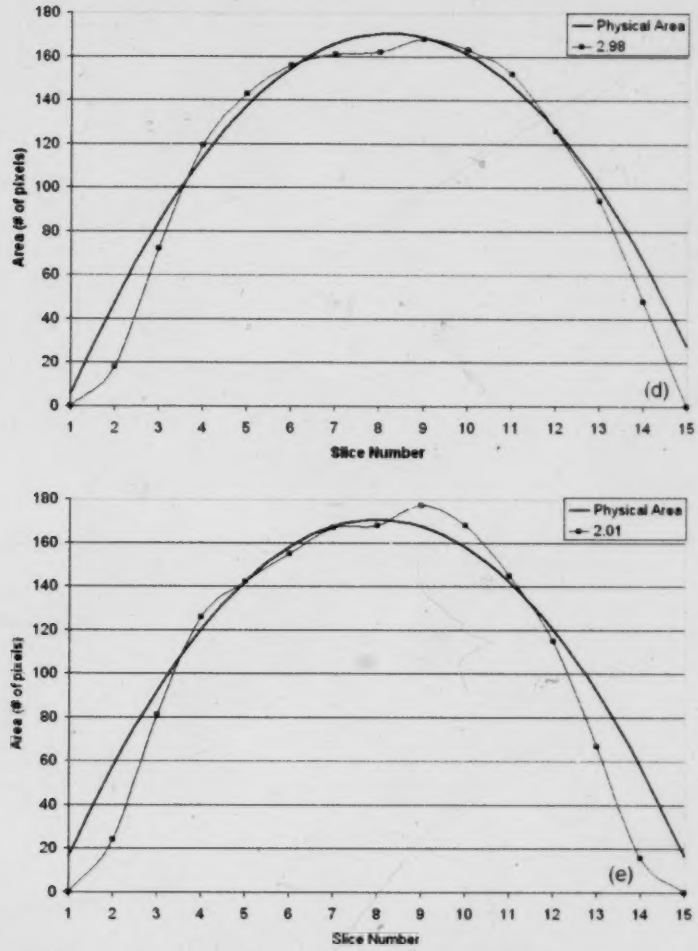

Figure 6.11: Calculated area using the tri-axial iterative thresholding method with a threshold of two for the large sphere for target to background activity concentration ratios of approximately (a) 15, (b) 10, (c) 5, (d) 3, and (e) 2 to one versus slice number.

The percentage difference between measured and actual volumes are shown in **Table 6.1** for the application of a single 28% threshold, the application of the iterative threshold in the axial direction and the tri-axial thresholding with a threshold value of two. Also shown is the absolute difference (cm^3) between measured and true volumes. As can be seen from **Table 6.1** axial thresholding provides more accurate results than the tri-axial iterative threshold in about half of the cases. However the tri-axial iterative threshold provides better results for the smaller targets at lower target to background activity concentration

ratios. With the exception of the small sphere at a target to background activity concentration ratio of 14.75, the iterative threshold methods produce significant improvements in the ability to determine overall target volume as compared to the use of a single threshold value. This is achieved at the cost of the underestimation of a number of individual cross sectional areas. The addition of a margin must always be contemplated in conjunction with use of these iterative threshold techniques if one wishes to ensure that no cross sections are underestimated. The largest deviation between measured (axial and tri-axial iterative methods) and actual cross section contours observed throughout was ≤ 10 mm. The addition of a 10 mm margin to all measured contours would thus be prudent to ensure that no cross sections are underestimated.

		Single Threshold (28%)		Axial Iterative Threshold		Tri-axial Iterative with a Threshold of two	
Sphere Size	Ratio	Percentage Discrepancy	Absolute Volume (cm^3)	Percentage Discrepancy	Absolute Volume (cm^3)	Percentage Discrepancy	Absolute Volume (cm^3)
Large	15.54	14.1	15.1	7.5	8.0	1.3	1.4
	9.59	13.4	14.4	3.0	3.2	3.7	3.9
	5.62	11.5	12.4	1.3	1.4	2.7	2.8
	2.98	28.2	30.3	0.5	0.5	5.6	6.0
	2.01	26.8	28.8	0.7	0.7	7.7	8.2
Medium	16.04	29.4	6.6	1.6	0.4	3.0	0.7
	10.13	30.0	6.7	3.3	0.7	6.8	1.5
	5.04	33.1	7.4	2.4	0.5	5.6	1.3
	2.98	38.7	8.7	5.0	1.1	4.1	0.9
	1.98	108.1	24.2	8.2	1.8	5.3	1.2
Small	14.75	37.3	2.1	36.2	2.2	60.9	3.8
	9.77	47.3	2.9	27.7	1.7	23.8	1.5
	5.00	57.6	3.6	49.3	3.1	13.5	0.8
	3.02	62.7	3.9	59.6	3.7	7.1	0.4
	2.00	88.4	5.5	80.2	5.0	5.3	0.3

Table 6.1: Summary of the percentage difference (measured – true) between the physical volume and the calculated volume for the application of a single threshold, the iterative threshold for only the axial data set, and the tri-axial iterative threshold to the spherical data, also shown is the absolute difference in volume.

The medium sphere was re-imaged in order to provide a data set not used in the generation of **Equations 6.10** and **6.11**. **Figure 6.12** shows the results of the tri-axial method threshold of two iterative thresholding process as applied to this new data set for the medium sphere centered in the phantom. This figure shows an overestimation of the target size on the central slice however the small ends of the spheres are properly fit. The overestimation on the central slices is on the order of ten percent.

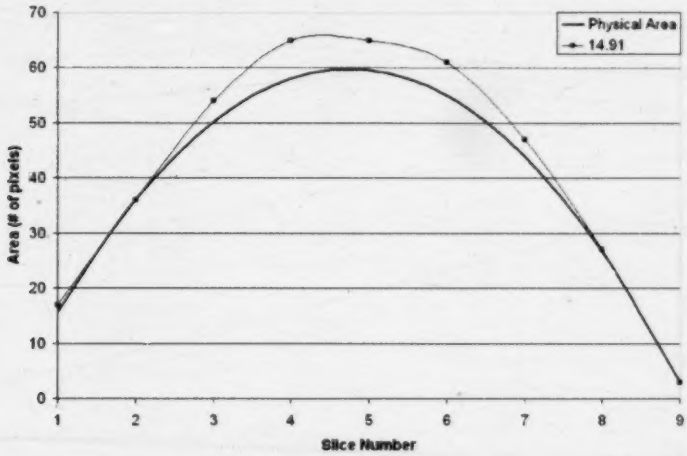

Figure 6.12: Calculated area using the tri-axial iterative thresholding method versus slice number for the medium sphere at a target to background activity concentration ratio of fifteen to one. This data set was not used to generate the fit used in the iterative thresholding.

In both the simple and tri-axial iterative threshold methods described above the images upon which segmentation is to be preformed must be selected by the user. Simply applying either of these iterative threshold algorithms to the entire data set will not result in an accurate determination of the region of interest. Both of these approaches may identify a region of interest on every slice of the image set irrespective of the presence or absence of the target. It may be possible to manually choose slice limits for the analysis which gives good final results, however this method is not automatic and leaves room for user variability. Manual choice of the range of images to be analyzed is subjective and detracts from the ability to provide accurate and reproducible results. This problem may be solved by examining the contrast presented by each image. The contrast at any slice location is the quotient between maximum and mean background pixel intensities. When contrast is plotted as a function of slice location a peak occurs

identifying the target volume. The range of slices to be analyzed is then chosen from both the full width at half and quarter maximum of the contrast versus slice location curve. The axial data set is analyzed over the range of slices which correspond to the full width at quarter maximum while the coronal and sagittal data set are analyzed over those slices contained within the full width at half maximum as this choice of ranges gave the best results. These automated slice limit choices were found to yield correct delineation of the small end regions of the target but unfortunately also resulted in an overestimation of the central regions of the spherical targets.

6.3 Irregular Targets

Figure 6.13: Photograph of the deformed spheroid volume.

Figure 6.14: Photograph of the small bottle used as an irregular shaped target volume.

The axial and tri-axial method threshold of two iterative thresholding techniques were also applied to two irregular target volumes: an irregular spheroid, which was created by deforming a spherical volume in three regions, and a small bottle of variable cross section, see **Figures 6.13** and **6.14**. The physical area per slice of these volumes was determined by CT scanning, the results of which are shown in **Figures 6.15(a-e)** and **6.16(a-e)**. These irregular targets were scanned over a target to background activity concentration range of approximately 15:1 to 2:1. **Figures 6.15 (a-e)** and **6.16 (a-e)** show the results of iterative thresholding for the irregular spheroid target and the small bottle in comparison to their CT derived cross sectional areas for the different target to background activity concentration ratios examined. The results for the irregular spheroid reveal that the tri-axial iterative threshold method with a threshold of two overestimates the size of the target for target to background activity concentration ratios of 5, 10 and 15. For target to background activity concentration ratios of 3.02 and 2.02 cross sectional areas near the center of the volume are more closely identified while near the periphery they are underestimated. In general, the tri-axial method threshold of two yields slightly better target delineation than does the simple axial approach. Results for the small bottle are best for large target to background activity concentration ratios and poorest for small ratios. As with the irregular spheroid, the tri-axial method threshold of two yields slightly better target

delineation than does the simple axial approach. With either technique the addition of a 10 mm margin is prudent in order to ensure that no cross sections are underestimated.

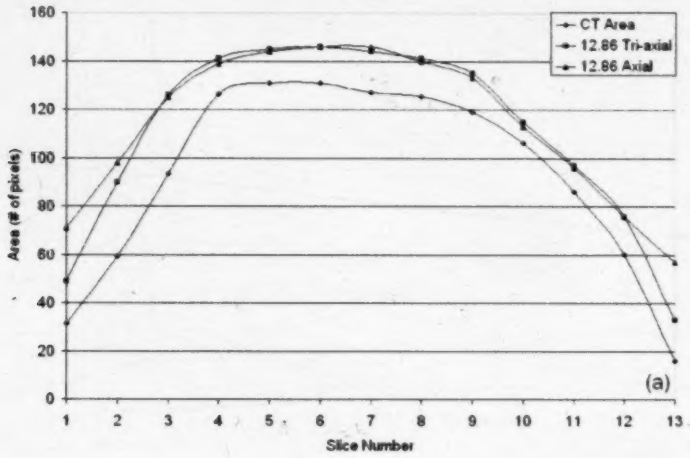

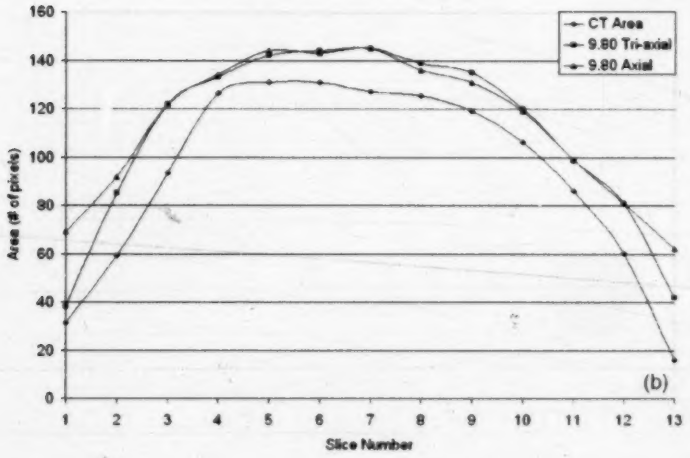

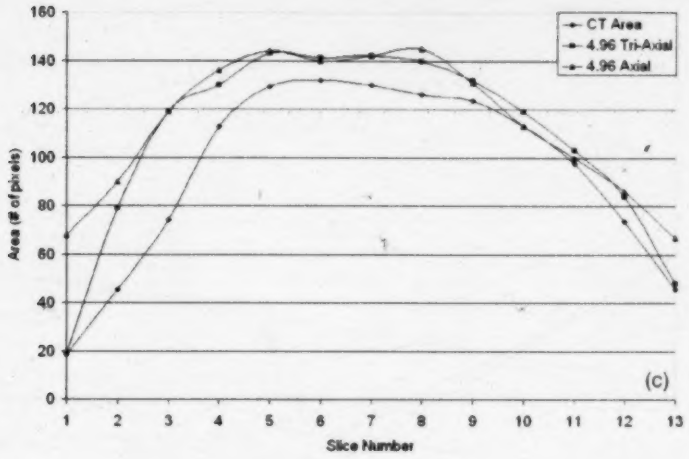
CT Area
4.96 Tri-Axial
4.96 Axial
Area (# of pixels)
Slice Number
(c)

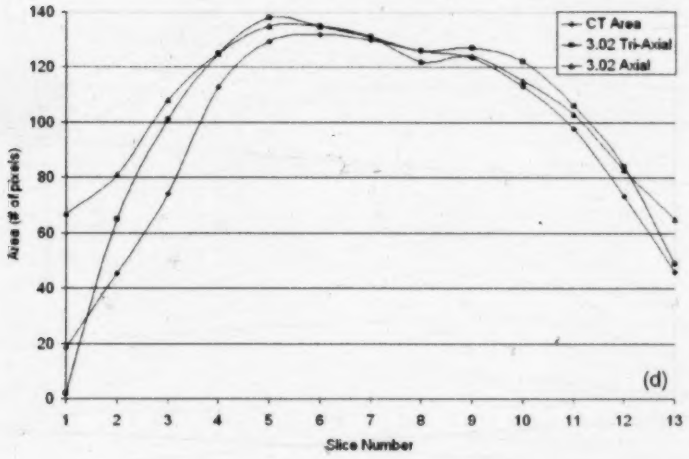
CT Area
3.02 Tri-Axial
3.02 Axial
Area (# of pixels)
Slice Number
(d)

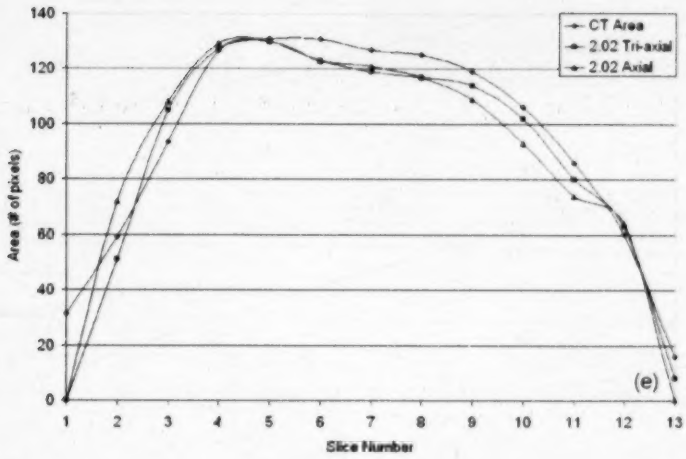

Figure 6.15: Comparison of CT generated, axial and tri-axial iterative threshold areas versus slice number for the deformed spheroid target for target to background activity concentration ratios of approximately (a) 15, (b) 10, (c) 5, (d) 3 and (2) to one.

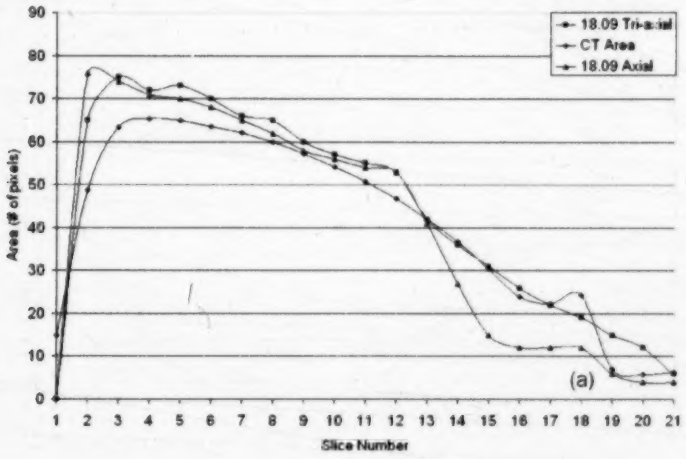

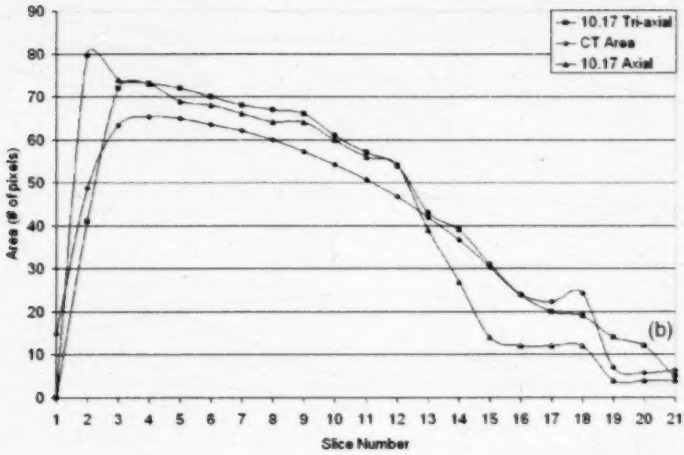
10.17 Tri-axial
CT Area
10.17 Axial
Area (# of pixels)
Slice Number
(b)

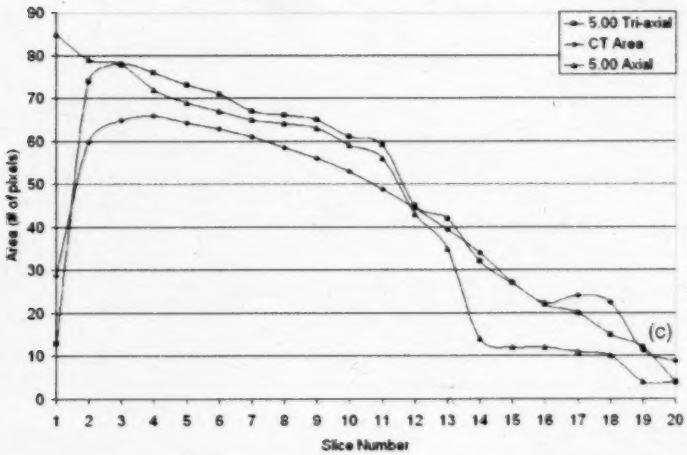
5.00 Tri-axial
CT Area
5.00 Axial
Area (# of pixels)
Slice Number
(c)

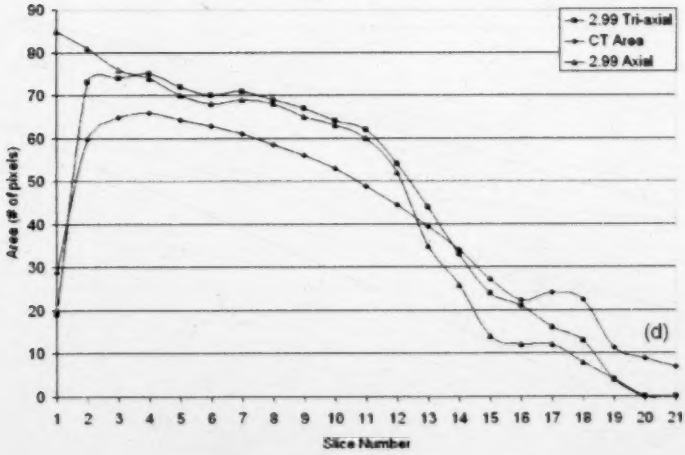
2.99 Tri-axial
CT Area
2.99 Axial
Area (# of pixels)
Slice Number
(d)

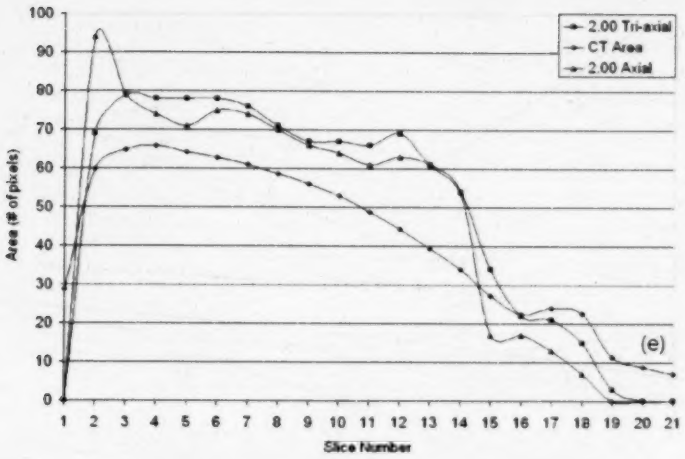

Figure 6.16: Comparison of CT generated, axial and tri-axial iterative threshold areas versus slice number for the small bottle target for target to background activity concentration ratios of approximately (a) 15, (b) 10, (c) 5, (d) 3 and (2) to one.

6.4 Application to Patient Data

To explore the clinical application of the iterative method, data from a patient was analyzed. This particular patient presented with several regions of elevated activity density, one adjacent to the heart near the spinal cord, a second near the midline of the patient in the upper portion of the left lung, and a third volume located near the patient's left shoulder, see **Figure 6.17**. The volumes associated with these regions of elevated activity were found using the tri-axial method threshold of two iterative thresholding technique and compared to those derived from a CT scan. CT based volumes were analyzed by a staff radiologist and described as ellipsoids for which the three principle radii were determined.

Figure 6.17: Patient image, note the dark spots in the patient's left lung. The first spot is near the left shoulder, the second near the midline and the third near the heart of the patient.

The results of this investigation are presented in **Table 6.2**. Here it may be seen that the first PET volume (near the heart) does not agree within experimental error with the CT determined volume. The PET delineation yields a volume nearly three times larger than that determined from CT, and is most likely due to the close proximity of the muscle tissue of the heart which itself also displays elevated levels of activity. In this case the tumor and the heart are in such close proximity that their volumes blur together such that no definitive boundary between the two structures could be identified. A further confounding factor at this site is the movement of the heart. In CT the heart was imaged over a very short time frame which acts to minimize the extent of its motion captured, while the PET scan was acquired over a period of minutes, during which time the heart will have moved. PET results for the lung tumor near the midline of the patient agree within error with the CT defined volume. The final region of interest studied (near left shoulder) produced a PET determined volume of nearly 7000 mm^3, but was not visible in the CT data set due to a large number of streak artifacts.

Location	PET Volume (mm^3)	CT Volume (mm^3)
Near Heart	64768	24097 ± 2191
Left Lung near midline	5248	5426 ± 388
Near Left Shoulder	6976	Not visible

Table 6.2: Summary of clinical volumes determined from both PET and CT patient images.

The limited scope of this assessment of the application of the iterative threshold technique to real patient data limits the veracity of the conclusions which may be drawn from it. Subject to this caveat the following observations may be forwarded. The iterative threshold technique seems to work well for patient data as long as the tumor volume is not in such close proximity to another region of elevated activity so as to obfuscate a distinct boundary between the two. This is readily shown both by the failure of the technique to accurately determine the volume of the tumor that is adjacent to the heart. The agreement seen between PET and CT derived volumes for the tumor located in the left lung near midline is supportive of the clinical utility of the tri-axial iterative threshold technique. In the third case the left shoulder lesion is only visible in the PET scan and as such PET serves as the only useful source of volumetric data concerning this lesion. The results presented in this thesis strongly suggest that the PET volume derived by the tri-axial threshold segmentation technique would, with the judicious addition of a margin, yield a target of sufficient geometric accuracy to allow an effective radiotherapy plan to be crafted.

6.5 Conclusion

The process of iterative thresholding was developed to provide an automated method for the segmentation of PET images. This technique was developed since the Sobel edge detection and the watershed methods proved unable to yield accurate geometric PET image segmentation and the use of simple thresholding is problematic.

The first step in developing the iterative thresholding technique was to fit the ideal threshold versus physical area for the spherical targets. The fit equations describe an exponential drop followed by a slowly increasing linear tail, shown in **Equations 6.10** and **6.11**. Two fits to the data were necessary; the first for small targets, those with a diameter of less than 24 mm and the second for large targets.

Next the iterative thresholding technique was tested on the axial data sets of the spherical targets. The iterative thresholding method was effective at segmenting large and medium sized spherical targets at large target to background activity concentration ratios. However this method did not provide useful results for the small spherical targets. In this case the results were similar to those produced by the Sobel and watershed techniques.

To improve segmentation results the iterative thresholding technique was applied to the axial, coronal and sagittal data sets for each target. The final data set constructed by applying the iterative thresholding to the three data sets consisted of four distinct pixel values, from zero to three. To accurately segment the target volume it was necessary to apply a final threshold value. Initially the final threshold value was set to one, which resulted in an overestimation of the target volume. Therefore, a final threshold value of two was used. A comparison of the results of the single threshold method, from **Chapter 5**, the axial and tri-axial iterative thresholding methods are shown in **Table 6.1**. From these results it can be seen that the iterative thresholding technique, both axial and tri-axial, can more accurately segment images of spherical target volumes. However the tri-axial iterative thresholding is more accurate than the axial iterative thresholding for the small spherical target.

To further test the axial and tri-axial iterative thresholding methods two irregularly shaped target volumes were CT and PET scanned. The axial and tri-axial iterative thresholding areas were compared to the CT areas at each slice location and are shown in **Figures 6.15** and **6.16**. From these figures it can be seen that the agreement between the iterative thresholding techniques and the CT areas is not high. The difference in areas is due to one of the assumptions made in the generation of the fit of ideal threshold versus area data. The physical area was calculated analytically in terms of squared millimeters then converted into the

number of pixels. However this conversion will overestimate the number of whole pixels that can fit within a circular region. Therefore, when the iterative thresholding areas are compared to the CT areas the iterative thresholding areas are too large. This difference is slight, on the order of ten percent and is a result of the model.

Finally the tri-axial iterative thresholding technique was applied to patient data. The iterative thresholding method accurately segmented a lesion in the lung near the midline of the patient; it also found a region of higher uptake near the patient's left shoulder that was not visible in the CT data set. The lesion near the heart was not accurately delineated. This failure is likely due to the proximity of the heart with its high uptake of FDG in combination with the greater degree of cardiac function captured in PET as compared to CT.

The ability to accurately segment PET images is necessary if the metabolic information contained in PET images is to be used in radiation therapy treatment planning. Three known methods of image segmentation: simple thresholding, Sobel edge detection and the watershed method were tested, and none were able to accurately segment PET images. Therefore the axial and tri-axial iterative thresholding techniques were developed. As the axial and tri-axial iterative thresholding method can accurately segment PET images, both phantom and patient, it may be possible to use PET images in the definition of the target volume for radiation therapy.

7. Conclusion and Future Directions

If positron emission tomography is to fill a quantitative role in the planning and assessment of radiation therapy treatments of cancer an accurate and automated method of image segmentation needs to be developed. In this work three segmentation methods were examined: thresholding, Sobel edge detection and the watershed technique, of which only the thresholding method proved able to accurately delineate regions of interest. Failure of the Sobel and watershed methods to accurately delineate volumes is due to assumptions inherent to those segmentation schemes. The Sobel method, for example, assumes that the boundary between a target and the surrounding background can be found by a maximum gradient in the image intensity. Inherent to this line of reasoning is the existence of a sharp physical discontinuity between the object and the background, which was indeed achieved with the experimental setup used. Partial volume effects in the image, however, serve to blur even the sharpest physical discontinuities, which, in turn, limit the use of the Sobel and other similar edge detection methods for the quantitative analysis of PET images. The watershed method is potentially more mathematically robust than the Sobel edge detection scheme as it employs concepts derived from mathematical morphology. Nevertheless the watershed approach ultimately attempts to identify edges within an image and hence is hampered by the same partial volume effects which thwart the Sobel approach. Since the Sobel and watershed methods failed on simple geometrical targets, such as cylinders and spheres, it is unlikely that either method would prove useful in the analysis of patient images.

While the threshold method can accurately segment a PET image, it can not be used in a straight forward manner as the choice of the threshold level which yields accurate target delineation depends strongly on the size of the target, and to a lesser extent on the target to background activity concentration ratio and weakly upon the radial offset of the target from the centre of the phantom. As it has been shown, it is possible to choose a single threshold level to apply to all images irrespective of size, activity concentration level and position. Doing so, however, requires the judicious choice of a threshold value which will ensure that no single cross section is underestimated. This is essential if one is to avoid the exclusion of diseased tissue from the delineated region. Proceeding in this manner will always result in the inclusion of uninvolved

surrounding normal tissue within the volume which will be incorrectly identified as tumor. The degree of geometric conformity between measured and true physical cross sectional areas achieved with this single threshold approach is greatest for large volumes and least for small volumes. For each particular volume the largest cross sections are the most accurately reproduced while the smallest exhibit the greatest deviation from their true size.

In an attempt to avoid the pitfalls associated with the use of a single universal threshold level, a fully automatic method of PET image threshold segmentation was developed. In this approach the ideal threshold is found iteratively on a slice by slice basis through the use of an empirical fit based upon the many ideal threshold data points derived experimentally from the spherical volumes examined in this work. With this method it is possible to outline both regular and irregular geometric shapes with reasonable accuracy. As with all threshold schemes the accuracy of this approach is best for large volumes and least for small volumes. Unfortunately the automated iterative method proves less than perfect as it leaves some cross sections underrepresented thus necessitating the addition of a margin, on the order of 1 cm, in order to ensure that the full extent of the target volume is completely contained within the delineated region. While the universal addition of a uniform margin will ensure that no cross sections are under represented it will inevitably result in the unavoidable inclusion of surrounding uninvolved tissue within the delineated volume which serves to define the geometric extent of the tumor. Ultimately, the practical utility of using either the single threshold approach or the automated iterative technique is a matter for clinical judgment.

As a final endpoint the automated iterative threshold technique developed in this thesis was applied to the PET tumor volumes of a real clinical patient. The targets delineated for this patient were compared to their corresponding CT derived volumes. In one case the PET derived volume greatly exceeded its CT defined counterpart due in large part to the presence of an adjacent hot organ (the heart) which was close enough to the tumor volume such that partial voluming effectively obfuscated the boundary between these two objects. Clearly there remains the need for the application of clinical judgment even with the use of a "fully automated" segmentation technique such as the one applied here when finalizing geometric extent of PET defined tumor volumes. The second PET defined tumor volume delineated in this manner agreed

quite well with its extent as indicated by CT. The third of these tumors was clearly visible in PET while CT was unable to demonstrate its presence. While exceedingly limited in its scope, this simple application succinctly demonstrates both the potential and the limitations of the clinical application techniques developed in this thesis.

Future directions indicated by this work include an investigation into the effects of filtering, deconvolution and smoothing of PET images prior to the application of the segmentation techniques discussed in this thesis. Further work might also focus on accounting for the presence of motion such as would occur for structures affected by respiration and cardiac function. An investigation into the use of alternate reconstruction algorithms is also warranted. As FDG uptake in a malignancy decreases rapidly with the application of an effective treatment[3], the results of this work could also be used to evaluate the response of a malignancy to treatment. A decrease in FDG uptake has been found to occur prior to a detectable decrease in the physical size of the mass as seen in conventional CT images, therefore the efficacy of a treatment might be assessed very soon after the commencement of treatment. A possible course of application would see the tumor initially delineated from a PET scan prior to treatment using the technique developed here. PET scans carried out during the course of treatment would aid the clinician in monitoring progress and determining therapeutic efficacy. Tumor delineation could potentially provide a quantitative measure of tumor response. Information concerning the evolution of the tumor during this time might then be used to further modify the course of treatment. Post treatment PET scans might provide valuable information with regard to the long term effectiveness of treatment and provide an early warning of the need for subsequent intervention.

Positron emission tomography images have been used for some time in the diagnosis of malignancy; however the full extent of the information provided by this powerful imaging modality has not been realized. FDG PET images provide unique information about the true extent of the disease as this modality measures the metabolic activity of tissues. Higher metabolic activity is an indicator of a cancerous growth. A method of quantifying the size of the region of higher activity density is needed if PET images are to be used in the planning of radiation therapy. The study of thresholding, Sobel edge detection and the

watershed method of image segmentation have been studied, and, of these three, only thresholding shows promise in the quantification of PET images. However the direct application of a threshold to a PET image is problematic due to the dependence of the ideal threshold on the size of the object contemplated. To overcome this difficulty an iterative threshold technique was developed which is both automatic and reasonably accurate. The iterative thresholding segmentation method was applied to both regularly and irregularly shaped phantom target volumes as well as patient data. Iterative thresholding shows promise in the future as a method for both aiding the quantitative identification of cancerous volumes for radiotherapy treatments and the subsequent monitoring of the effectiveness of treatment on cancer patients.

References

[1] J.D. Bradley et al., "Implementing Biologic Target Volumes in Radiation Treatment Planning for Non-Small Cell Lung Cancer," J Nucl Med. **45**, 96S-101S (2004).

[2] S.R. Cherry, J.A. Sorenson and M.E. Phelps, *Physics in Nuclear Medicine*, 3rd Edition. (Saunders, USA, 2003).

[3] P. Rigo et al., "Oncological applications of positron emission tomography with fluorine-18 fluorodeoxyglucose," Eur J Nucl Med. **23**, 1641-1674 (1996).

[4] A. Dimitrakopoulou-Strauss et al., "The role of quantitative (18)F-FDG PET studies for the differentiation of malignant and benign bone lesions," J Nucl Med. **43**, 510-518 (2002).

[5] M. Sasaki et al., "Comparison of MET-PET and FDG-PET for differentiation between benign lesions and malignant tumors of the lung," Ann Nucl Med. **15**, 425-431 (2001).

[6] A. Gutzeit et al., "Unknown Primary Tumors: Detection with Dual-Modality PET/CT-Initial Experience," Radiology **234**, 227-234 (2005).

[7] S. Apisarnthanarax, K.S.C. Chao, "Current Imaging Paradigms in Radiation Oncology," Radiation Research **163**, 1-25 (2005).

[8] M.N. Maisey, "Overview of clinical PET," The British Journal of Radiology **75**, S1-S5 (2002).

[9] J. Czernin, H. Schelbert, "PET/CT Imaging: Facts, Opinions, Hopes, and Questions," J Nucl Med. **45**, 1S-3S (2004).

[10] J. Skalski, R.L. Wahl and C.R. Meyer, "Comparison of Mutual Information-Based Warping Accuracy for Fusing Body CT and PET by 2 Methods: CT Mapped onto PET Emission Scan Versus CT Mapped onto PET Transmission Scan," J Nucl Med. **43**, 1184-1187 (2002).

[11] P.J. Slomka et al., "Automated 3-Dimensional Registration of Stand-Alone ^{18}F-FDG Whole-Body PET with CT," J Nucl Med. **44**, 1156-1167 (2003).

[12] W.C. Lavely et al., "Phantom validation of coregistration of PET and CT for image-guided radiotherapy," Med. Phys. **31**, 1083-1092 (2004).

[13] B.M. Klabbers et al., "Matching PET and CT scans of the head and neck area: Development of method and validation," Med Phys. **29**, 2230-2238 (2002).

[14] K. Mah et al., "The impact of 18FDG-PET on target and critical organs in CT-based treatment planning of patients with poorly defined non-small-cell lung carcinoma: a prospective study," Int. J. Radiation. Oncology Biol. Phys. **52**, 339-350 (2002).

[15] Levin CS and Hoffman EJ, "Calculation of positron range and its effect on the fundamental limit of positron emission tomography system spatial resolution," Phys. Med. Biol. **44**, 781-799 (1999).

[16] P. Hautojārvi, *Positrons in Solids*, (Springer-Verlag, New York, 1979)

[17] J.W.M. DuMond, D.A. Lind, and B.B. Watson, "Precision Measurement of the Wave-Length and Spectral Profile of the Annihilation Radiation from Cu64 with the Two-Meter Focusing Curved Crystal Spectrometer," Physical Review **75,** 1226-1239 (1949).

[18] K.L. Rose and S. DeBenedetti, "Positron Annihilation in Solid Argon," Phys. Rev. **138**, 927-933 (1965).

[19] S. Cova and L. Zappa, "Effective number of annihilation electrons per atom for free positrons in condensed matter," J. Phys. B. **1**, 795-801 (1968).

[20] A. Sánchez-Crespo, P. Andreo, and S.A. Larsson, "Positron flight in human tissues and its influence on PET image spatial resolution," E. J. Nuc. Med. Mol. Img. **31**, 44-51 (2003).

[21] O.E. Mogensen and F.M. Jacobsen, "Positronium yields in liquids determined by lifetime and angular correlation measurements," Chemical Physics **73**, 223-234 (1982).

[22] ICRU, *Tissue Substitutes in Radiation Dosimetry and Measurement,* Report 44 of the International Commission on Radiation Units and Measurements (Bethesda, MD, 1989).

[23] C.L. Melcher, "Scintillation Crystals for PET," J Nucl Med. **41**, 1051-1055 (2000).

[24] K.S. Krane, *Introductory Nuclear Physics*, 3rd Edition (John Wiley & Sons, New York, 1988).

[25] J.S. Lim, *Two Dimensional Signal and Image Processing*, (Prentice Hall, Englewood Cliffs, N.J., 1990).

[26] R.C. Gonzalez and R.E. Woods, *Digital Image Processing*, 2nd Edition, (Prentice Hall, Upper Saddle River, N.J., 2002).

[27] M. Mancas and B. Gosselin, "Towards an automatic tumor segmentation using iterative watersheds," Proc. SPIE Medical Imaging 2004: Image Processing, 1598-1608 (2004).

[28] C. Xu and J.L. Prince, "Snakes, Shapes, and Gradient Vector Flow," IEEE Transactions on Image Processing, 359-369 (1998).

[29] S. Beucher and F. Meyer, "The Morphological Approach to Segmentation: The Watershed Transformation" in *Mathematical Morphology in Image Processing*, E. Dougherty (ed.), (Marcel Dekker, New York, 1993).

[30] R. Boellard et al., "Effects of Noise, Image Resolution, and ROI Definition on the Accuracy of Standard Uptake Values: a Simulation Study," J. Nucl. Med. **45**, 1519-1527 (2004).

[31] Y.E. Erdi et al., "Segmentation of Lung Lesion Volume by Adaptive Positron Emission Tomography Image Thresholding," Cancer **80**, 2505-2509 (1997).

[32] L. Adam et al., "Performance of a Whole-Body PET Scanner Using Curve-Plate NaI(Tl) Detectors," J. Nucl. Med. **42**, 1821-1830 (2001)

[33] J.W. Keyes, "SUV: standard uptake value or silly useless value?" J. Nucl. Med. **36**, 1836-1839 (1995)

[34] M.M. Graham, L.M. Peterson and R.M. Hayward, "Comparison of simplified quantitative analyses of FDG uptake," Nucl. Med. Biol. **27**, 647-655 (2000).

[35] U. Nestle et al., "Comparison of Different Methods for Delineation of ^{18}F-FDG PET-Positive Tissue for Target Volume Definition in Radiotherapy of Patients with Non-Small Cell Lung Cancer," J. Nucl. Med. **46**, 1342-1348 (2005).

[36] C.B. Caldwell et al., "Observer variation in contouring gross tumor volume in patients with poorly defined non-small-cell lung tumors on CT: the impact of ^{18}FDG-hybrid PET fusion," Int. J. Radiation Oncology Biol. Phys. **51**, 923-931 (2001).

[37] B. Yaremko et al., "Threshold modification for tumor imaging in non-small-cell lung cancer using positron emission tomography," Nuclear Medicine Communications **26,** 433-440 (2005).

[38] http://iacl.ece.jhu.edu/projects/gvf/